GRATING-BASED BEAM SHAPING AND INELASTIC INTERFEROMETRY WITH FREE ELECTRONS

by

CAMERON WARREN JOHNSON

A DISSERTATION

Presented to the Department of Physics
and the Division of Graduate Studies of the University of Oregon
in partial fulfillment of the requirements
for the degree of
Doctor of Philosophy

June 2021

DISSERTATION APPROVAL PAGE

Student: Cameron Warren Johnson

Title: Grating-Based Beam Shaping and Inelastic Interferometry with Free Electrons

This dissertation has been accepted and approved in partial fulfillment of the requirements for the Doctor of Philosophy degree in the Department of Physics by:

Brian J. Smith	Chairperson
Benjamin J. McMorran	Advisor
Benjamín J. Alemán	Core Member
David C. Johnson	Institutional Representative

and

Andy Karduna	Interim Vice Provost for Graduate Studies

Original approval signatures are on file with the University of Oregon Division of Graduate Studies.

Degree awarded June 2021

DISSERTATION ABSTRACT

Cameron Warren Johnson

Doctor of Philosophy

Department of Physics

June 2021

Title: Grating-Based Beam Shaping and Inelastic Interferometry with Free Electrons

Here I present studies for the manipulation of free electrons using material holograms and the application of holographically structured electrons in interferometry. The research in this dissertation can be divided into two main sections. First, is the design and nanofabrication of off-axis material holograms for free electrons that can be used to arbitrarily shape the amplitude and phase of the electron wavefront. Focused ion beam gas-assisted etching is presented as a method to reliably achieve the fabrication resolution required to produce the intended grating groove profiles to optimize diffraction efficiency and meet the precise hologram depth profiles required to impart a desired structured wavefront. An analytical method for finding hologram groove profiles is also outlined and experimental tests are performed to verify its accuracy. In the second portion, binary straight diffraction gratings are placed in a transmission electron microscope to create a scanning two-grating Mach-Zehnder interferometer. The

sensitivity of the relative phases in the interferometer output are shown through the relative alignment of the gratings, as well as by introducing external phase shifts from static potentials to the path separated probes. The interferometer's capability to achieve phase sensitive nanoscale imaging is also demonstrated. Finally, the interferometer is used to measure interference between a coherent superposition of electrons inelastically scattered from the dipole plasmon of a gold nanoparticle.

This dissertation contains previously published and unpublished material.

CURRICULUM VITAE

NAME OF AUTHOR: Cameron Warren Johnson

GRADUATE AND UNDERGRADUATE SCHOOLS ATTENDED:

University of Oregon, Eugene, Oregon
University of Washington, Seattle, Washington
South Seattle College, Seattle, Washington

DEGREES AWARDED:

Doctor of Physics, 2021, University of Oregon
Bachelor of Physics, 2016, University of Washington
Associate of Science, 2014, South Seattle College

AREAS OF SPECIAL INTEREST:

Electron Optics, Diffraction Physics, Interferometry

PROFESSIONAL EXPERIENCE:

Graduate Research Assistant, University of Oregon, 2016-2021

Northstar Program Lab Instructor, University of Oregon, 2016-2018

Graduate Employee Teaching Assistant, University of Oregon, 2016-2017

Undergraduate Research Assistant, University of Washington, 2014-2016

CH-53E Helicopter Mechanic/Sergeant, USMC, 2006-2012

GRANTS, AWARDS AND HONORS:

Graduate School Dissertation Fellowship, University of Oregon, 2020

1st Place Poster Award, Microscopy and Microanalysis, Portland Oregon, 2018

1st Place Poster Award, Graduate Research Forum, University of Oregon, 2018

National Science Foundation Graduate Research Fellowship, University of Oregon, 2017

PUBLICATIONS:

C. W. Johnson, A. E. Turner, F. J. García de Abajo, B. J. McMorran. Grating-Based Inelastic Mach-Zehnder Interferometry with Free Electrons. {*Manuscript in Prepraration*}, 2021.

C. W. Johnson*, A. E. Turner*, and B. J. McMorran. A Scanning 2-Grating Free Electron Mach-Zehnder Interferometer. {*Submitted*}, arXiv:2104.09992 [physics.ins-det], April 2021.

A. E. Turner, **C. W. Johnson**, P. Kruit, B. J. McMorran. Interaction-Free Measurement with Electrons. {*Submitted*}, 2021.

T. Řiháček, M. Horák, T. Schachinger, F. Mika, M. Matějka, S. Krátký, T. Fořt, T. Radlička, L. Novák, B. Sed'a, B. J. McMorran, **C. W. Johnson**, I. Müllerová. Beam shaping and probe characterization in the scanning electron microscope. *Ultramicroscopy*, 225:113268, 2021.

V. Brogden, **C. W. Johnson**, C. Rue, J. Graham, K. Langworthy, S. Golledge, and B. J. McMorran. Material Sputtering with a Multi-Species Plasma Focused Ion Beam. *Advances in Materials Science and Engineering*, 2021:8842777, 2021.

C. W. Johnson*, J. S. Pierce*, R. C. Moraski, A. E. Turner, A. T. Greenberg, W. S. Parker, and B. J. McMorran. Exact Design of Complex Amplitude Holograms for Producing Arbitrary Scalar Fields. *Optics Express*, 28(12):17334-17346, 2020.

C. W. Johnson, D. H. Bauer, and B. J. McMorran. Improved Control of Electron Computer-Generated Holographic Grating Groove Profiles Using Ion Beam Gas-Assisted Etching. *Applied Optics*, 59(6):1594-1601, 2020.

X. Linpeng, M. Viitaniemi, A. Vishnuradhan, Y. Kozuka, **C. W. Johnson**, M. Kawasaki, and K. Fu. Coherence properties of shallow donor qubits in ZnO. *Phys. Rev. Applied*, 10(6):064061, 2018.

* Co-first authors with equal contributions.

ACKNOWLEDGEMENTS

I would like to thank my research advisor Benjamin McMorran whose advice and constant encouraging support has not only helped my professional development as a scientist, but also continually inspires me to have a more optimistic worldview. Everyone in the McMorran lab who have all had a heavy hand in the development and execution of this research, especially Jordan Pierce and Amy Turner who have both been co-authors with equal contributions on much of this work. All the educators and mentors who have played a role in guiding me towards and through academia, a few standouts among many are Elizabeth Schoene, Jacob Ashcraft, and Kai-Mei Fu. Thanks to my family: siblings, parents, and particularly my partner Jess, who has kept me emotionally grounded throughout gradschool. Miscellaneous thank yous to: Bit, Cheech, troll beers, and hobbies. Finally, thanks to all the sources of funding and financial support for this research: University of Oregon Graduate School, the National Science Foundation (Grant No: 1309047 & 1607733), as well as the Department of Energy (Grant No: DE-SC0010466).

TABLE OF CONTENTS

LIST OF FIGURES

LIST OF TABLES

Table Page

CHAPTER I

INTRODUCTION

1.1. History and Motivation

Although atomic theories of nature and macroscopic electrical phenomena were known to the ancient Greeks, the discrete aspect of electrons and the constant of charge they carry were not veritably discovered until the turn of the 20^{th} century with J. J. Thomson's 1897 cathode ray tube and Robert Millikan's 1909 oil drop experiments, respectively [1, 2]. In the following decades, the physical laws governing the behavior of bound electrons was the subject of intense scrutiny and was instrumental in the development of quantum mechanics and modern atomic theory [3]. Concurrently, Louis de Broglie proposed a hypothesis on the quantum mechanical wave nature of free electrons (and all massive quantum particles) assigning a wavelength that is inversely proportional to its momentum, $\lambda \propto p^{-1}$ [4]. While this property seems to contradict the previously measured point-like particle nature of electrons, it is technically complimentary and was independently verified a few years later by George Paget Thomson (son of J. J. Thomson), as well as Clinton Davisson and Lester Germer by showing that electrons could diffract from both amorphous and crystalline materials [5, 6]. Soon after in 1933, Ernst Ruska constructed the first electron microscope opening a crucial window into the sub-micron world with electron microscopy [7]. Dismayed by the resolution of these early microscopes, Dennis Gabor developed his holographic principle that exploited electron interference to surpass technological resolution limits [8]. In 1952, Haine and Mulvey provided an experimental verification of the holographic principle with

electrons [9], subsequently Gabor's holographic principle has become a versatile tool in the physics of image formation for all wave mediums. So far, electron microscopy, along with its various spectroscopic capabilities, has achieved the highest imaging resolution of all microscopic techniques [10], providing an immeasurable insight into atomic-scale structure and energetic information of materials, leading to innumerable advances in materials science and nanoscale physics [11]. While bound electrons play a central role in the properties of materials, here we describe studies of free electrons in vacuum, and unless state otherwise any mention of an electron can be assumed to be a free electron.

We can describe the state of individual electrons in an electron microscope with a beam-like geometry where the expectation value of momentum is in the longitudinal direction with only a small distribution in the transverse plane. The degree to which an electron will exhibit wavelike behavior is determined by the purity of its quantum state. A pure electron quantum state is spatially and temporally coherent, that is, different parts of the transverse/longitudinal wavefront can perfectly self-interfere if they were displaced in space/time to overlap. In practice, most electron states are partially coherent having a finite coherence lengths/times. The coherence length is largely associated with the spatial extent of the emission source and is constant with angular spread, scaling with beam diameter, where as the coherence time is associated with the energy distribution of the electron. However, modern field emission electron sources have an energy spread to peak energy ratio that is comparable to a HeNe laser, and the spatial coherence of the beam can be improved by selecting a smaller solid angle of wavefront. Under these conditions, it is valid to approximate the propagation of an electron as a pure quantum state, but if necessary

the partial coherence can be incorporated to the pure state solution perturbatively [12].

Many traditional electron microscopy techniques rely on diffraction and interference of coherent electrons after interactions with condensed matter systems to determine the structure and composition of matter. However, using electrons to probe quantum coherent interactions is a relatively new concept that is being explored in the emerging field of quantum electron optics [13, 14]. Some specific topics in this developing field include: interaction free measurements [15], coherent optical control [16], quantum state tomography [17], transfer of orbital angular momentum [18], the Aharonov-Bohm effect [19], and electron decoherence and entanglement [20, 21]. Research of these topics has been enabled by structuring the longitudinal [22] and transverse [23] electron wavefunction and interferometry [24], but being an emerging field, there is much room for new and improved methods and experiments [25].

In this dissertation, I explore methods that improve shaping the electron transverse momentum distribution and wavefront with off-axis material holograms, use diffraction gratings to construct a novel, highly functional, scanning grating-based interferometer in a transmission electron microscope (TEM), and finally demonstrate inelastic interferometry with coherent superpositions of plasmon scattered electrons.

1.2. Background Information

Before diving into the main body of research presented in this dissertation, we cover some background concepts that are instrumental for the heuristic understanding of the main chapter contents.

1.2.1. Free Electron Solutions to Schrödinger Equation

The fully relativistic, quantum mechanical dynamics of free electrons can be determined with the Dirac equation [26]. Although electrons in a TEM are inherently relativistic with velocities that are a considerable fraction of the speed of light, the benefits of explicit inclusion of spin and Lorentz invariance afforded by the Dirac equation are not outweighed by its complexity [12]. Instead, we can apply a relativistic correction to the Schrödinger equation that provides a description of the electron wavefunction that is sufficiently accurate for most experiments in the TEM [27].

In a conventional TEM there is a continuous emission source and besides the magnetic lenses that are used to focus the electron beam, we consider electrons that only interact with electrostatic potentials such that we can consider the vector potential $\mathbf{A} = 0$. Consequently, the time-independent Schrödinger equation determining the steady-state electron wavefunction can be written as

$$\left(-\frac{\hbar^2}{2m_e}\boldsymbol{\nabla}^2 + V(\mathbf{r})\right)\psi(\mathbf{r}) = E\psi(\mathbf{r}), \tag{1.1}$$

where E is the total energy of the electron, $V(\mathbf{r})$ is the electron's potential energy, and the probability of finding the electron in a volume V is giving by the Born rule $P_{\mathrm{V}} = \int_{\mathrm{V}} d^3\mathbf{r}|\psi(\mathbf{r})|^2$. The electrons are accelerated from the source by an electrostatic potential $V = -eU_{\mathrm{acc}}$, giving a kinetic energy in the column $E_{KE} = E + eU_{\mathrm{acc}}$ and allowing us to write the time independent Schrödinger equation in a form that is identical to the Helmholtz equation

$$\left(\boldsymbol{\nabla}^2 + k^2\right)\psi(\mathbf{r}) = 0, \tag{1.2}$$

where $k = \frac{\sqrt{2m_e E_{KE}}}{\hbar} = \frac{2\pi}{\lambda}$. The relativistic effects in a TEM can be accounted for by replacing the de Broglie wavelength with its relativistic form $\lambda \to \lambda_{rel}$ giving

$$k_{rel} = \frac{2\pi}{\lambda_{rel}} = \frac{1}{\hbar c}\sqrt{E_{KE}^2 + 2E_{KE}m_e c^2}. \tag{1.3}$$

The electrons propagating down the TEM column are traveling, on average, in a single direction with a small beam divergence, see Figure 1.1, allowing the electron

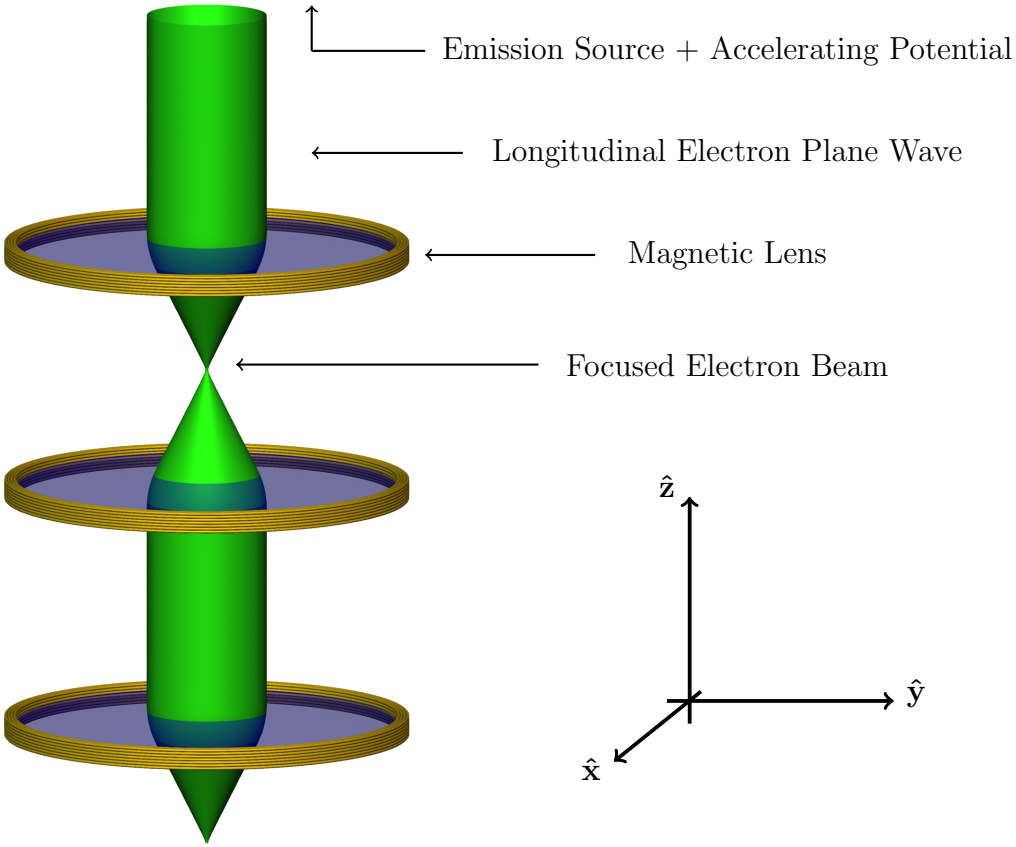

FIGURE 1.1. Cartoon diagram of a paraxial beam of electrons accelerated from a point-like emission source in a TEM column with magnetic lenses to focus the beam. The general coordinate conventions used in this dissertation, z is up and $\mathbf{R} = (x, y)$ is the transverse plane.

wavefunction to be written in the form $\psi(\mathbf{r}) = \phi(\mathbf{r})e^{ik_z z}$ with $k_z \lesssim k_{rel}$ and the mode function $\phi(\mathbf{r})$ governed by the the time-independent paraxial wave equation

$$\left(\boldsymbol{\nabla}_\perp^2 + 2ik_z\frac{\partial}{\partial z}\right)\phi(\mathbf{r}) = 0, \tag{1.4}$$

where $\boldsymbol{\nabla}_\perp^2 = \frac{\partial^2}{\partial x^2} + \frac{\partial^2}{\partial y^2}$ is the transverse Laplacian. This mode function has an exact solution known as the Fresnel diffraction integral

$$\phi(\mathbf{r}) = \frac{k_z}{2\pi i z}\int d^2\mathbf{R}'\,\phi(\mathbf{R}',0)\exp\left(\frac{ik_z}{2z}(\mathbf{R}-\mathbf{R}')^2\right), \tag{1.5}$$

where $\mathbf{r} = (\mathbf{R}, z)$ and $\mathbf{R} = (x, y)$. Conveniently, when z is much larger than the radial extent of $\phi(\mathbf{R}', 0)$, the $k_z\mathbf{R}'^2/z$ term in the argument of the exponent becomes small enough to be neglected making the Fresnel diffraction integral mathematically equivalent to the Fourier transform of $\phi(\mathbf{R}', 0)$. This result is general to the paraxially approximated Helmholtz equation that is widely known in linear Fourier optical theory for scalar waves [28].

1.2.2. Scalar Wave Optics and Coordinate Conventions

All paraxial scalar waves that follow Fourier optical theory can be decomposed into a superposition of plane waves $e^{i\mathbf{k}\cdot\mathbf{r}}$ with a continuous or discrete spectrum of momenta $\hbar\mathbf{k} = (\hbar k_x, \hbar k_y, \hbar k_z)$. We can consider an ideal converging lens with the defining property that it will focus a plane wave incident on the lens to a single location in the transverse plane located a distance f past the lens, called the back focal plane or far field. There is a 1-to-1 relationship between a plane wave's transverse momentum $\hbar\mathbf{K} = (\hbar k_x, \hbar k_y)$ and its focused position in the back focal plane of the lens. For an arbitrary transverse scalar wave incident on the lens

$\psi(\mathbf{R})$ this 1-to-1 mapping to the back focal plane is the Fourier transform and is proportional to the transverse momentum distribution of the incident scalar wave $\widetilde{\psi}(\mathbf{K}) \propto \int d^2\mathbf{R}\, \psi(\mathbf{R}) e^{i\mathbf{K}\cdot\mathbf{R}} \equiv \mathcal{F}\{\psi(\mathbf{R})\}$, Figure 1.2.

When working in holography, we use the coordinate convention that $\mathbf{R} = (x, y)$ is the position coordinate at the hologram or diffraction grating with incident plane waves, and $\mathbf{K} = (k_x, k_y)$ is considered the transverse momentum coordinate in the back focal plane where discrete focused diffraction orders are spatially separated, Figure 1.2(a). Alternatively, when dealing with focused waves scattering from an object it is convenient and physically valid to flip this convention and consider the focused wave incident on the object in the front focal plane of the lens as the position coordinate $\mathbf{R} = (x, y)$, then the back focal plane of the lens is still the momentum coordinate $\mathbf{K} = (k_x, k_y)$, but now is the maximally defocused transverse wavefront. This convention is used so that when we consider an energy loss spectrum, Γ, for the scattering process we can intuitively describe the transverse momentum resolved loss spectrum, $d\Gamma/d\mathbf{K}$, in the far field of the interaction, Figure 1.2(b).

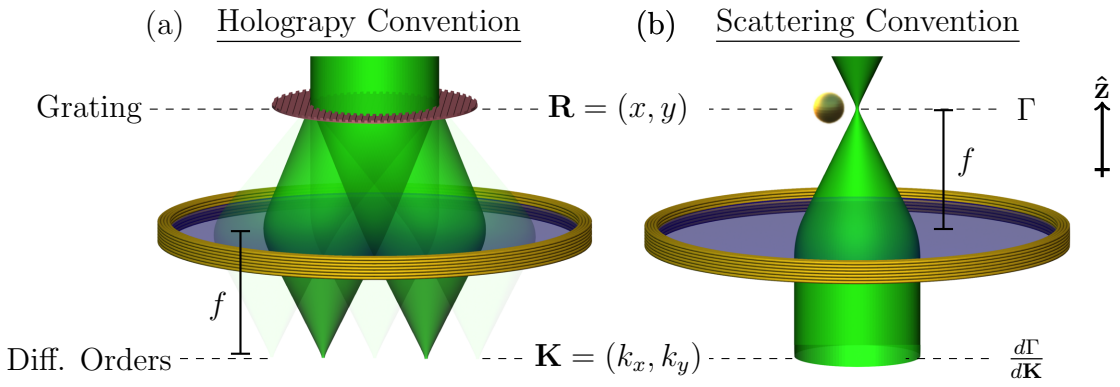

FIGURE 1.2. (a) Transverse plane coordinate convention for holography/diffraction grating experiments; a grating in front of a magnetic lens and the far field diffraction orders spatially separated in the back focal plane. (b) Transverse plane coordinate convention for scattering experiments; a focused electron beam interacting with a sample with interaction probability Γ and the transverse momentum resolved probability $d\Gamma/d\mathbf{K}$ in the back focal plane of a magnetic lens.

1.2.3. A TEM as an Electron Optics Workbench

In general TEMs have current carrying wire coils acting as magnetic lenses and apertures at fixed distances in a vertical column that forms a sequential optical system for the freely propagating electrons. The focal length of each lens can be controlled with independently by increasing or decreasing coil currents and the apertures can be easily be swapped for flat electron optical elements. In the body of this work we use an FEI Titan image-aberration-corrected 60-300 keV scanning transmission electron microscope (STEM/TEM) that has 11 magnetic lenses and 4 aperture holders (Fig. 1.3). Figure 1.3(b,c) show what physical

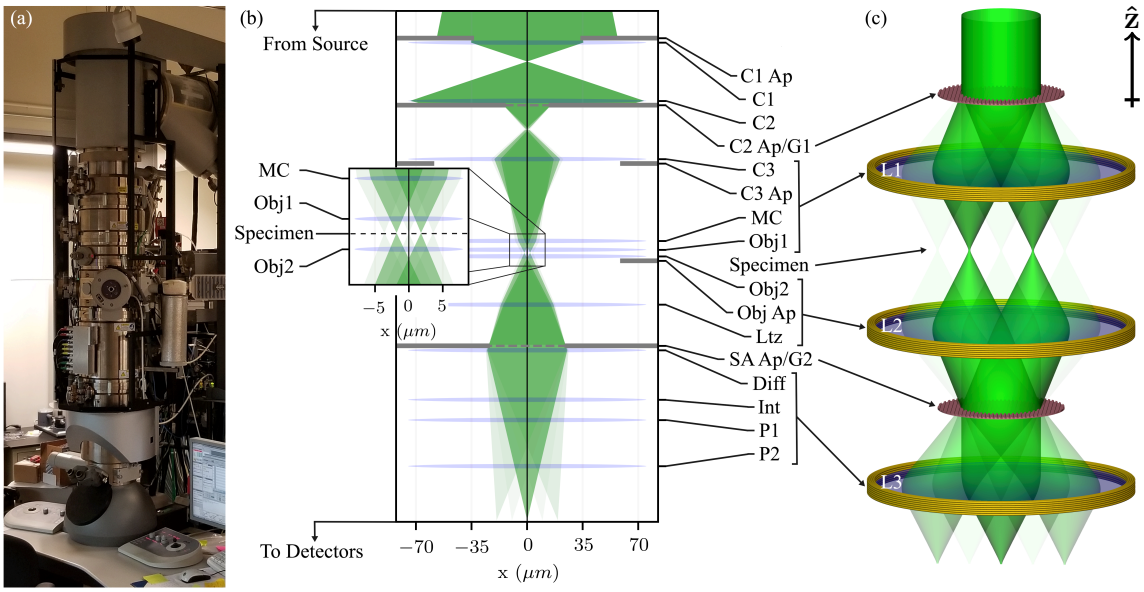

FIGURE 1.3. (a) Photograph of an image-corrected FEI Titan TEM. (b) Ray tracing diagram of TEM with the approximate relative spacing between the magnetic lenses and apertures consisting of: condenser lenses (C1, C2, C3) and condenser apertures (C1 Ap, C2 Ap, C3 Ap), mini-condenser and objective lenses at the specimen section (MC, Obj1, Obj2), an objective aperture (Obj Ap), a Lorentz lens (Ltz), a selected-area aperture (SA), as well as a diffraction, intermediate, and two projector lenses (Diff, Int, P1, P2). Shown in a two-grating interferometer configuration with input grating (G1) and output grating (G2) placed in the C2 Ap and SA Ap planes respectively. (c) Illustration of two-grating interferometer showing what abstract optical component corresponds to in the TEM.

lens groups and apertures correspond to the abstract illustration components that will be used throughout this dissertation.

One important note not captured in the illustration in Figure 1.3(c) is that the post-specimen projection lenses can easily provide up to a ×1,000,000 magnification between the specimen and detector planes in this configuration. Additionally, these lenses can be adjusted to display an image of the aperture planes above and below the specimen. At the bottom of the column there are various detectors: a charge-coupled device (CCD) camera capturing two-dimensional intensity images of the transverse electron wavefunction at a given $z = z_0$ plane, $|\psi(\mathbf{R}, z_0)|^2$; monolithic detectors that measure different radial sections of the scattered intensity for every specimen scanning probe location, a brightfield (BF) detector for the central region, $\int d\varphi \int_0^{R_0} dR\, R|\psi(\mathbf{R}, z_0)|^2$, and high-angle annular darkfield detector (HAADF) for an annular region around the optical axis, $\int d\varphi \int_{R_1}^{R_2} dR\, R|\psi(\mathbf{R}, z_0)|^2$, with $R_0 \ll R_1 < R_2$; and an electron energy loss spectrometer (EELS) that disperses the electrons with magnetic prism to measure the spectrum of the electrons, $|\psi(\omega)|^2$.

1.2.4. Coherent Transmission Through Materials

When electrons in a TEM enter a thin amorphous material, as depicted in Figure 1.4, they experience an electrostatic potential due to the average value of all the atomic potentials called the mean inner potential U_{mip}. This mean inner potential contributes to the kinetic energy of the electron and modifies the longitudinal wavenumber as

$$k_z(U_{\text{mip}}) = \frac{1}{\hbar c}\sqrt{(E_{KE} + eU_{\text{mip}})^2 + 2(E_{KE} + eU_{\text{mip}})m_e c^2}. \tag{1.6}$$

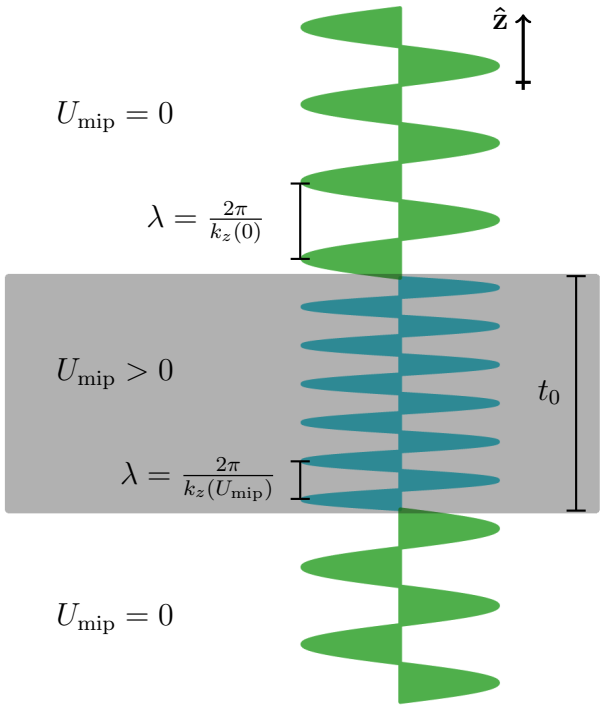

FIGURE 1.4. Diagram of electron longitudinal plane-wave passing through a thin material with thickness t_0 and a positive mean inner potential. Depicted here is a positive mean inner potential giving rise to a decreased de Broglie wavelength in the material, for materials with a negative mean inner potential it would increase.

This is similar to the refractive index for light. At normal operating conditions the case that $eU_{\text{mip}} \ll E_K$ is satisfied and we can approximate Equation (1.6) with the first two terms of its Taylor expansion about eU_{mip}/E_K

$$\begin{aligned} k_z(U_{\text{mip}}) &= k_z(0) + \frac{e\, m_{rel}\lambda_{rel}}{2\pi\hbar^2} U_{\text{mip}} + \mathcal{O}\left(\left(\frac{eU_{\text{mip}}}{E_{KE}}\right)^2\right) \\ &\approx k_z(0) + \sigma U_{\text{mip}}, \end{aligned} \tag{1.7}$$

where $\sigma = em_{rel}\lambda_{rel}/2\pi\hbar^2$ is called the interaction parameter that is independent of any material parameters for an electron with relativistic mass $m_{rel} = m_e + E_{KE}/c^2$ and relativistic de Broglie wavelength $\lambda_{rel} = hc/\sqrt{E_{KE}^2 + 2E_{KE}m_e c^2}$.

Within the material the electron's longitudinal wavefunction is modified by the first order expansion in the wavenumber $\psi_z(z) = \exp(ik_z(0)z)\exp(i\sigma U_{\text{mip}}z)$. This additional phase changes the wavelength in the material, but electrons return to their initial kinetic energy upon exiting the material, (Fig. 1.4). Provided that the material thickness, t_0, is sufficiently small so dynamical diffraction can be ignored within the material, the phase accumulated by passing through the material can be found by integrating across the thickness of the material, projecting the total phase shift in the transverse plane $\int_0^{t_0} dz\, \sigma U_{\text{mip}} = \sigma U_{\text{mip}} t_0 = \Phi t_0$. What has not been discussed so far is that there are many elastic and inelastic high angle scattering processes that can occur within the material that are highly dependent on the material properties as well as the acceleration energy. It would be a tedious, but possible task to calculate the probability of all of these scattering processes for a given material. However, since these processes just eject electrons outside of the collection apertures of the optical system in the TEM column, we can empirically find a Beer's law like "absorption" coefficient which can be written as the complex part of the phase shift $\widetilde{\Phi} = \sigma U_{\text{mip}} + i\alpha$.

In general, the thickness of the material is not required to be uniform across the transverse directions. If the thickness varies in the transverse plane $t(\mathbf{R})$, with $\mathbf{r} = (\mathbf{R}, z)$, then after transmission through the material the electron wavefunction becomes

$$\psi(\mathbf{r}) \propto \exp(ik_z(0)z)\exp(i\widetilde{\Phi}\, t(\mathbf{R})). \tag{1.8}$$

A material that can form hard, homogeneous, low-stress, free standing thin films with small high angle scattering probabilities $\alpha \ll \sigma U_{\text{mip}}$, that supports nanofabricated depth profiles, $t(\mathbf{R})$, can then be used as diffraction holograms. For example, we use Si_3N_4, which has the properties $\sigma U_{\text{mip}} \approx 0.15$ rad·nm^{-1} and $\alpha \approx 0.008$ nm^{-1}.

1.2.5. Electron Energy Loss Due to Electromagnetic Interactions

In addition to the elastic interactions that are described in the previous section, there can be a significant probability that electrons can be inelastically scattered. Here I summarize the mechanism for energy loss via interactions with induced electromagnetic fields.

1.2.5.1. Classical Approach

Consider an electron propagating down the column of a TEM with velocity $\mathbf{v} = -v\hat{\mathbf{z}}$ (Fig. 1.5). Classically, this can be described as a delta function charge density along a time dependent path, $\rho(\mathbf{r},t) = e\delta(\mathbf{r}-\mathbf{r}_0(t))$, where the time dependent path can be written explicitly as $\mathbf{r}_0(t) = (R_0\cos(\varphi_0), R_0\sin(\varphi_0), z_0 - vt)$. This charge density has a corresponding current density $\mathbf{J}(\mathbf{r},t) = e\mathbf{v}\delta(\mathbf{r}-\mathbf{r}_0(t))$, which in frequency space is given by

$$\begin{aligned}\widetilde{\mathbf{J}}(\mathbf{r},\omega) &= \int dt\, e^{i\omega t}\mathbf{J}(\mathbf{r},t) \\ &= -\frac{e\mathbf{v}}{v}\delta(\mathbf{R}-\mathbf{R}_0)e^{i\omega(z-z_0)/v}.\end{aligned} \tag{1.9}$$

The charge of a fast electron produces a time dependent external electric field $\mathbf{E}^{\text{ext}}(\mathbf{r},t)$, which in frequency space is given by $\widetilde{\mathbf{E}}^{\text{ext}}(\mathbf{r},\omega) = \int dt\, e^{i\omega t}\mathbf{E}^{\text{ext}}(\mathbf{r},t)$.

Now consider an arbitrary nanostructure whose optical response is determined by the dielectric function $\boldsymbol{\epsilon}(\mathbf{r},\omega)$. The nanostructure response to the external electric field from the passing electron results in an induced electric field denoted as, $\mathbf{E}^{\text{ind}}(\mathbf{r},t)$ and $\widetilde{\mathbf{E}}^{\text{ind}}(\mathbf{r},\omega) = \int dt\, e^{i\omega t}\mathbf{E}^{\text{ind}}(\mathbf{r},t)$. This induced electric field can be written in terms of the current density of the fast electron and the dyadic Green's function of the

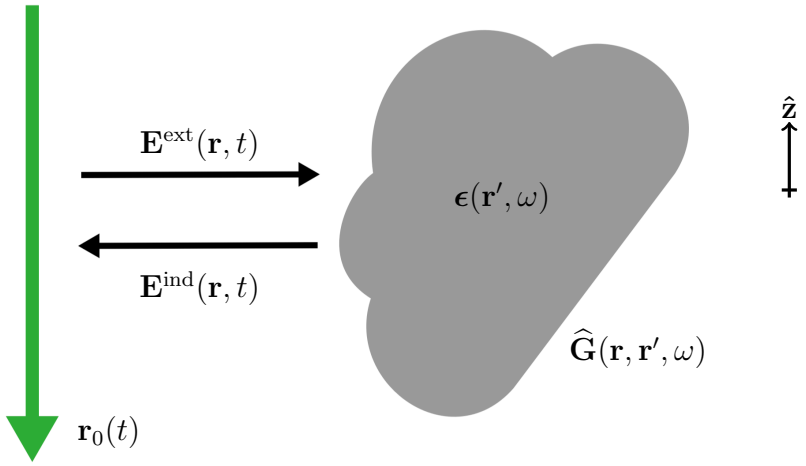

FIGURE 1.5. Illustration of a classical point electron on passing through the electric field from a plasmonic nanostructure induced by the dielectric response to the external electric field from the passing electron itself that results in a EELS probability Γ.

nanostructure

$$\widetilde{\mathbf{E}}^{\text{ind}}(\mathbf{r},\omega) = -4\pi i\omega \int d^3\mathbf{r}'\, \widehat{\mathbf{G}}(\mathbf{r},\mathbf{r}',\omega)\cdot\widetilde{\mathbf{J}}(\mathbf{r}',\omega), \tag{1.10}$$

where $\widehat{\mathbf{G}}(\mathbf{r},\mathbf{r}',\omega)$ is the solution to

$$\boldsymbol{\nabla}\times\boldsymbol{\nabla}\times\widehat{\mathbf{G}}(\mathbf{r},\mathbf{r}',\omega) - \frac{\omega^2}{c^2}\boldsymbol{\epsilon}(\mathbf{r},\omega)\widehat{\mathbf{G}}(\mathbf{r},\mathbf{r}',\omega) = -\frac{1}{c^2}\delta(\mathbf{r}-\mathbf{r}'), \tag{1.11}$$

this differential equation can be derived directly from Maxwell's equations (Fig. 1.5) [29].

The induced electric field does work on the passing electron resulting in a loss of energy

$$\Delta E = e\int dt\,\mathbf{v}\cdot\mathbf{E}^{\text{ind}}_{\mathbf{r}_0}(\mathbf{r}_0(t),t) = \int_0^\infty d\omega\,\hbar\omega\Gamma(\omega), \tag{1.12}$$

where the subscript in $\mathbf{E}^{\text{ind}}_{\mathbf{r}_0}$ is included to denote that the induced field is produced from the electron on the path $\mathbf{r}_0(t)$ and is evaluated at $\mathbf{r}_0(t)$, and $\Gamma(\omega)$ is the

probability of losing $\hbar\omega$ amount of energy per unit ω. The loss probability can then be written as

$$\Gamma(\omega) = \frac{e}{\pi\hbar\omega}\int dt\,\mathrm{Re}\left\{e^{-i\omega t}\mathbf{v}\cdot\widetilde{\mathbf{E}}^{\mathrm{ind}}_{\mathbf{r}_0}(\mathbf{r}_0(t),\omega)\right\}. \tag{1.13}$$

Using the dyadic Green's function representation of the induced field with the substitution of time integral coordinates $z = z_0 - vt$ and $dt = dz/v$ gives

$$\Gamma(\mathbf{R}_0,\omega) = \frac{4e^2}{\hbar}\int dz\,dz'\,\cos\left(q_z(z-z')\right)\mathrm{Im}\left\{-\hat{\mathbf{z}}\cdot\widehat{\mathbf{G}}(\mathbf{R}_0,z,\mathbf{R}_0,z',\omega)\cdot\hat{\mathbf{z}}\right\}, \tag{1.14}$$

where $q_z = \omega/v$ [30]. With this we can calculate the energy loss spectrum we would expect to see using an EELS spectrometer to predict an expected result or compare to experimental measurements.

1.2.5.2. Quantum Approach

A more rigorous result can be derived quantum mechanically by calculating the transition rate probability using Fermi's golden rule. This is done by considering the fast electron wavefunction $\psi_i(\mathbf{r}) = \psi_{i\perp}(\mathbf{R})e^{ik_z z}$ exciting the solid state electron density operator $\hat{\boldsymbol{\rho}}$ from its ground state to an excited state, $|g\rangle \rightarrow |e\rangle$, via the Coulomb interaction Hamiltonian, $H^{\mathrm{int}} \propto |\mathbf{r}-\mathbf{r}'|^{-1}$, where $\mathbf{r}$ and $\mathbf{r}'$ are the source and field points of the electric potential. Within this formulation we can determine the loss probability in terms of the final transverse momentum distribution of the scattered wave, $\mathbf{K}$ (Fig. 1.6). Under the assumptions that the gradient of the transverse wavefunction is much smaller than the longitudinal plane wave,

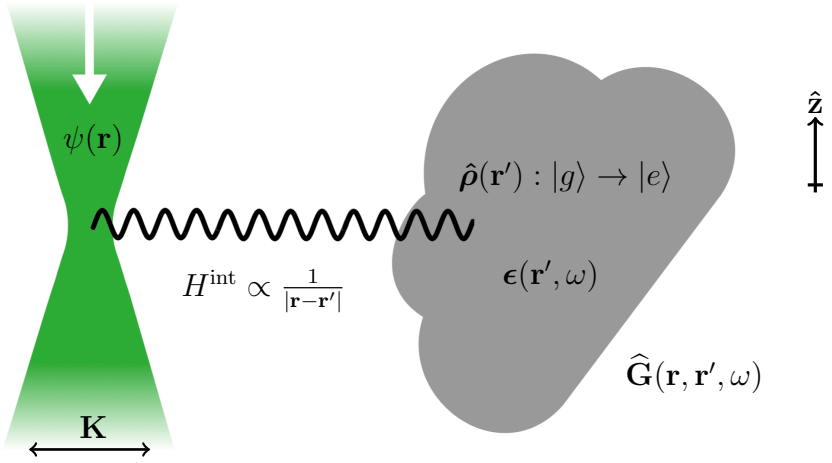

FIGURE 1.6. Illustration of an electron wavefunction exciting the condensed matter electrons in a plasmonic nanostructure to a higher energy state via the Coulomb interaction Hamiltonian resulting in an EELS probability that can be resolved by final transverse momenta $d\Gamma/d\mathbf{K}$.

the non-recoil approximation $\omega = \mathbf{q} \cdot \mathbf{v} - \hbar q^2/2m_e \approx \mathbf{q} \cdot \mathbf{v}$ for the incident plane wave wavevector $\mathbf{q}$, and delta function normalization of the final states, then in this formalism the momentum resolved EELS probability can be written as

$$\begin{aligned}\frac{d\Gamma(\omega)}{d\mathbf{K}} = \frac{e^2}{\pi^2\hbar} \int d^2\mathbf{R}\, d^2\mathbf{R}'\, \psi_{i\perp}^*(\mathbf{R})\psi_{i\perp}(\mathbf{R}')e^{i\mathbf{K}\cdot(\mathbf{R}-\mathbf{R}')} \\ \times \int dz dz'\, e^{-iq_z(z-z')} \text{Im}\left\{-\hat{\mathbf{z}} \cdot \widehat{\mathbf{G}}(\mathbf{r}, \mathbf{r}', \omega) \cdot \hat{\mathbf{z}}\right\}\end{aligned} \tag{1.15}$$

[30]. Integrating over all possible final transverse momenta gives the intuitive result

$$\Gamma(\omega) = \int d\mathbf{K} \frac{d\Gamma(\omega)}{d\mathbf{K}} = \int d^2\mathbf{R} |\psi_{i\perp}(\mathbf{R})|^2 \Gamma(\mathbf{R}, \omega), \tag{1.16}$$

where $\Gamma(\mathbf{R}, \omega)$ is the same as Equation (1.14) from the classical formalism.

1.3. Dissertation Outline

This dissertation is laid out in two main sections: The first pertains to the design, fabrication, and measurement of material holograms for free electrons that split the transmitted beam into multiple off-axis diffraction orders. Chapter 2 covers the development of focused ion beam gas-assisted etching as a reliable nanofabrication process for making straight diffraction gratings with ideal diffraction efficiencies for a given groove profile. Chapter 3 covers the development of an analytical theory for the design of off-axis holograms that can be used to arbitrarily shape the amplitude and phase of the transverse wavefront of a single diffraction order and an experimental implementation is demonstrated. The second section is on the application of these nanofabricated gratings to grating-based electron interferometry. Chapter 4 covers the construction of a scanning two-grating electron Mach-Zehnder interferometer in a TEM and demonstrates its phase sensitivity to electrostatic fields and an application for quantitative phase imaging. Chapter 5 covers the theoretical treatment of plasmon scattering in the grating interferometer for multiple coherent probes incident on a single metallic nanoparticle and the interference in the interferometer output. Chapter 6 covers an experimental demonstration of this inelastic interference on isolated gold spherical nanoparticles. Finally, chapter 7 provides an outlook for future experiments that can be performed with the electron interferometer and provides a conclusion for the dissertation.

This dissertation contains previously published and unpublished material.

CHAPTER II

FIB GAE FABRICATED DIFFRACTION HOLOGRAMS

Notes for Ch. II:

This chapter is adapted from the published research article:
[31] **C. W. Johnson**, D. H. Bauer, and B. J. McMorran. Improved Control of Electron Computer-Generated Holographic Grating Groove Profiles Using Ion Beam Gas-Assisted Etching. *Applied Optics*, 59(6):1594-1601, 2020.

BJM and I developed the study for the paper. DHB assisted in designing the gratings and helped measure diffraction efficiencies for the tilted incidence portion of the experiment. I performed the nanofabrication, the measurements and wrote the paper.

An off-axis hologram's groove profile can be generated by simulating the interference pattern of a reference wave and a wave with a desired phase to encode, then imprinting that interference pattern into a phase-shifting material for an incident plane wave [32]. The desired phase from the hologram is imparted to the incident wave upon transmission. Given a material that can impart a thickness-dependent phase shift to a wave medium, holograms can be created for any medium which creates complex scalar waves such as photons, electrons, neutrons, atoms, and molecules [33, 34, 35, 36, 37]. Holograms have been used for decades to shape electromagnetic waves and have recently been applied to the field of matter wave optics that exploit the particle-wave properties of massive quantum particles first proposed by de Broglie in 1924 [4].

Conventional transmission electron microscopes (TEMs) operating at accelerating voltages ranging from 60-300 kV, resulting in electron wavelengths of 5-2 pm respectively, routinely achieve atomic resolution and have been instrumental at increasing our understanding of material properties at the nanoscale. In the past decade researchers have been developing holograms to structure the profile of electron waves in TEMs with the hope to create new tools able to measure new degrees of freedom that are undetectable within conventional electron microscopy [38]. Many of these efforts have been to create holograms that produce electron vortex beams (EVBs) which carry quantized amounts of orbital angular momentum aiming to develop nanoscale, symmetry-breaking dichroism type measurements [18, 39]. Holograms for electrons have also shown to be useful for aberration correction [40, 41, 42], interferemetric 4D scanning TEM [43, 44], and exploring fundamental properties of free electrons [45]. The biggest hindrances to holograms having a large impact in these research areas are two-fold. The first problem is efficiency; the groove profile of a hologram must be precisely controlled in order maximize the diffraction efficiency into a desired diffraction order while simultaneously minimizing all the other diffraction orders to reduce background noise. The second problem is scalability; the holograms must be large enough to have a sufficient intensity in the desired diffraction order. Previous efforts have been able to address one of these issues at a time, but there has not been a nanofabrication method to create holograms that overcomes both of these problems simultaneously.

Holograms for electrons can be amplitude-type, consisting of arrays of slits milled all the way through a material only allowing transmission through the slits [46, 47, 48], or phase-type, consisting of grooves in an electron-transparent material like silicon nitride (Si_3N_4) of a particular depth to introduce a thickness-dependent

phase shift [49, 50, 51]. The two most successful nanofabrication methods for creating electron phase holograms have been focused ion beam (FIB) milling and electron beam lithography (EBL) [52, 53]. FIB milling sputters material away by physical momentum transfer and easily allows for arbitrary groove profiles, ultimately limited by the size of the intensity distribution of the FIB and the redeposition of the sputtered material back on the hologram. FIB milling also requires very low currents, $\sim$10 pA, to achieve the best resolution. Implantation of gallium from the FIB process introduces a nontrivial scattering and phase shifts onto transmitted electrons as well causing membrane swelling and stretch, further complicating the manufacture and efficiency of holograms [34]. Consequently, FIB milling is good at arbitrarily controlling the efficiency of holograms, but is difficult to create holograms large enough to fill condenser apertures of a typical TEM, $\sim$50 μm and introduces unwanted material defects. EBL has an even better resolution than FIB milling and can easily pattern 50 μm, but it is difficult to implement arbitrary groove profiles without introducing more processing steps to the nanofabrication process, significantly increasing the chance of process failure. This makes it nearly impossible to create single Si_3N_4 membranes with multiple holograms using EBL or any lithographic technique; it is much more practical to have a single membrane with multiple holograms placed in a condenser aperture of a TEM, as replacing a condenser aperture for each application is undesired on a shared user instrument. This means EBL is a scalable process, but does poorly at creating multiple holograms with differing arbitrary groove profiles needed to maximize efficiencies.

Indeed, different nanofabrication processes other than FIB milling and EBL as well as different host materials other than Si_3N_4 have been explored in previous studies [54, 55, 56]. These different processes still lack all the necessary attributes,

such as scalability, resolution, and consistency, required for the fabrication of holograms. While different membrane materials have arguably better physical properties than Si_3N_4 for holograms, ease of manufacture and commercial availability of high quality, low stress, thin Si_3N_4 make it an ideal host material.

Introducing a concurrent gas-assisted etching (GAE) process to the FIB milling procedure selectively catalyzes a dry chemical etch where the FIB is being rastered. This chemical etching process works by adsorbing to the material surface and disassociating to reactive ionic components, then wherever the material has been weakened by the scanning FIB the reactive ions capture material to form volatile compounds that out-gas and pumped from the vacuum chamber. This removes much of the material whose structure has been altered and implanted with ions. As a result, all the positive attributes of FIB milling such as reproducibility, and spatial depth variability are kept, while simultaneously increasing resolution by decreasing process time, stage drift, and material redeposition. FIB GAE is a robust single-step nanofabrication process for the creation of highly efficient electron phase holograms that can be scaled to fill the apertures in TEMs.

2.1. Holograms Made Using FIB GAE

2.1.1. Nanofabrication Methods

All of the FIB GAE presented here was performed in a FEI Helios Dual Beam FIB - 600 using Ga^+ ions. We use XeF_2 as the etchant gas, which is commercially available in FEI dual beam FIB instruments. XeF_2 has been shown to increase the sputtering rate of Si based materials by up to factor of 12 for Ga^+ ion beam milling [57].

To characterize the effectiveness of FIB GAE we chose three standard holograms groove profiles - binary, sinusoidal, and blazed - that can each be optimized for various applications in electron beam engineering. We made a total of 36 holograms, 12 for each groove profile shape with increasing groove depth, all with 200 nm pitch and 12 μm diameter. The ion beam current and accelerating energy was held constant for all mills at 7.7 pA and 30 keV respectively. The binary holograms were made with a single raster pattern with total ion doses varying linearly from 2.5-21.9 pC/μm^2. To intentionally fabricate a pattern with a continuous, spatially varying groove profile we can create a set of multiple raster patterns with slightly varying pitch duty cycles, that when milled in sequence produces the intended groove shape. The sinusoidal hologram were made by repeating a sequence of 7 different raster patterns with total ion doses from 3.8-31.5 pC/μm^2. The blazed holograms were made by repeating a sequence of 19 different raster patterns with total ion doses from 3.4-36.4 pC/μm^2. The XeF_2 gas was introduced through a commercial gas injection needle approximately 1 mm above the milling region. Examples of the groove profiles made can be seen in Figure 2.1.

2.1.2. Diffraction Efficiency

For weakly interacting objects in a TEM, the amplitude and phase of the transmitted electron wave are changed proportionally to the spatially varying thickness of the hologram, $t(\mathbf{R})$, dependent on the materials properties of the hologram [58]. For an incident electron wavefunction $\psi_0(\mathbf{R})$, incident on a material with varying thickness $t(\mathbf{R})$ with a phase shift per nm, Φ_0, and 'absorption' per nm, α, then the wavefunction directly after the hologram can be written as $\psi(\mathbf{R}) = \psi_0(\mathbf{R})e^{i\widetilde{\Phi}t(\mathbf{R})}$, where $\widetilde{\Phi} = \Phi_0 + i\alpha$. We introduce the 'absorption' term α to

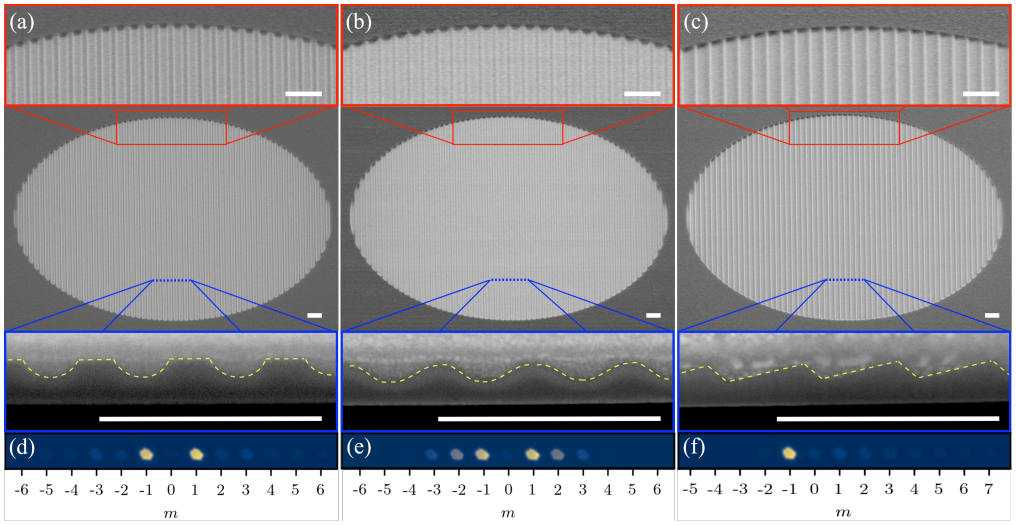

FIGURE 2.1. Example 12 μm diameter, 200 nm pitch holograms with (a) binary, (b) sinusoidal, (c) blazed groove profiles. All white scale bars are 500 nm. Milled in 100 nm thick free standing Si_3N_4 membrane with a 5 nm titanium/platinum charge alleviation layer on the underside, viewed at 52° angle in a scanning electron microscope. Red insets are zoomed sections on the hologram upper edge. Blue insets are FIB cross-sections showing a platinum cap layer (only present for cross-sectioning), a typical Si_3N_4 groove profile, a titanium/platinum charge alleviation layer (high contrast line at bottom), and vacuum underneath; the dashed yellow lines trace the interface of the platinum cross-sectioning cap and the actual hologram groove profile. (d-f) Normalized, defocused far field diffraction patterns from holograms with mill depths designed to produce the ideal diffraction properties of each groove profile.

account for electrons scattered by the Si_3N_4 membrane at high angles outside of the collection aperture of the optical system. If we write the output electron wave as a one dimensional Fourier series in the diffraction direction, assuming plane wave illumination with an amplitude $|\psi_0(\mathbf{R})| = 1$, the magnitude squared Fourier coefficients are the absolute diffraction efficiencies from the hologram,

$$\eta_m = |c_m|^2 = \left| \frac{1}{x_0} \int_0^{x_0} e^{i(\widetilde{\Phi} t(x) - 2\pi m x / x_0)} dx \right|^2, \tag{2.1}$$

where x_0 is the pitch of the hologram and $m \in \mathbb{Z}$ is the diffraction order. These efficiencies can be normalized giving efficiencies relative to total transmitted wave,

$$\eta_m^{(r)} \equiv \frac{\eta_m}{\sum_{k\in\mathbb{Z}} \eta_k}. \tag{2.2}$$

We placed holograms in the specimen plane of an FEI Titan TEM and expanded convergence angle of the electron beam for plane wave illumination. The lenses after

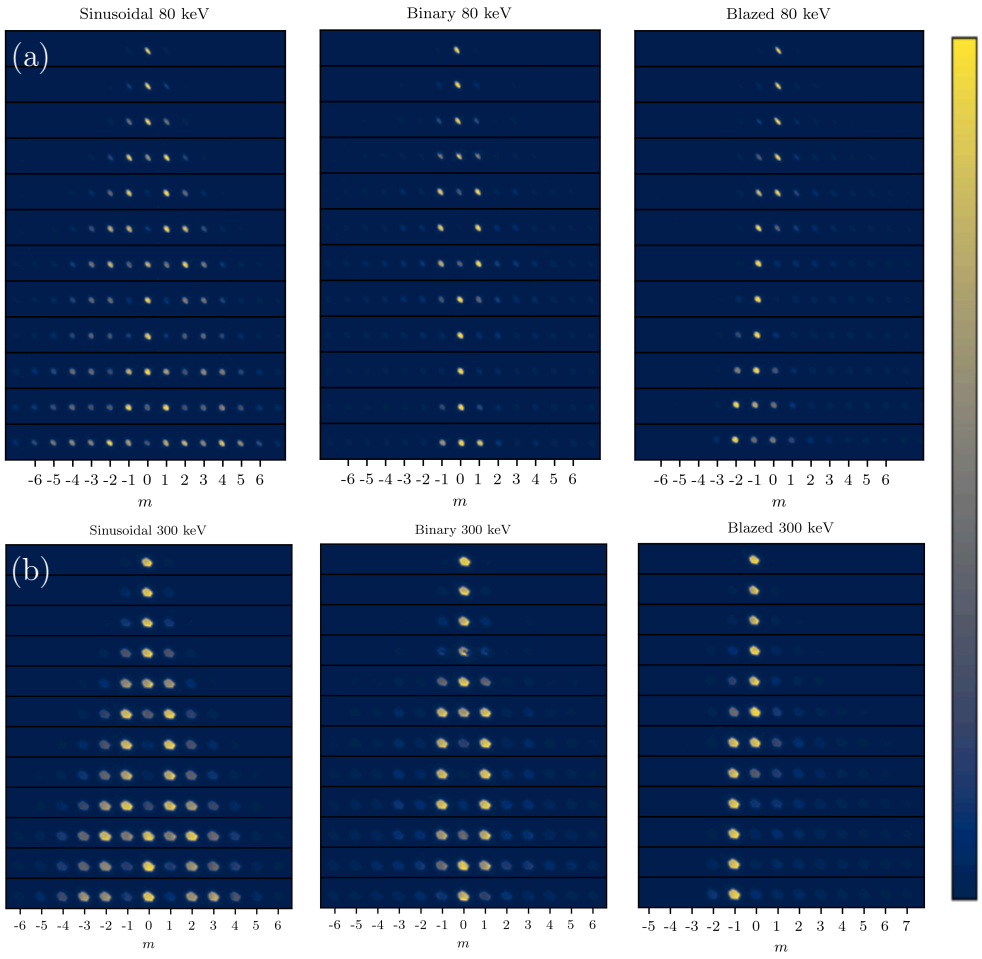

FIGURE 2.2. Defocused far field diffraction intensity patterns from FIB GAE nanofabricated diffraction grating arrays measured in a TEM at (a) 80 keV and (b) 300 keV. Sinusoidal, binary, and blazed groove profile gratings from left to right respectively. From top to bottom is increasing mill depth by linearly increasing the FIB dose.

the specimen plane were used to project the focal plane of the holograms onto the CCD detector at the bottom of the TEM column. This was performed with both 80 and 300 keV electrons for every grating Figure 2.2

As is clear from Figure 2.1, we note that we have slight deviations from the ideal profiles for the binary and blazed cases; these deviations can be attributed to material redeposition and the finite width of the ion beam used to mill and catalyze the chemical etch [59]. To model the thickness of the binary groove profile, $t(\mathbf{R})$, we replace the bottom of the square trough with the lower half of an ellipse. For the sinusoidal case, we use a sine function. For the blazed case, we use two linear ramps with opposite slopes. The modelled thickness profile of a single groove period, $0 < x \leq x_0$, of each hologram can be explicitly written as

$$t(x) = \begin{cases} t_0 - d\,\Theta(x_0/2 - x)\left((1 - f_{bi}) + f_{bi}\sqrt{\left(\frac{x_0}{4}\right)^2 - \left(x - \frac{x_0}{4}\right)^2}\right); & \text{Binary} \\ t_0 - d\sin^2(\pi x/x_0); & \text{Sinusoidal} \\ t_0 - d\left(\Theta(x_0 f_{bl} - x)\frac{x}{x_0 f_{bl}} - \Theta(x - x_0 f_{bl})\frac{x - x_0}{x_0(1 - f_{bl})}\right); & \text{Blazed} \end{cases} \tag{2.3}$$

where t_0 is the thickness of the Si_3N_4 membrane, d is the groove depth, f_{bi} is what vertical fraction of the binary groove has the ellipsoidal shape, f_{bl} is the fraction of the pitch with the positive slope, and $\Theta(x)$ is the Heaviside step function. We use the values $f_{bi} = 0.6$ and $f_{bl} = 0.13$ that were used by fitting to the yellow dashed curves in Figure 2.1.

The first-order phase shift per nanometer of any non-magnetic material can be decomposed into the mean inner potential of the material and an electron energy dependent interaction parameter $\varphi_0 = U_{mip}\sigma(E)$, where $\sigma(E) = 2\pi e(E + m_e c^2)/hc\sqrt{2Em_e c^2 + E^2}$ [58]. We use the previously measured value $U_{mip} = 15$

V [60]. The 'absorption' per nanometer was found experimentally to be $\alpha = 0.008 \pm 0.001$ nm^{-1} by comparing the integrated intensity of an electron beam passing through vacuum and through a uniform membrane of Si_3N_4 with a known thickness.

The measured relative relative diffraction in Figure 2.3. These efficiencies were found by summing all of the pixel values in a 80×80 pixel square around each diffraction order in Figure 2.2, then normalizing by the sum of all pixel values in the recorded diffraction pattern image. The uncertainties were found by applying Poisson counting statistics to the count of pixel values in each box, normalizing to the total pixel value sum of the image, then an extra 1% uncertainty was added in quadrature to account for higher diffraction orders not recorded by the CCD.

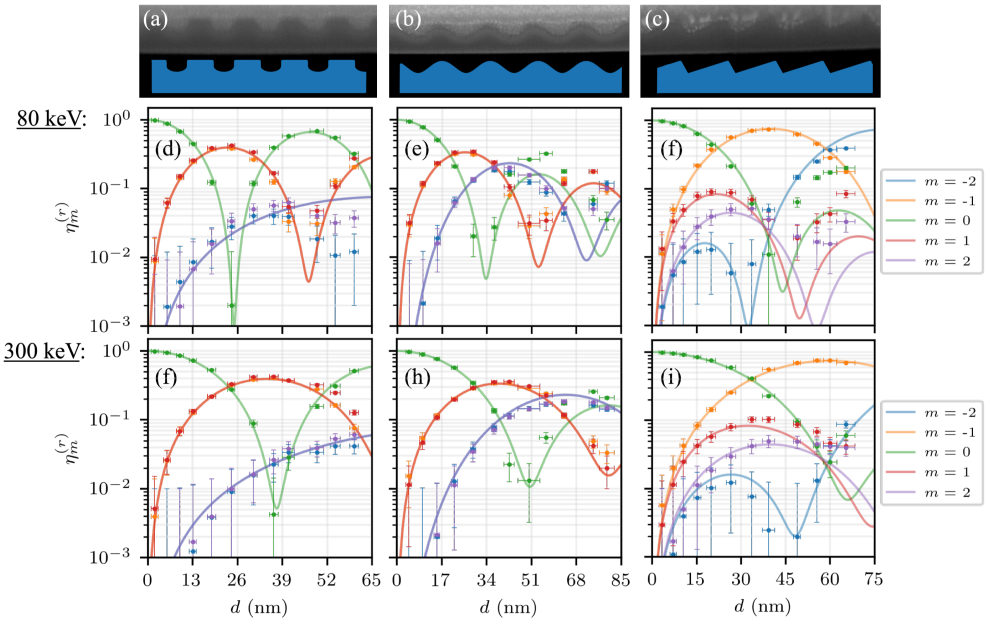

FIGURE 2.3. (a,b,c) SEM micrographs of ion milled cross-sections of binary, sinusoidal, and blazed holograms respectively; blue profiles are the modelled groove profiles $t(x)$ from Equation (2.3) for simulated diffraction efficiencies. Experimentally measured relative diffraction efficiencies, $\eta_m^{(r)}$, of the first 5 diffraction orders, m, as a function of hologram groove depth, d, for the array of 36 test holograms, (d,e,f) at 80 keV for binary, sinusoidal, and blazed holograms respectively, (f,h,i) and at 300 keV for binary, sinusoidal, and blazed holograms respectively. The dots with error bars are the measured values, and the solid curves are the fits from Equation (2.2).

The mill depths were estimated by taking the mean of least squares fits of Equation (2.2) for the appropriate groove profile with d used as the only fit parameter. The uncertainties in mill depth were found by adding the standard deviation of the two fit mill depths as well as an extra 1 nm uncertainty added in quadrature to account for any systematic deviation from the expected groove shapes defined in Equation (2.3). The first 5 diffraction order relative efficiencies are in good agreement with Equation (2.2) up to about a 50 nm mill depth. We attribute this deviation for mill depths greater than 50 nm to the appreciable aspect ratios between depth and pitch causing an increased rate of redeposition from sputtered and etched material in the milled hologram trenches, changing the expected groove profile.

2.1.3. Tilted Incidence of Blazed Hologram

The phase shift a thin material applies to a passing electron wave is due to the interaction with the inner potential $U_{ip}(\mathbf{r})$ of the material projected along the z-axis $\Phi(\mathbf{R}) = \sigma(E)\int_0^{t(\mathbf{R})} U_{ip}(\mathbf{r})dz$. Since Si_3N_4 is amorphous, we can average the electric potentials from the atomic sites in the material giving a mean inner potential $U_{mip} = \langle U_{ip}(\mathbf{r})\rangle_{\mathbf{r}}$, allowing us to write

$$\Phi(\mathbf{R}) = \sigma(E)U_{mip}\int_0^{t(\mathbf{R})} dz = \Phi_0 t(\mathbf{R}). \tag{2.4}$$

For a hologram, the thickness function $t(\mathbf{R})$ in Equation (2.4) is assumed to be oriented parallel to the electron wave fronts. If the hologram is tilted with respect to the optical axis, $t(\mathbf{R})$ is not the thickness of the material normal to the plane of the hologram, it is the projection of the thickness along the propagation direction of the electron as a function of the tilt angle $t(\theta, \mathbf{R})$ (Fig. 2.4(a)). We used this to

design a 450 nm pitch, 15 μm diameter blazed grating whose maximum first order relative diffraction efficiency is increased from 74% to 88% by changing the incidence angle by 30° (Fig. 2.4(b,c)). In principle, a hologram could be made that has a near perfect relative diffraction efficiency in the first diffraction order $\eta_1^{(r)}$ ≈100%, limited by the 'absorption' α, caused by high angle scattering within the hologram material. We kept the hologram pitch below 500 nm to retain pattern scalability, and only considered up to 30° tilt angles for practical considerations of the TEM sample holder. The larger tilt angles up to 30° certainly push the limits of the weak phase approximation and treatment as a flat optical element. When scaling up to larger diameter gratings it may be necessary to include wave propagation to the analysis.

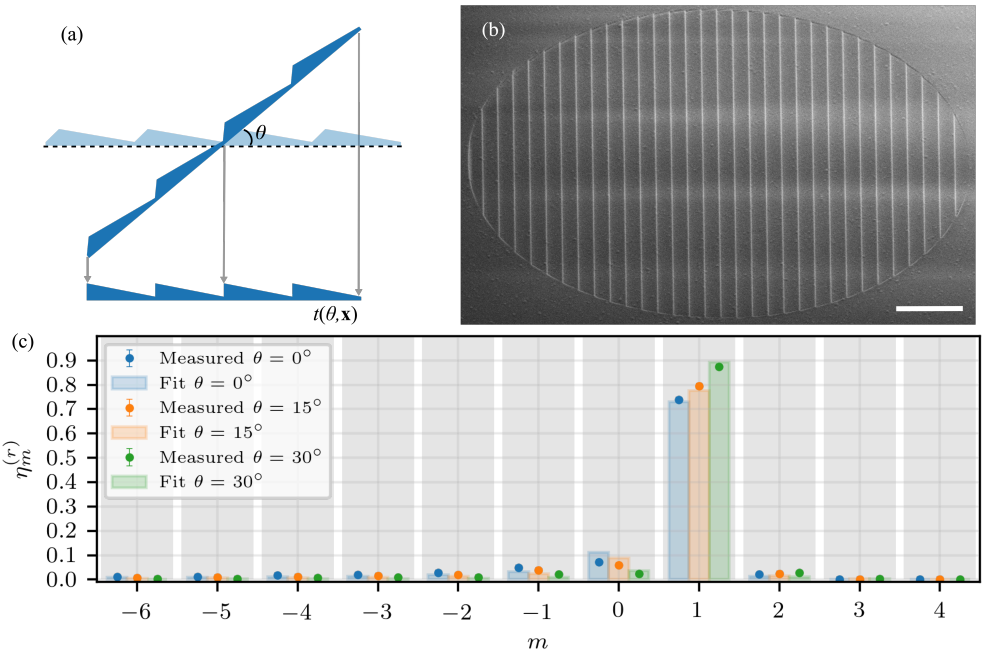

FIGURE 2.4. (a) SEM micrograph of a 450 nm pitch, 15 um diameter hologram, white scale bar is 2 μm. (b) Diagram showing the geometry of tilted hologram and how the projection of the thickness profile of the hologram changes with incidence angle. (c) Measured relative diffraction efficiencies of the hologram from (a) at three different incidence angles with the predicted values from Equation 2.

2.2. Practical Considerations

2.2.1. Scalability and Applications

To highlight the scalability and immediate applications of the FIB GAE nanofabrication method we made two 50 μm diameter, 100 nm thick holograms. First is a blazed 200 nm pitch hologram with an azimuthally varying spatial phase creating an electron vortex beam that can be used in nanoscale magnetic and plasmonic dichroism experiments [18, 39]. Second is a binary 125 nm pitch hologram that can be used as an amplitude dividing beam splitter for electron interferometry and phase sensitive electron microscopy [61]. The two holograms required 45 minute and 30 minute mill times, respectively.

Electron vortex beams are a relatively new class of electron beam that possesses orbital angular momentum (OAM). The OAM is associated with an azimuthally varying spatial phase that can be imprinted on the beam in a number of ways [62], including a hologram with a fork dislocation [48, 51, 52]. These beams show promise for probing chiral excitations in matter [18, 63], measuring atomic magnetic moments [39], and manipulating nanoparticles [64]. However, these applications are severely limited by low beam current, and effects caused by nearby diffracted beams. The use of FIB GAE allows better control over the groove profile and faster mill times, which provides the ability to improve both diffraction efficiency and effective aperture size. The 50 μm blazed forked hologram has a relative diffraction efficiency (Eqn. (2.2)) $\eta_1^{(r)} = 68\%$ and no more than 7% of the total transmitted intensity into any other diffracation order at 200 keV, and with $\alpha = 0.008$ nm^{-1}, the absolute diffraction efficiency (Eqn. (2.1)) is $\eta_1 \approx 22\%$ (Fig. 2.5(a)). The previous highest reported

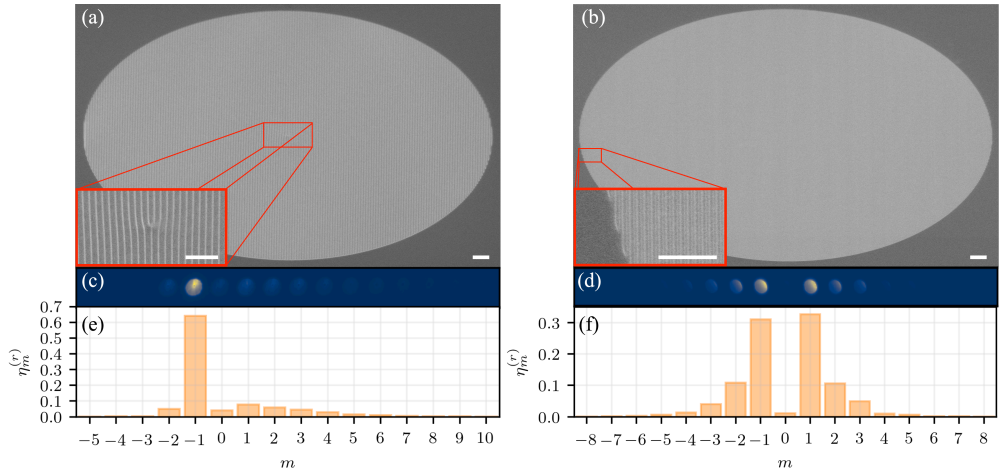

FIGURE 2.5. (a) 50 μm diameter, 200 nm pitch, 1 OAM blazed hologram. (b) 50 μm diameter, 125 nm pitch, straight binary hologram. Top images are SEM micrographs viewed at 52° angle, scale bar is 2 μm. Red insets show zoomed portion of micrographs, scale bar is 2 μm. (c,d) Normalized far field diffraction patterns taken at 200 keV and 300 keV respectively. (e,f) Bar plots of the measured relative diffraction efficiencies.

efficiency blazed hologram was made with FIB milling and had a relative diffraction efficiency of $\eta_1^{(r)} = 40\%$, but required a 2 μm pitch [65]. This is a greater than 50% increase in diffraction efficiency, but with a significant decrease in pitch and increase in hologram diameter. Consequently, FIB GAE-fabricated holograms produce high beam current, isolated electron vortex beams ideal for electron vortex probe experiments.

Recent demonstrations of electron interferometry using nanoscale gratings show promise for significantly improving the phase sensitivity of scanning transmission electron microscopy [66], but are limited by the devices used to coherently divide the electron beam. A hologram used as an amplitude-dividing electron beamsplitter must maximize diffraction into two diffraction orders separated by a large angular separation. The undiffracted ($m = 0$) order can be completely suppressed by controlling the mill depth of a binary hologram so that the phase difference between

peaks and troughs of the square wave of the transmitted wave is π [49]. FIB GAE allows for this condition to be met at a smaller pitch, and larger aperture than conventional FIB milling (Fig. 2.5(b)). When used as an amplitude-dividing beam splitter, the path separation between diffraction orders is inversely proportional to pitch, and suppressing the $m = 0$ diffraction order doubles the path separation of the two most intense diffraction orders.

We have made holograms up to 60 μm diameters with comparable efficiencies to those in Figure 2.5. Combining current of the ion beam with the dose used in each test mill and the linearity of mill depth in time as shown in Figure 2.3, gives an average mill time per mill depth per mill area of 0.008 $\text{s}\cdot\text{nm}^{-1} \cdot \mu\text{m}^{-2}$ for binary gratings. At 80 keV, 21 nm of S_3N_4 gives a π phase shift to the electron wave; if we wanted to reach this depth for a binary grating with a 80 μm diameter it would take 1.5 hours. This is a reasonable estimated limit for making holograms with $\sim$200 nm feature sizes with the parameters used. This could be improved by increasing the ion beam current at a cost of resolution.

We used 100 nm thick Si_3N_4 membranes of the gratings because of the large mill depths required at higher energies. It should be noted that FIB GAE is scalable with minimal membrane stretch when the mill depth is at most 2/3 the thickness of the membrane. This makes it possible to have ideal binary holograms in 30 nm thick membranes for energies below 80 keV.

2.2.2. Incoherent Scattering from Holograms

A primary concern about material phase gratings for electrons is the decoherence effects of scattering within the materials. Current research in programmable phase plates based on the interaction of free electrons with static electromagnetic fields

shows promise, but are still a long way from matching the resolution and versatility of static material phase plates [67, 68].

The angular distributions of all the scattering processes that occur within the material of the holograms have non-zero contributions at the angles of the usable diffraction orders from the holograms. Inelastically scattered electrons from the material that remain in the solid angle subtended by the diffracted electrons cause a loss in coherence [69]. However, note that the electrons coherently diffracted by the hologram have well-defined transverse momentum whereas the electrons scattered in the hologram delocalize in the far field according to their angular distributions. If the coherently diffracted electrons are used as interaction probes in the far field of the hologram, the loss of coherence should be partially mitigated by essentially filtering by transverse momenta. A qualitative example of this delocalization is shown for the bulk plasmon of Si_3N_4 using electron energy loss spectroscopy in the Figure 2.6 and generalizes to any angularly distributing scattering process within the material. FIB GAE further mitigates these decoherence effects by allowing for the use of large holograms with ideal groove profiles in thinner Si_3N_4 membranes, as well as decreasing gallium implanted in the hologram by decreasing the needed time under the ion beam.

2.3. Chapter Summary

We have demonstrated FIB GAE as a scalable method for fabricating electron holograms that is robust for generating any arbitrary groove profile for electron diffraction gratings. This nanofabrication method is not only capable of making high efficiency blazed holograms for electrons, but is much easier to implement than pure FIB milling and lithographic techniques, as well as having immediate applications

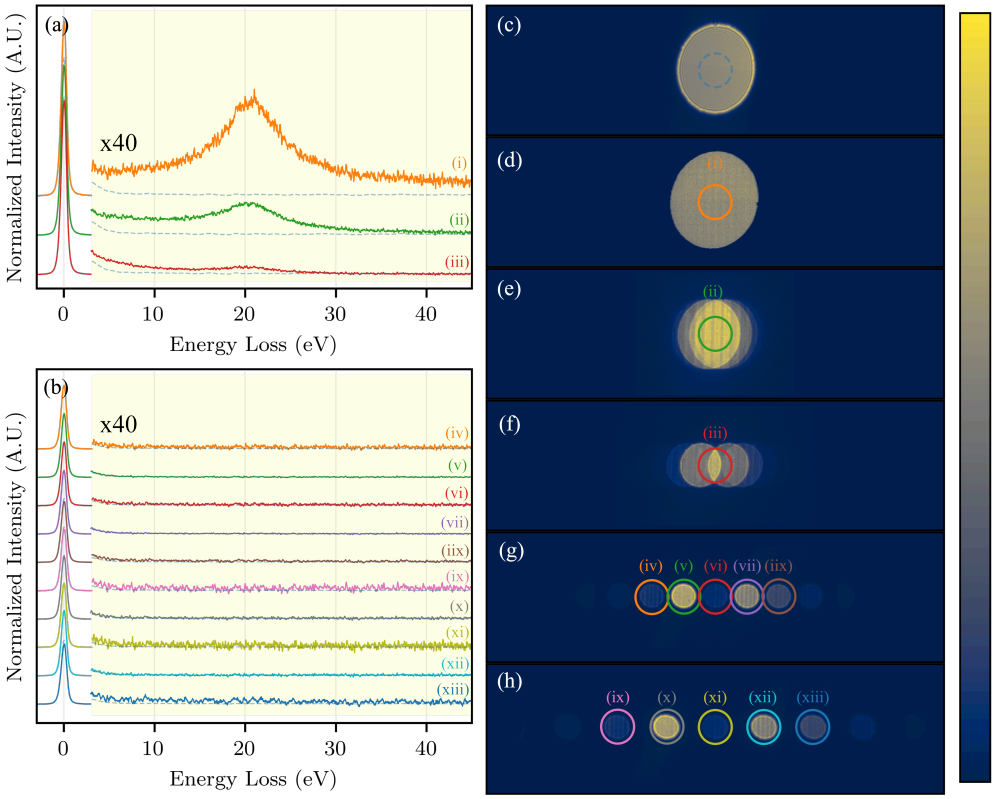

FIGURE 2.6. (a,b) Electron energy loss spectra (EELS) at different focal planes, magnifications, and spectrometer entrance aperture positions of electrons that have passed through a 200 nm pitch binary hologram showing that the diffracted beams do not have an appreciable energy spread. All spectra are normalized to the total counts. (c-d) Images of electron intensity distribution without the hologram (c), used for comparison, and for different defocused planes after the hologram (d-h) with the position and scale of the EELS entrance aperture. (a) The different colored EELS spectra correspond to the same colored apertures and positions shown in (c-f). The Si_3N_4 bulk plasmon around 20 eV decreases in intensity with respect to the zero loss peak as the electrons are allowed to propagate to the far field. Near the focal plane, the electrons coherently diffracted by the hologram have a well-defined transverse momentum separating into their individual diffraction orders, while electrons inelastically scattered by hologram delocalize and cannot be resolved above the noise of the detector (b,g,h). The Roman numerals next each aperture match the corresponding EELS spectrum.

in structured probe spectroscopy and interferometric phase contrast microscopy. Although we have only highlighted two specific examples for the application of FIB GAE made holograms in electron optics, it also can be just as impactful making

holograms to correct aberrations that are inherent to magnetic lenses, as well as holograms that can impart arbitrary spatial amplitudes and phases to electron wavefronts [40, 41], as discussed in the next chapter. Aside from its applications in electron optics, this technique could prove useful in creating holograms for coherent X-ray, EUV, and neutron optics [35, 70].

CHAPTER III

HOLOGRAPHICALLY STRUCTURING ELECTRON WAVEFRONTS

Aside from optimizing the off-axis diffraction efficiency of a grating, the nanofabricated holograms described in the previous chapter can also be used to coherently structure the transverse wavefront of an electron beam.

Notes for Ch. III:

This chapter is adapted from the published research article:

[71] **C. W. Johnson***, J. S. Pierce*, R. C. Moraski, A. E. Turner, A. T. Greenberg, W. S. Parker, and B. J. McMorran. Exact Design of Complex Amplitude Holograms for Producing Arbitrary Scalar Fields. *Optics Express*, 28(12):17334-17346, 2020.

*JSP and I were co-authors with equal contributions. JSP developed the theory and reconstruction code for this project. BJM and I developed the experimental tests for the paper. I wrote ∼70% the paper with ∼30% of the text written in previous drafts by JSP. I performed all the experiments. RCM, AET, ATG, and WSP all either contributed to one or more of writing analysis code, interpreting experiment results, or providing paper edits.

Transverse shaping of paraxial optical beams via holography has been a mature subject for decades [33]. Research in this field remains active due to the vast utility and applications of structured optical wavefronts [72]. The physical principles allowing for transverse optical beam shaping are general for any scalar field that is well described by Fourier optics, i.e., the wavefunctions describing electron matter-waves [73] or any other quantum matter-wave [74, 75, 76]. Recent advances

in theoretical treatments and experimental implementations over the control of transverse optical fields have mainly focused on specific technologies, such as spatial light modulators (SLMs), that can be programmed to independently control either the transverse amplitude or phase [77, 78, 79, 80].

Within the past decade, research in shaping the transverse wavefunction of coherent electron beams in transmission electron microscopes (TEM) has been expanding with the possibility to replicate the successes transverse beam shaping have provided light optics. The high spatial resolution possible in a TEM has allowed structured electrons to match the symmetry of individual nanoplasmonic excitations to distinguish between modes [23]. Prospects for using structured electrons to probe individual atomic systems seem achievable [81]. The spin, charge, and mass of a free electron differ from that of a photon resulting in rich physics due to spin-orbit coupling, magnetic field interactions, and relativistic effects that have not been fully experimentally realized [82, 83, 84]. Progress in these fields could be advanced with more precise transverse beam shaping.

Programmable diffractive optics for electrons are in development [67, 68], but the most predominant way to shape the transverse electron wavefront has been by material phase plates [49, 50, 51], much like the passive diffractive optics used in coherent X-ray optics [70, 85]. These material phase plates have a phase shift and amplitude attenuation per unit thickness of the material. Accordingly, the hologram designs for SLMs that assume only a pure phase shift or pure amplitude loss cannot be used for electron holograms to exactly produce the correct desired amplitude and phase [86]. A new method for hologram pattern generation is required that can simultaneously consider phase shift and amplitude loss through the hologram and still produce the intended target wavefunction.

In this chapter, we introduce such a method to design off-axis holograms that exactly encodes any arbitrary phase and amplitude profile on a specific diffraction order of a scalar field. These holograms can be expressed as an envelope function over a periodic function, defined by its (position dependent) Fourier expansion. The method is general for phase-only, amplitude-only, or mixed phase and amplitude holograms in the thin-hologram limit.

3.1. Model and theory

3.1.1. Thin transmission holograms

Under the thin hologram approximation, a paraxial scalar wave transmitting through a thin material with a complex transmission function will acquire both a phase shift and amplitude loss. Thus, the phase shift and amplitude loss of the transmitted wave through a material hologram are dependent on material parameters and the longitudinal thickness

$$\psi(\mathbf{R}) = \psi_0(\mathbf{R}) \exp\left(i \int_0^{t(\mathbf{R})} dz\, \widetilde{\Phi} \right), \tag{3.1}$$

where $\psi(\mathbf{R})$ and $\psi_0(\mathbf{R})$ are the transmitted and incident waves immediately after and before the hologram, $t(\mathbf{R})$ is the longitudinal thickness profile of the hologram, with transverse coordinates $\mathbf{R} = (x, y)$, and $\widetilde{\Phi} = \Phi_0 + i\alpha$ gives the longitudinal phase shift and amplitude attenuation per unit length through the material. We assume plane wave illumination as well as a homogeneous and amorphous hologram material with $\frac{d}{dz}\widetilde{\Phi} = 0$, allowing us to set $\psi_0(\mathbf{R}) = \psi_0$. Carrying out the integration gives

$$\psi(\mathbf{R}) = \psi_0 \exp\left(i\widetilde{\Phi} t(\mathbf{R})\right). \tag{3.2}$$

Generally with these assumptions, the wavefront transmitted through an off-axis hologram can be written as a sum of diffraction orders

$$\psi(\mathbf{R}) = \sum_{m=-\infty}^{\infty} \psi_m(\mathbf{R}) e^{im\mathbf{K}_0\cdot\mathbf{R}}. \tag{3.3}$$

The m^{th} diffraction order carries $m\hbar|\mathbf{K}_0|$ transverse momentum and is spatially separated from the other orders in the far field. By far field we mean at the back focal plane of a lens which is equivalent to forward wave propagation to $z \to \infty$ with scaled transverse coordinates $\mathbf{K} = (k_x, k_y)$. The spatial positions, $\mathbf{K}$, in this back focal plane correspond to the transverse momentum distribution of the wave, see Figure 3.1.

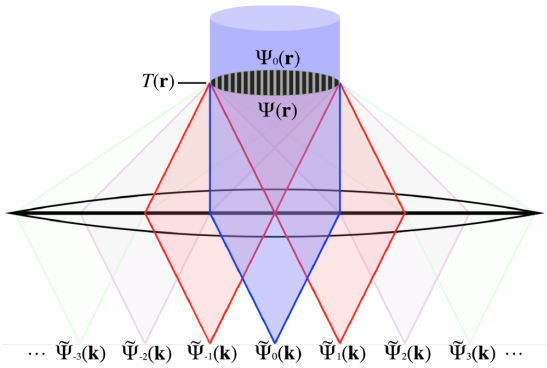

FIGURE 3.1. Illustration of a wavefunction $\psi_0(\mathbf{R})$ incident on an off-axis hologram with groove profile $t(\mathbf{R})$. The wavefunction after the hologram $\psi(\mathbf{R})$ propagates into spatially separated diffraction orders in the back focal plane/far field, $\sum_m \tilde{\psi}_m(\mathbf{K})$.

The goal is to produce a desired wavefunction in the far field when the diffraction orders are spatially separated, but since $\psi_m(\mathbf{R})$ and $\tilde{\psi}_m(\mathbf{K})$ are uniquely related via Fourier transformation it is sufficient to reconstruct the near field $\psi_m(\mathbf{R}) = \int d\mathbf{K}\, \tilde{\psi}_m(\mathbf{K}) e^{i\mathbf{K}\cdot\mathbf{R}}$. Consequently, we expand each transmitted wave diffraction order

as

$$\psi(\mathbf{R}) = \sum_{m=-\infty}^{\infty} A_m Z_m(\mathbf{R}) \Theta_m(\mathbf{R}) e^{im\mathbf{K}_0 \cdot \mathbf{R}} \equiv \sum_{m=-\infty}^{\infty} \Psi_m(\mathbf{R}) e^{im\mathbf{K}_0 \cdot \mathbf{R}}, \tag{3.4}$$

where $A_m > 0$ is a scalar amplitude, $0 \leq Z_m(\mathbf{R}) \leq 1$ is an envelope function, $\Theta_m(\mathbf{R})$ is a complex unit phase factor, and $\Psi_m(\mathbf{R})$ is the target wavefunction. The scalar amplitude, envelope function, and phase factor are uniquely determined by the target wavefunction to create in the far field in the m^{th} diffraction order. Now the hologram thickness profile $t(\mathbf{R})$ must be parameterized such that Equation (3.2) can be expanded as a sum of diffraction orders.

3.1.2. Constructing the hologram thickness profile

To construct the hologram thickness profile we first expand it into a Fourier series

$$t(\mathbf{R}) = t_0 - dZ(\mathbf{R}) \sum_{n=-\infty}^{\infty} c_n e^{in\mathbf{K}_0 \cdot \mathbf{R}}, \tag{3.5}$$

where $t_0 > 0$ is the hologram thickness, $0 < d < t_0$ is the max groove depth, $0 \leq Z(\mathbf{R}) \leq 1$ is an envelope function, $c_n = |c_n|\alpha_n$ are Fourier coefficients for the groove profile with α_n the unit phase factor, and $\mathbf{K}_0$ is the same transverse wavevector in Equation (3.3) that determines the hologram grating pitch and direction. However, the groove depth modulation of this linear grating, provided by $Z(\mathbf{R})$, is not enough to arbitrarily sculpt the diffracted wavefronts. To allow for sculpting of the transmitted wavefront we let c_n and $\mathbf{K}_0$ deviate from their nominal values over

the transverse plane

$$t(\mathbf{R}) = t_0 - dZ(\mathbf{R}) \sum_{n=-\infty}^{\infty} |c_n(\mathbf{R})| \alpha_n(\mathbf{R}) \left(\Theta(\mathbf{R}) e^{i\mathbf{K}_0 \cdot \mathbf{R}}\right)^n , \tag{3.6}$$

where we have defined $\Theta(\mathbf{R}) = e^{i\delta\mathbf{K}_0(\mathbf{R})\cdot\mathbf{R}}$ as the unit phase factor due to the local deviations from the constant pitch defining wavevector in the transverse plane $\mathbf{K}_0 \rightarrow \mathbf{K}_0 + \delta\mathbf{K}_0(\mathbf{R})$. It is important to allow for arbitrary groove profiles considering the choice of nanofabrication method and intended application of the hologram. In most cases we keep the Fourier coefficients constant, relying on $\Theta(\mathbf{R})$ to change the transmitted wavefront, but for binary groove profiles we allow the duty cycle of the grooves to vary in the transverse plane. Regardless, it can be shown that the thickness parameters $Z(\mathbf{R})$ and $\Theta(\mathbf{R})$ can be written as functions $Z_1(\mathbf{R})$ and $\Theta_1(\mathbf{R})$ which are determined by a target wavefunction to be generated in the first diffraction order for any groove profile defined by the Fourier coefficients $\{c_n\}$. As a result, we can write a single diffraction order as

$$\begin{aligned} A_m Z_m(\mathbf{R}) \Theta_m(\mathbf{R}) = e^{i\widetilde{\Phi}(t_0 - c_0(\mathbf{R}) dZ(\mathbf{R}))} \Theta(\mathbf{R})^m \\ \times \sum_{s \in E_m} \prod_{n=1}^{\infty} \alpha_n(\mathbf{R})^{s(n)} I_{s(n)}\big(-2i\widetilde{\Phi}|c_n(\mathbf{R})| dZ(\mathbf{R})\big), \end{aligned} \tag{3.7}$$

where $s(n) \in E_m$ is a set of all maps that provide an $e^{im\mathbf{K}_0\cdot\mathbf{R}}$ factor and $I_m(x)$ is a modified Bessel function of the first kind. This result is found by algebraic manipulation while rewriting an infinite product of infinite sum as an infinite sum of infinite products and an explicit derivation is shown in Appendix A.

3.2. Holograms with specific groove profiles

This theory applies to any material hologram, though here we apply it to electron wavefront manipulation in a TEM. For electron off-axis holograms patterned on a TEM thin silicon nitride (Si_3N_4) window, the typical groove pitch is between 100 nm and 200 nm. Standard beam energies between 60 keV and 300 keV correspond to electron wavelengths from approximately 5 pm to 2 pm, respectively. To produce a hologram groove profile we first need to use a specific value of $\widetilde{\Phi}$, i.e., choose an electron beam energy and material. We will assume an electron energy of 200 keV, giving $\widetilde{\Phi} \approx 0.008i - \pi/29$ nm^{-1} for a Si_3N_4 film [31].

We chose to design example holograms for producing two example target wavefunctions in the first diffraction order. The first target wavefunction is a balanced superposition of Laguerre-Gaussian modes with non-zero radial numbers:

$$\Psi^{(1)}(\mathbf{R}) = A_1 Z_1(\mathbf{R})\Theta_1(\mathbf{R}) \propto \mathrm{LG}_2^8(\mathbf{R}) + \mathrm{LG}_2^{-8}(\mathbf{R}), \tag{3.8}$$

where Laguerre-Gaussian modes are a class of solutions to Equation 1.4 with radial and azimuthal indices p, l for every mode $\mathrm{LG}_p^l(\mathbf{r})$. The second target wavefunction is a superposition of two Laguerre-Gaussian modes with differing azimuthal and radial numbers:

$$\Psi^{(2)}(\mathbf{R}) = A_1 Z_1(\mathbf{R})\Theta_1(\mathbf{R}) \propto \mathrm{LG}_3^5(\mathbf{R}) + \mathrm{LG}_1^{10}(\mathbf{R}). \tag{3.9}$$

All holograms have a groove pitch set to be 0.8 times the minimum Gaussian beam waist parameter of the of the Laguerre-Gaussian target wavefunctions. As an aside, any target wavefunction can be reproduced only being limited by the nanofabrication

resolution; complicated waveforms can require high precision in the large spatial frequencies of the periodic hologram profile. These example target wavefunctions were chosen because they have non-trivial complexity while still being experimentally practical as well as having the convenient property that the far field amplitude and phase is the same as near field, but just scaled and rotated in the transverse plane.

To exemplify the full versatility of this method, we demonstrate hologram groove patterns for both target wavefunctions that feature blazed, sinusoidal, and binary groove profiles, the latter two exhibiting convenient simplifications to Equation (3.7).

3.2.1. Blazed groove shapes

A blazed groove profile can be described by the Fourier coefficients

$$c_n = \begin{cases} \frac{1}{2} & \text{if } n = 0 \\ \\ \frac{i}{2\pi n} & \text{if } n \neq 0 \end{cases} . \tag{3.10}$$

We ran a brute force search for all the first order maps $s_(n) \in E_1$, i.e. all the maps that contribute to the first diffraction orders. We used 10,000 maps that had the largest contribution to the sum of products in Equation 3.7. Further details about this search can be found in Appendix A. The resulting hologram groove patterns are shown in Figure 3.2(a,d).

3.2.2. Sinusoidal groove shapes

The Fourier coefficients for a sinusoidal groove profile are given by $c_0 = \frac{1}{2}$ and $c_1 = c_{-1} = \frac{1}{4}$, with all other $c_n = 0$, giving a transmitted wavefunction of

$$\psi(\mathbf{R}) = e^{i\widetilde{\Phi}(t_0 - \frac{d}{2}Z(\mathbf{R}))} \sum_{m=-\infty}^{\infty} \left(\Theta(\mathbf{R})e^{i\mathbf{K}_0\cdot\mathbf{R}}\right)^m I_m\left(-\frac{id}{2}\widetilde{\Phi}Z(\mathbf{R})\right). \tag{3.11}$$

To reconstruct some function $Z_1(\mathbf{R})\Theta_1(\mathbf{R})$ in the first diffraction order, we must invert $Z(\mathbf{R})$ and $\Theta(\mathbf{R})$ in

$$A_1 Z_1(\mathbf{R})\Theta_1(\mathbf{R}) = e^{i\widetilde{\Phi}(t_0 - \frac{d}{2}Z(\mathbf{R}))}\Theta(\mathbf{R})I_1\left(-\frac{id}{2}\widetilde{\Phi}Z(\mathbf{R})\right). \tag{3.12}$$

The amplitude is then

$$A_1 = \left|e^{i\widetilde{\Phi}(t_0 - \frac{d}{2})}I_1\left(-\frac{id}{2}\widetilde{\Phi}\right)\right|. \tag{3.13}$$

With this amplitude, it is straightforward to numerically invert Equation (3.12) to find $Z(\mathbf{R})$ and $\Theta(\mathbf{R})$, see Figure 3.2(b,e).

3.2.3. Binary groove shapes

Binary groove profiles are given with the Fourier coefficients:

$$c_m(b(\mathbf{R})) = \begin{cases} b(\mathbf{R}) & \text{if } m = 0 \\ b(\mathbf{R})\,\mathrm{sinc}(m\pi b(\mathbf{R})) & \text{if } m \neq 0 \end{cases}. \tag{3.14}$$

Here $b(\mathbf{R})$ is a position dependent parameter giving the duty cycle, with $0 \leq b(\mathbf{R}) \leq 1$. Instead of following the procedure outlined previously, we note the transmitted

wavefunction has just two regions now where the hologram applies a constant phase and amplitude loss to each region, namely

$$\begin{aligned}\psi(\mathbf{R}) = e^{i\widetilde{\Phi}(t_0-d)} \sum_{m=-\infty}^{\infty} c_m(b(\mathbf{R})) \left(\Theta(\mathbf{R})e^{i\mathbf{K}_0\cdot\mathbf{R}}\right)^m \\ + e^{i\widetilde{\Phi}t_0}\left(1 - \sum_{m=-\infty}^{\infty} c_m(b(\mathbf{R})) \left(\Theta(\mathbf{R})e^{i\mathbf{K}_0\cdot\mathbf{R}}\right)^m\right).\end{aligned} \tag{3.15}$$

Combining these two convergent sums gives

$$\psi(\mathbf{R}) = e^{i\widetilde{\Phi}t_0} + \left(e^{i\widetilde{\Phi}(t_0-d)} - e^{i\widetilde{\Phi}t_0}\right) \sum_{m=-\infty}^{\infty} c_m(b(\mathbf{R})) \left(\Theta(\mathbf{R})e^{i\mathbf{K}_0\cdot\mathbf{R}}\right)^m. \tag{3.16}$$

A single non-zero diffraction order is then

$$A_m\Theta_m(\mathbf{R})Z_m(\mathbf{R}) = \left(e^{i\widetilde{\Phi}(t_0-d)} - e^{i\widetilde{\Phi}t_0}\right) \frac{\sin(m\pi b(\mathbf{R}))}{m\pi}\Theta(\mathbf{R})^m. \tag{3.17}$$

We do not present a proof that Equation (3.17) is equivalent to Equation (3.7), but have verified that this does indeed produce the same hologram groove profile.

To reconstruct some function $Z_1(\mathbf{R})\Theta_1(\mathbf{R})$ in the first diffraction order we must find the appropriate amplitude A_1 that satisfies Equation (3.17). The magnitude of $\Psi_1(\mathbf{R})$ is maximized when $b(\mathbf{R}) = 1/2$, meaning we must set $A_1 = |e^{i\widetilde{\Phi}(t_0-d)} - e^{i\widetilde{\Phi}t_0}|/\pi$. With this, the functions $b(\mathbf{R})$ and $\Theta(\mathbf{R})$ are given by

$$b(\mathbf{R}) = \frac{1}{\pi}\arcsin\left(Z_1(\mathbf{R})\right) \tag{3.18}$$

and

$$\Theta(\mathbf{R}) = \Theta_1(\mathbf{R})e^{-i\arg[e^{i\widetilde{\Phi}(t_0-d)} - e^{i\widetilde{\Phi}t_0}]}. \tag{3.19}$$

This is the same result as in [80], but is not limited to amplitude only holograms. The resulting holograms for the target wavefunctions can be seen in Figure 3.2(c,f).

Notice that, for Equation (3.19), the ultimate groove depth d only changes the global phase and scalar amplitude of the diffracted beam and does not affect its spatial structure. From a design perspective this is desirable since fabricating groove arrays to an exact depth can be quite difficult. More importantly, the hologram groove profile does not change as a function of material parameter $\widetilde{\Phi}$, the only energy-dependent parameter. In other words one hologram can provide consistent correction for a range of wavelengths, albeit with different amplitudes.

Another benefit of binary holograms is that if the $+1$ diffraction order gives an exact beam (say a perfect LG_1^0 beam, which is a vortex beam [52]), then the -1 diffraction order will be a perfect beam of the opposite phase (giving an LG_{-1}^0). This is not the case for the other hologram groove types because they produce asymmetric

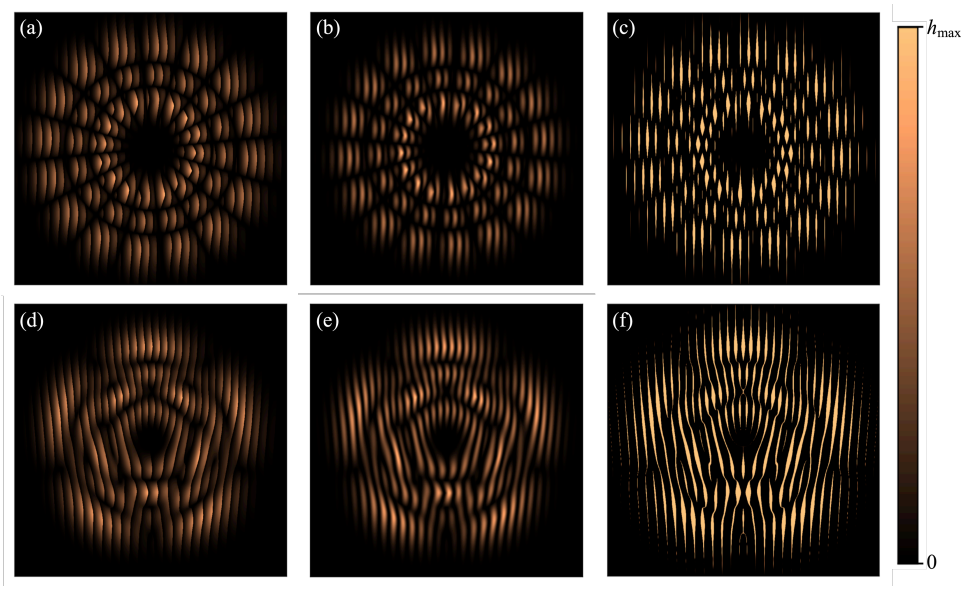

FIGURE 3.2. (a-c) Blazed, sinusoidal, and binary hologram groove profiles for $\Psi^{(1)}(\mathbf{R})$, respectively. (d-f) Blazed, sinusoidal, and binary hologram groove profiles for $\Psi^{(2)}(\mathbf{R})$, respectively.

groove patterns and only provide the correct target wavefunction in a single diffraction order.

3.2.4. Choosing a groove profile

The groove profile of the hologram ultimately affects the diffraction efficiencies which are highly dependent on the ratio of phase shift and amplitude attenuation per unit length of the hologram material. The nanofabrication method used to make the hologram is also a factor, as some methods are more adept at creating a given groove profile than others. Typically, blazed profiles maximize the intensity in a single given diffraction order and have mostly been made by focused ion beam (FIB) milling, where as binary profiles maximize an equal amount of intensity into equal but opposite diffraction orders and have mostly been made by electron beam lithography. When the FIB beam size is comparable to the feature size of the hologram, the resulting grooves can be sinusoidal. The nanofabrication method's resolution limit and the feature sizes of the hologram must be considered on a case by case basis depending on the required precision of the hologram output for the intended application.

3.3. Experiment

The hologram design principles outlined above apply to any paraxial beam, e.g. photons or matter waves. We demonstrate the effectiveness of this procedure by producing nanoscale holograms for manipulating coherent electron beams in a transmission electron microscope (TEM).

3.3.1. Hologram nanofabrication

Groove profiles of the two target wavefunctions, $\Psi^{(1)}(\mathbf{R})$ and $\Psi^{(2)}(\mathbf{R})$, similar to those in Figure 3.2, were used to create raster pattern stream files for an FEI Helios Dual Beam 600i Ga^+ FIB [87]. The profiles were milled into a single 100 nm thick Si_3N_4 membrane which was coated on the bottom with a $\sim$5 nm thick titanium/platinum layer to alleviate charge. An etchant gas, XeF_2, was used to assist in the milling process and improve the spatial groove depth controllability [31]. All six groove profiles were repeatedly milled with varying mill time to ensure that the correct groove depth was achieved for the blazed and sinusoidal hologram, as only the correct groove depth produces the desired wavefunction.

3.3.2. Measurement and phase reconstruction of target wavefunctions

The array of holograms was placed in the specimen plane of an FEI Titan transmission electron microscope (TEM) operated at 200 keV, see Figure 1.3. The incident beam was spread out to be much larger than the outer hologram diameter to ensure close to plane wave illumination. The magnetic lenses after the specimen plane were used to place a magnified image of the hologram's back focal plane at a CCD camera at the bottom of the TEM column. For each hologram, a focal series of transverse plane intensity images were recorded at equally spaced z positions through the back focal plane of a lens.

These images of the focal series were smoothed with a Gaussian convolution kernel. A small amount of stigmatic aberration from small misalignments in the TEM were removed digitally with affine scale transformations linear with the defocus applied to each image. The images were then digitally aligned by their intensity center of mass. We used a Fourier transform-based iterative transport of intensity

equation algorithm to reconstruct the phase of the electron wave in the back focal plane of each hologram with a flat initial phase input guess to seed the iterative reconstruction. This phase reconstruction method has been shown to be robust for reconstructing the phase of a wave in the presence of phase singularities [88].

3.3.3. Discussion of experimental results

The desired and measured far field complex amplitude (the square root of measured intensity multiplied by the reconstructed phase factor for each target function) of $\widetilde{\Psi}^{(1)}(\mathbf{K})$ and $\widetilde{\Psi}^{(2)}(\mathbf{K})$, as well as the binary, sinusoidal, and blazed holograms can be seen in Figure 3.3. Notice in Figure 3.3(f) the hologram was

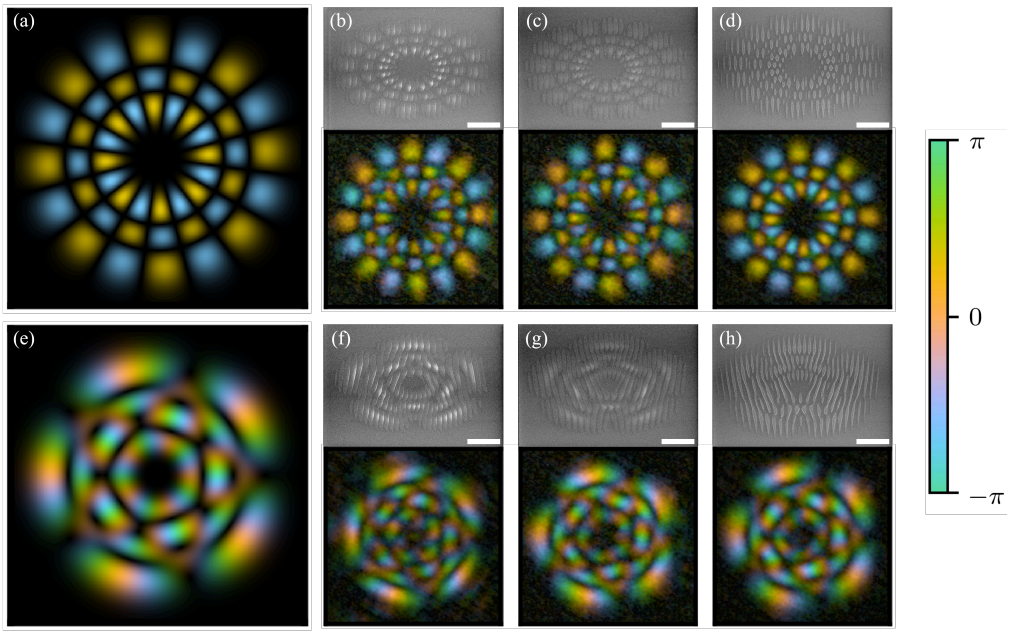

FIGURE 3.3. (a,e) Desired complex amplitudes (color is phase and brightness is amplitude) for $\widetilde{\Psi}^{(1)}(\mathbf{K})$ and $\widetilde{\Psi}^{(2)}(\mathbf{K})$ in the far field, respectively. Experimental hologram SEM micrographs and TEM back focal plane complex amplitudes for (b-d) $\widetilde{\Psi}^{(1)}(\mathbf{K})$ and (f-h) $\widetilde{\Psi}^{(2)}(\mathbf{K})$ with blazed, sinusoidal, and binary groove profiles each with maximum mill depths of $d_{\max} = 61.5$ nm, 36.2 nm, and 29.0 nm, respectively. All scale bars in the micrographs are 2 μm.

made for conjugated target wavefunction $\Psi^{(2)}(\mathbf{R})^*$ which is reflected in the reconstructed phase. Also, in Figure 3.3(b-d) there is a noticeable additional phase to the expected phase from Figure 3.3(a). This additional phase curvature is in the direction of the scaling from the affine transformations used on the focal series and is considered to be part of the error from the reconstruction. We also note that the reconstruction appears to be closer to the intended target wavefunction with higher contrast going from the blazed to binary profiles. Numerical simulations with the intended groove profiles produce the exact target wavefunctions, so we attribute this deviation from the expected result to inaccurately milled profiles and for the case of blazed and sinusoidal grooves, not reaching the exact maximum mill depth $d_{\max}$. The finite width of the FIB beam size does a poor job at properly defining the sharp cusps of the blazed profile, so it is reasonable that the sinusoidal profile produces a more accurate wavefront. As noted in Section 3.2.3, the relative transverse structure of the of the reconstructed wavefront is not affected by mill depth for binary groove profiles and it should be expected that this groove profile most accurately produces the target wavefunction.

3.4. Chapter Summary

We have presented a new analytic method to generate groove patterns for off-axis holograms that takes complex transmission (modulation of both amplitude and phase) into account, and theoretically are able to exactly produce a desired target wavefunction in a chosen diffraction order. We demonstrated an experimental implementation of this method for two target wavefunctions, each with three different groove shapes milled into thin SiN membranes for electron waves. We have reconstructed the phase from focal series images of the back focal plane from the

experimental holograms and have shown that they are in good qualitative agreement with the expected amplitude and phase.

CHAPTER IV

A SCANNING TWO GRATING INTERFEROMETER IN A TEM

The holograms described in the previous two chapters can be used as efficient amplitude-dividing beam splitters for use in electron interferometry.

Notes for Ch. IV:

This chapter is adapted from the submitted research article:

[89] **C. W. Johnson***, A. E. Turner*, and B. J. McMorran. A Scanning two-Grating Free Electron Mach-Zehnder Interferometer. {Submitted}, arXiv:2104.09992 [physics.ins-det], April 2021.

*AET and I were co-authors with equal contributions. BJM, AET, and I developed the study for the paper. AET and I both contributed $\sim 50\%$ in performing experiments and writing the paper.

Electron holography and interferometry can enable nanoscale phase imaging [90, 91], the exploration of the Aharonov-Bohm effect [19, 92], interaction-free measurements and quantum electron microscopy [15, 93, 94], the measurement of coherence properties [20, 95**?**], quantum state tomography [17, 96], and the coherent control of the free electron wavefunction [97]. While interferometry is widely used in optics and photonics fields such as astronomy [98], optical metrology [99], neutral atom optics [100], and quantum optics [101], electron interferometry has advanced at a slower pace, partially due to a lack of basic optical elements such as beam splitters and mirrors that can be used to build a versatile system. Here we use two diffraction gratings as beam splitters in a conventional transmission electron microscope (TEM)

to create a flexible, path-separated Mach-Zehnder interferometer for free electrons, emulating the canonical example for phase sensitive interferometry.

Electron interferometers are currently limited and defined by the electron optical elements used to construct the interferometer. Electrostatic mirrors for free electrons show great promise, but are in their early development [67, 102, 103]. beam splitters have existed for decades, the most prevalent being electrostatic biprisms [104], which divide wavefronts and require high spatial coherence [105]. Biprisms generate interferograms from which the phase of the sample can be extracted after image processing. However, they require high spatial coherence; thus, they are inherently limited by modern electron emission sources that are only partially coherent. Using recently improved diffraction gratings as amplitude dividing beam splitters [16, 49, 106] to create spatially separated paths evades the high spatial coherence requirement, if the separated paths are recombined in the exact manner they were split after the sample [43]. We note that amplitude division with microwave chip beam splitters has also been demonstrated, but is not yet practical for electrons with kinetic energies above 200 eV [107].

Various demonstrations of matter wave interferometry have proceeded for decades [108]. Path-separated Mach-Zehnder interferometers specifically have been demonstrated for different kinds of matter waves, including neutrons [109], atoms [100], Bose-Einstein condensates [110], conduction and quantum Hall valley electrons in two-dimensional devices [111, 112], and superconducting quantum interference devices [113]. Free electron Mach-Zehnder interferometers with discrete separated outputs, i.e. dark and bright ports, have predominantly been constructed using nanofabricated diffraction gratings or crystals as beam splitters. Single crystal electron interferometers with two planes fabricated from monolithic uniform crystals

[114, 115] and three-crystal Mach-Zehnder interferometers with discrete adjustable crystal planes, [108, 116] have been demonstrated. A three-grating Mach-Zehnder interferometer for free electrons was demonstrated with nanofabricated transmission amplitude gratings [117]. Even though all of these interferometer variants for free electrons have advanced electron interferometry, none of them have the ability to scan well defined spatially separated paths over a specimen; i.e., they cannot be used for imaging. Furthermore, the short longitudinal length scales of these interferometers have restricted the type of experiments that can be performed.

Here we demonstrate a two-grating electron Mach-Zehnder interferometer (2GeMZI) inside a conventional TEM that provides clearly defined spatially separated probes that are the off-axis diffraction orders of the input grating focused in a back focal plane at the specimen section of the microscope, continuously tunable probe phase shifts, and scanning/imaging capabilities, i.e. the interferometer probes can be scanned across a phase shifting specimen changing the intensity of the interferometer output for each pixel in an imaging scan grid. Furthermore, since this is a scanning probe technique, the magnification can be changed at will by simply scanning over larger or smaller areas without adjusting the setup, unlike other comparable interferometric electron imaging technique. This is accomplished by placing diffraction gratings in apertures above and below the specimen plane of a TEM operated in scanning TEM (STEM) mode. The small deviations of the lens and aperture positions from the nominal STEM settings allow us to maintain the high resolution imaging capabilities afforded by the TEM while retaining the precise interferometer alignments. To demonstrate the phase sensitivity of the 2GeMZI we map electrostatic potential differences in the vicinity of both grounded and charged

silver nanorods and demonstrate quantitative nanoscale phase imaging of a spherical latex nanoparticle.

4.1. Interferometer Theoretical Description

In this electron interferometer, nanoscale diffraction gratings are used as amplitude-dividing beam splitters and the standard TEM imaging optics are used to separate, scan, and recombine the beams. An illustration of this system can be seen in Figure 4.1 where successive transverse planes are defined in relation to the previous plane by Fourier transform. Here we describe how the evolution of the electron wavefunction can be modeled throughout the interferometer and use the notation convention that input grating (G1) is in the **R** plane, the interferometer

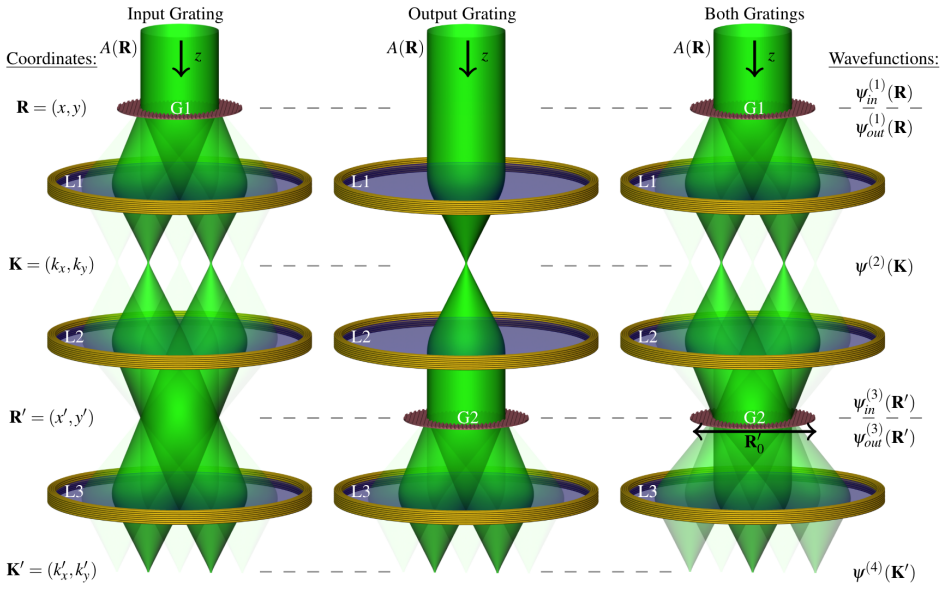

FIGURE 4.1. Diagram for 2GeMZI showing definitions of the different transverse planes as well as labels for the transverse wavefunctions in each plane, the magnetic lenses (L1, L2, L3), gratings (G1, G2), and beam-defining aperture $A(\mathbf{R})$ are also shown. The three different images depict the 3 cases of when the different gratings are inserted or removed. In the lower right corner we show the direction of the grating shift $\mathbf{R}'_0$ of the second grating.

probes are in the $\mathbf{K}$ or specimen plane, the output grating (G2) is in the $\mathbf{R}'$ plane, and the interferometer outputs are in the $\mathbf{K}'$ or detector plane.

The evolution of an electron wavefunction propagating through free space, neglecting spin, can be described by the time-independent Schrödinger equation with relativistic corrections (Section 1.2.1). In a typical TEM with a field emission electron source, electrons are accelerated to beam energies of 60 to 300 keV with a 500 meV energy spread and the electron beam has very small beam divergence [27]. The evolution of electron wavefunctions can therefore be modeled using Fresnel and Fourier optical theory [28], consistent with the Schrödinger equation with assumptions that the electrons are largely quasi-monochromatic, non-interacting, and collimated.

An electron wavefunction passing near or transmitting through an object can accumulate phase shifts and amplitude losses. In the weak phase approximation [118], these effects are proportional to the longitudinal extent of the interaction, e.g., the thickness of the material. This can be described by a complex index of refraction $\widetilde{\Phi} = \sigma U_{\text{mip}} + i\alpha$, where $\sigma = 2\pi me\lambda/h^2$ is the object independent interaction parameter for a free electron with relativistic mass m and de Broglie wavelength λ, U_{mip} is the mean inner potential of the material, and α is a material-dependent decay coefficient that models coherent amplitude loss due to high-angle scattering. We use this complex index of refraction model to describe both the diffraction holograms we employ as beam splitters and the specimens we image.

The transverse electron wavefunction incident on the input grating of the interferometer is assumed to be a plane wave with an outer edge defined by an aperture $\psi_{in}^{\{1\}}(\mathbf{R}) = A(\mathbf{R})$. When transmitted through a grating the wavefunction is

modified by its transmission function

$$\psi_{out}^{(1)}(\mathbf{R}) = A(\mathbf{R})e^{i\widetilde{\Phi}t_1(\mathbf{R})}, \tag{4.1}$$

where $t_1(\mathbf{R})$ is the periodic thickness profile of the grating. For a straight grating with pitch p_1 and diffraction wavevector $\mathbf{K}_1 = 2\pi/p_1$, we can expand Equation (4.1) by the Fourier series representation of the exponential term

$$\psi_{out}^{(1)}(\mathbf{R}) = A(\mathbf{R}) \sum_n c_n^{\{1\}} e^{in\mathbf{K}_1 \cdot \mathbf{R}}, \tag{4.2}$$

where the Fourier coefficients are given by

$$c_n^{\{1\}} = \frac{1}{p_1} \int_0^{p_1} d\tilde{x}\, e^{i\widetilde{\Phi}t_1(\tilde{x}) - in|\mathbf{K}_1|\tilde{x}} \tag{4.3}$$

where $\tilde{x}$ is in the direction of the grating pitch. Then the unnormalized probes in the back focal plane of the input grating can be expressed as

$$\psi^{(2)}(\mathbf{K}) \propto \sum_n c_n^{\{1\}} \widetilde{A}(\mathbf{K} - n\mathbf{K}_1), \tag{4.4}$$

where $\widetilde{A}(\mathbf{K})$ is the Fourier transform of $A(\mathbf{R})$. If the second grating is allowed to translate by an amount $\mathbf{R}'_0$, then the output of the second grating is

$$\psi_{out}^{(3)}(\mathbf{R}') \propto A(\mathbf{R}') \sum_{n,n'} c_n^{\{1\}*} c_{n'}^{\{2\}} e^{in'\mathbf{K}_2 \cdot (\mathbf{R}' - \mathbf{R}'_0) - in\mathbf{K}_1 \cdot \mathbf{R}'}, \tag{4.5}$$

where $c_n^{\{2\}}$ and $\mathbf{K}_2$ are similarly defined for the second grating. When the image of the input grating is projected onto the output grating with the same pitch and orientation, i.e., $\mathbf{K}_0 = \mathbf{K}_1 = \mathbf{K}_2$, the wavefunction in final $\mathbf{K}'$ plane can be written

as

$$\psi^{(4)}(\mathbf{K}') \propto \sum_{n,n'} c_n^{\{1\}*} c_{n'}^{\{2\}} e^{-in'\mathbf{K}_0\cdot\mathbf{R}_0'} \widetilde{A}(\mathbf{K}' - (n-n')\mathbf{K}_0). \tag{4.6}$$

The output of the interferometer is divided into distinct $m = n - n'$ diffraction orders. Using this to re-index the double sum, we can write Equation (4.6) as a sum of output diffraction orders

$$\begin{aligned} \psi^{(4)}(\mathbf{K}') &\propto \sum_m \left(\sum_n c_n^{\{1\}*} c_{n-m}^{\{2\}} e^{-i(n-m)\mathbf{K}_0\cdot\mathbf{R}_0'} \widetilde{A}(\mathbf{K}' - m\mathbf{K}_0) \right) \\ &= \sum_m \psi_m^{(4)}(\mathbf{K}'). \end{aligned} \tag{4.7}$$

When the gratings are symmetric and put a majority of the the transmitted intensity into the $m = \pm 1$ diffraction orders, i.e., $|c_{\pm 1}| \gg |c_{|n|\neq 1}|$ and $|c_{+1}| = |c_{-1}|$, then the $m = 0$ output diffraction order where $n = n'$, up to a global phase, is

$$\psi_0^{(4)}(\mathbf{K}') \propto |c_1^{\{1\}} c_1^{\{2\}}| \left(1 + e^{-2i\mathbf{K}_0\cdot\mathbf{R}_0'}\right) \widetilde{A}(\mathbf{K}') + \cdots . \tag{4.8}$$

We can consider the ability to scan the interferometer probes in the $\mathbf{K}$ plane by the vector $\mathbf{K}_s$, then the m^{th} probe is at the location $m\mathbf{K}_0 + \mathbf{K}_s$. We can also consider the probes passing through some electrostatic potential $V(\mathbf{K}, z)$, allowing us to apply the weak phase approximation and write the phase accumulated by each probe as being proportional to the projected potential along the z direction $\Phi(\mathbf{K}) = \sigma \int dz\, V(\mathbf{K}, z)$, see Figure 4.2. With this the 0^{th} order output of the interferometer is approximately

$$\psi_0^{(4)}(\mathbf{K}') \propto \left(1 + e^{i\varphi(\mathbf{K}_s, \mathbf{R}_0')}\right) \widetilde{A}(\mathbf{K}'), \tag{4.9}$$

where the total phase difference between the two highest intensity probes is

$$\phi(\mathbf{K}_s, \mathbf{R}'_0) = \ -2\mathbf{K}_0 \cdot \mathbf{R}'_0 + \Phi(\mathbf{K}_s - \mathbf{K}_0) - \Phi(\mathbf{K}_s + \mathbf{K}_0). \tag{4.10}$$

We should note that the static potential V can have contributions that extend into the vacuum region due to the build up of surface charge on a material as well as inside materials from the mean inner potential as was defined in $\widetilde{\Phi}$.

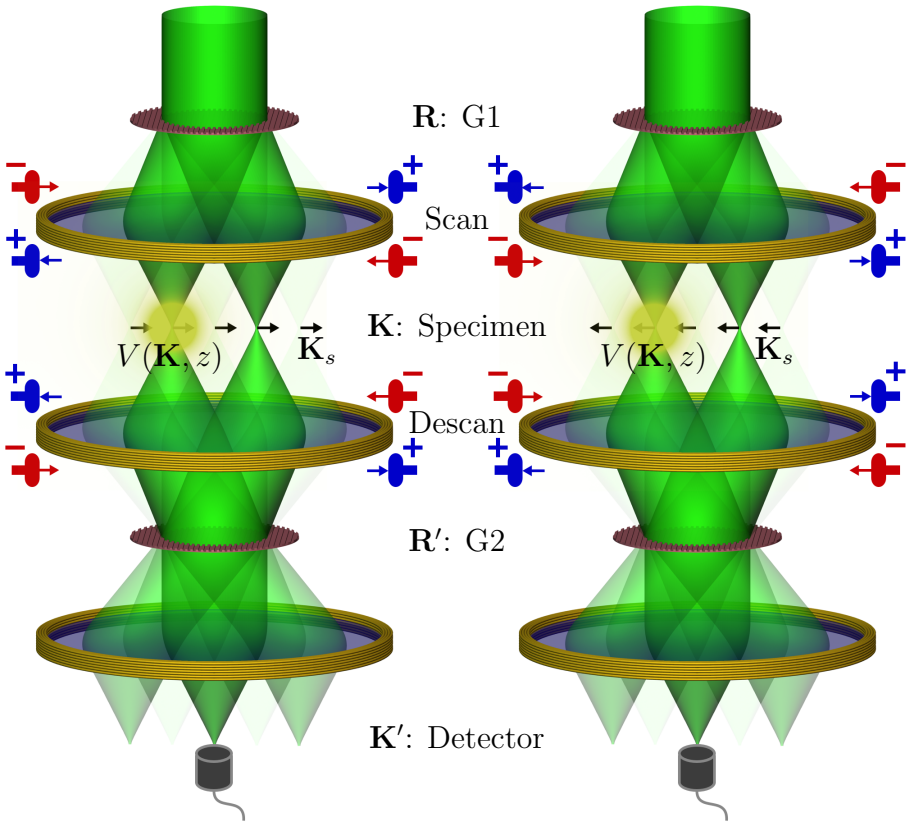

FIGURE 4.2. Illustration of how the microscope imaging scan/descan coils translate the interferometer probes by the vector $\mathbf{K}_s$ in the $\mathbf{K}$ plane while maintaining the interferometer alignment. Two scan directions shown, but is capable of scanning in two-dimensional transverse plane. Static potential $V(\mathbf{K}, z)$ is depicted by the semi-transparent yellow spot. A bright field (BF) monolithic detector can measure the intensity of the $m = 0$ interferometer output for every scan location to create an image.

4.2. Construction of Interferometer

Two arrays of 350 nm pitch, 30 μm diameter binary phase gratings were each nanofabricated onto a 250×250 μm^2, 30 nm thick, free-standing Si_3N_4 membrane using focused ion beam (FIB) gas-assisted etching described in Chapter 2 [31]. To aid with alignment, the gratings were patterned at multiple orientations in a 6×6 array. In an image-corrected 80-300 keV FEI Titan TEM, one grating array was installed in the second condenser aperture and used as the initial beam splitter (G1). The second grating array was installed in the post-specimen selected area aperture as the beam-combining beamspliter (G2). The TEM was operated at 80 keV in STEM mode with approximately a 1 mrad convergence angle. An independently positionable circular aperture at the third condenser lens was used to select the output of a single grating out of the widely illuminated array of gratings. The diffraction orders created by the selected input grating were focused to narrow probes at the specimen plane, Figure 4.2. The lenses were set in free lens control, so they could each be manually and independently controlled, and with the assistance of the "Lorentz" lens in the image corrector a correctly magnified, oriented, and in-focus image of G1 was projected onto G2. Finally, the post-G2 projection lenses were used to form images of the the far field diffraction pattern from the interferometer output on the detectors at the bottom of the TEM column. The relative grating shift parameter $\mathbf{R}_0'$, that is the relative transverse displacement between the input and output gratings, was controlled by the diffraction alignment coils in the image corrector that shifted the image of G1 relative to G2 allowing for arbitrary relative phase shifts between the two specimen plane probes in the interferometer output. The $\mathbf{K}$ plane probes at the specimen could be adjusted to have up to 1 μm separation between the ± 1 probes, although the spot size increases proportionally with the probe separation. Using

these beam splitter gratings, the ratio between separation between the paths, $2k_0$, and the width of the probes, δk, is fixed at about $2k_0/\delta k = 20$.

The magnitude of the $\{c_n^{\{1\}}\}$ and $\{c_n^{\{2\}}\}$ Fourier coefficients were measured by inserting only one of G1 or G2 at time while collecting an image of the probe intensities with a scintillator fiber-coupled CCD. A single diffraction order was integrated and divided by the total integrated intensity to determine normalized diffraction efficiencies $|c_n^{\{1\}}|^2$ and $|c_n^{\{2\}}|^2$; the measured grating outputs are shown in Figure 4.3(a,b). Ideally, the gratings would be perfect binary gratings with 50% groove duty cycle with up to 40.5% of the transmitted intensity going into each of the $m = \pm 1$ probes. However, edge rounding and non-ideal duty cycles from nanofabrication with a finite width ion beam as well as over and under milling from the ideal groove depth caused deviations from the optimal diffraction efficiency. Even so, we were able to achieve dominant $m = \pm 1$ coefficients allowing for efficient two

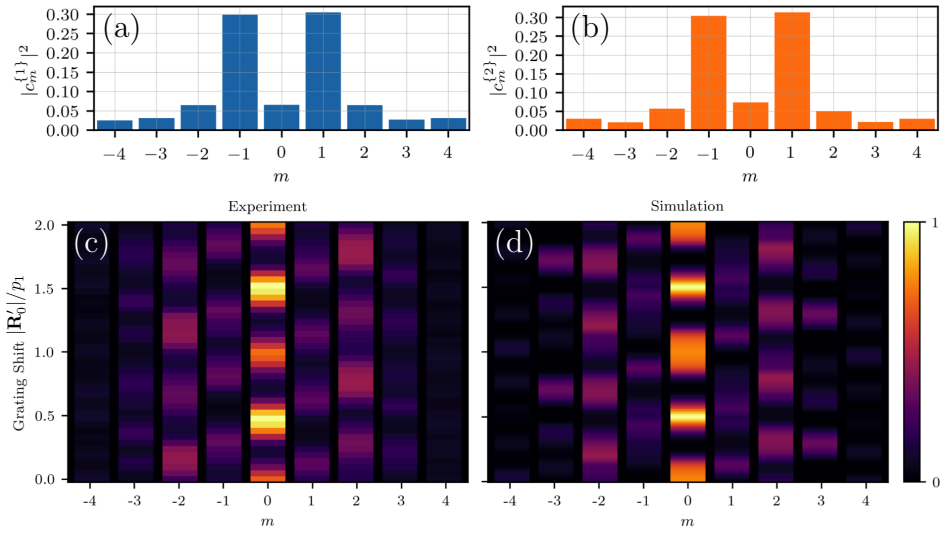

FIGURE 4.3. (a) G1 grating relative diffraction efficiency without G2 inserted. (b) G2 grating relative diffraction efficiency without G1 inserted. (c) Interferometer output order intensities as function of relative grating shift $\mathbf{R}_0'$ normalized by the grating pitch p_1. (d) Simulated interferometer output order intensities as function of relative grating shift $\mathbf{R}_0'$ normalized by the grating pitch p_1.

beam scanning in the 2GeMZI where each beam corresponds to either the +1 or -1 diffraction order.

With G1 and G2 both inserted, we collected CCD images of the output beams for different values of $\mathbf{R}_0'$ by tuning the previously mentioned diffraction alignment coils. The measured output intensities are in good agreement with the expected result, Figure 4.3(c,d). Without the presence of an electrostatic potential, the intensity of the 0^{th} order interferometer output is expected to be proportional to the modulus square of Equation (4.9), i.e., sinusoidal in the argument $\mathbf{K}_0 \cdot \mathbf{R}_0'$. We see this dependence in the experimental data, but it is also accompanied by a beating at half the spatial frequency $\mathbf{K}_0/2$. This frequency beating is caused by a combination of grating duty cycle mismatch and contributions of the higher-order terms from the sum of probe coefficients. Due to these higher-order effects, the fringe visibility $\mathcal{V} = (I_{max} - I_{min})/(I_{max} + I_{min}) = 0.76$ when the output is aligned for maximally destructive interference or $\mathcal{V} = 0.82$ when aligned for maximally constructive interference. The maximum theoretical fringe visibility $\mathcal{V} = 1$ can be approached through the continued improvement of gratings.

Scan and descan coils can be used to raster both beams across a scan region up to 3 times the probe separation while keeping the electron interference pattern (the image of G1) stationary on the second beam splitter (G2), ensuring the interferometer output was constant while beams were scanned across a flat phase region. The scan/descan system is independent of the diffraction alignment used to control $\mathbf{R}_0'$, so the relative phases between the interferometer probes remains constant throughout the scan. It should be noted that phase shifts due to path length differences during the scan certainly exist, but are small enough to neglect. While scanning, a bright field (BF) monolithic detector can be inserted such that it is illuminated by only the

0^{th} interferometer output order, Figure 4.2. This is a small, single pixel detector with a much faster acquisition rate than the microscope CCD camera that can record a single output order intensity value at every $\mathbf{K}_s$ scan position in a grid for a short dwell time on the order of microseconds creating interferometric BF images. In this configuration we can perform interferometric imaging with the 2GeMZI creating 512×512 pixel images on the order of hundreds of milliseconds. The relative phase between the probes at any scan position in the specimen plane $\mathbf{K}_s$ can be reconstructed from the intensity of the interferometer output

$$I_0^{(4)}(\mathbf{K}_s, \mathbf{R}'_0) = |\psi_0^{(4)}(\mathbf{K}_s, \mathbf{R}'_0)|^2 \approx \langle I_0^{(4)} \rangle_{\mathbf{K}_s} \left[1 + \mathcal{V} \cos\left(\varphi(\mathbf{K}_s, \mathbf{R}'_0)\right)\right], \tag{4.11}$$

where $\langle \cdots \rangle_{\mathbf{K}_s}$ is the average over all $\mathbf{K}_s$ scan positions.

4.3. Electrostatic Potentials in the Interferometer

One application of the 2GeMZI is mapping electrostatic potentials with out the need of image post-processing. In the last 30 years, quantitative potential maps measured with electron holography have been used to accurately determine charge distributions of nanoscale devices [119, 120]. However streamlined this method has become, it still requires image post-processing or proprietary live analysis software [121, 122]. While the high spatial and phase resolution of electron holography cannot yet be matched by the 2GeMZI in this initial demonstration, the interferometer provides a live interpretation of the electrostatic potential, whereas electron holography requires post-scan image processing. Each scanned image pixel values corresponds to the intensity of the interferometer output indicates the electrostatic potential difference at the two interferometer probes at scan locations

$\mathbf{K}_s \pm \mathbf{K}_0$. Here we use the 2GeMZI to show the fringes in raw interferometric BF images of a grounded and insulated vertical nanorod.

Using a Ga^+ FIB operated at 30 keV with a 7.7 pA beam current, we fabricated vertical silver nanorods on a nitride cantilever from a 100 nm thick silver film thermally deposited on a 50 nm thick Si_3N_4 membrane in the following steps:

(i) Mill completely through silver and nitride forming cylindrical silver bead along nitride tether.

(ii) Mill only through silver defining bottom edge of nanorod, optionally leaving a small lead of silver between the rod and the film.

(iii) Mill completely through silver and nitride defining top edge of rod and nitride cantilever.

(iv) Flip membrane over and raster FIB over the bare nitride section of cantilever to induce bending until the nanorod is vertical, normal to the silver film and nitride membrane [123].

These nanorods were fabricated with a clear vacuum region around the rods for easy access for imaging in the 2GeMZI. One of the two nanorods was given a small lead to ground to the rest of the silver film, while the other was electrically insulated by removing all of the silver between the nanorod and the film. An illustration of the fabrication process can be seen in Figure 4.4(a) accompanied by scanning electron microscopy (SEM) micrographs displaying the sample geometry and orientation, Figure 4.4(b-d).

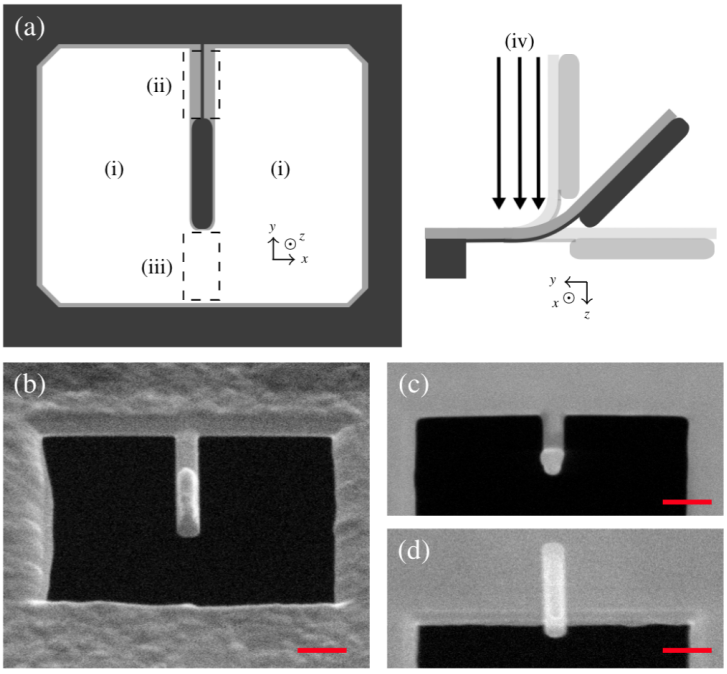

FIGURE 4.4. (a) Vertical silver nanorod FIB nanofabrication steps (i-iv). (b) SEM micrograph at 52° tilt after fabrication steps (i-iii). SEM micrographs after fabrication steps (i-iv) imaging from bottom of membrane at (c) 0° tilt and (d) 52° tilt. All scale bars are 200 nm.

The vertical nanorods were inserted in the specimen plane of the 2GeMZI which was adjusted to have a larger path separation of 500 nm with a probe size of about 25 nm. We recorded interferometric BF images over a scan region of 1.5x×1.5 μm^2 of the grounded and insulated nanorods shown in Figure 4.5(a,b). The electric potential from the semiconductor nitride substrate cantilever and the grounded nanorod was small; as shown in Figure 4.5(a), the interferometer output was only modulated close to the surface of the nitride and the relative phase between two probes in the vacuum region far away from the object is constant. However, the electrically insulated nanorod charged when exposed to the beam until reaching a static surface charge, creating a larger static potential. The resulting interference fringes for the probe potential differences can clearly be seen far into the surrounding vacuum region, as

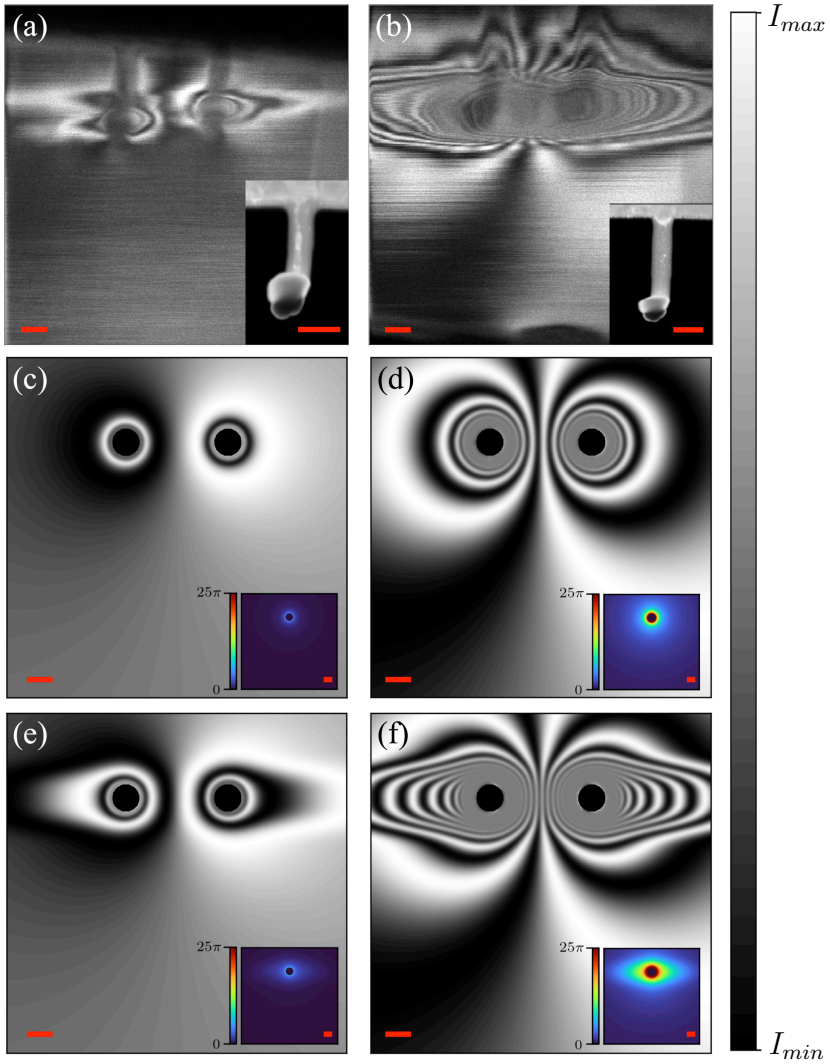

FIGURE 4.5. 2GeMZI BF images showing the $m = 1$ interferometer output intensity oscillating as a function of scan location between the intensity minimum and maximum for, (a) grounded vertical Ag nanorod, (b) insulated vertical Ag nanorod, insets are STEM high angle annular dark field images of each nanorod. (c,d) Simulated 2GeMZI output for two probes passing through a $1/r$ electrostatic potential where (d) has 10 times the charge of (c). (e,f) Same as (c,d) but with a horizontally elongated Gaussian included with the potential to simulate the increased induced charging. All scale bars are 100 nm.

shown in Figure 4.5(b). Close to the nanorod, the larger gradient in electrostatic potential induces a phase that varies within the width of the probes, resulting in a loss of fringe visibility.

We use $V(\mathbf{K}, z) = V_0/r$ as the electrostatic potential to approximate the nonlinear monotonically decreasing behavior that is expected surrounding a charged vertical nanorod, Figure 4.5(c,d). In the experimental interferometric BF images there is elongation in the probe separation direction that is not shown in this simple model, a plausible explanation for this is an increased surface charge on the nanorod when the higher-order probes ($m \neq \pm 1$) are incident. Including a Gaussian background to the potential giving the projected potential $V_z(\mathbf{K}, z) = V_0/r + V_1 e^{-k_x^2/2\delta k_x^2 - k_y^2/2\delta k_y^2}$ that is elongated in the probe separation direction, $\delta k_x = 5\delta k_y$. This extra potential is to account for the increase in surface charge when the interferometer probes are incident on the nanorods, Figure 4.5(e,f). The simulation values for V_0, V_1, and δk_y were chosen to give a qualitative fit for the interferometric images were experimentally measured in the 2GeMZI.

This initial demonstration shows that the 2GeMZI is qualitatively sensitive to differences in electrostatic potentials at the locations of the two probes: spatially varying electrostatic potentials impart a phase to the specimen probes and the phase difference modulates the intensity at the BF detector. With moderate improvements, the interferometric BF images can provide nanoscale that interpretable as maps of the static projected potential without need of image post-processing. Some challenges still need to be overcome to achieve quantitative potential mapping, especially for determining static charge distributions. First, one must ensure that the static charge is independent of the scanning probes which can be accomplished with adequately grounded, conductive materials. Second, one must limit the samples of interest

such that the spatial extent of the potential does not significantly extend over multiple probe locations in the **K** plane. This ensures there is a reference probe and a measurement probe with a phase difference that is directly proportional to the potential. This second point can be relaxed2 with a careful analysis and full understanding of the accumulated relative phases between all the probes as they are scanned through the potential. Third, smaller probe sizes must be used to probe potentials with small spatial features or large spatial gradients.

4.4. Quantitative Phase Imaging of a Latex Nanoparticle

To demonstrate an example of quantitative phase imaging with the 2GeMZI, we imaged polystyrene latex spherical nanoparticles (NP) on a suspended single layer of graphene. Polystyrene latex has a well-characterized mean inner potential, $U_{\text{mip}}^{\text{latex}} = 8.5 \pm 0.7$ V [124]. We use a nanosphere with a diameter of 60 nm. The ratio of probe size and separation is fixed, but can be simultaneously tuned by changing the lens magnification settings. Here the 2GeMZI was tuned for a probe separation of 92 ± 2 nm and a focused beam width of approximately 5 nm such that one of the two 2GeMZI probes could be scanned through the nanosphere while the other passed through uniform graphene in the specimen plane; same as in Figure 4.2, but with a NP instead of a static potential. The phase imparted by the graphene is expected to be about 45 mrad [125]. Individual atoms are not resolvable at the resolution in this initial demonstration, so we treat the sample as a homogeneous latex sphere with a small uniform phase background. Another benefit of the graphene substrate is that it efficiently alleviates charge, allowing us to disregard extraneous static fields due to sample charging and only consider the mean inner potential from the latex as the source of the probe phase shift. Due to the size of the NP in comparison to

the large probe separation, the elimination of electrostatic fields, and the negligible decay coefficient of latex, we can assume the phase difference between the two probes is

$$\varphi(\mathbf{K}_s, \mathbf{R}_0') = -2\mathbf{K}_0 \cdot \mathbf{R}_0' + \sigma U_{\text{mip}}^{\text{latex}} t_{\text{sph}}(\mathbf{K}_s). \tag{4.12}$$

The first term, $2\mathbf{K}_0 \cdot \mathbf{R}_0'$, is due to the interferometer alignment and the last, $\sigma U_{\text{mip}}^{\text{latex}} t_{\text{sph}}(\mathbf{K}_s)$, is the phase accumulated by the probe passing through the sphere of projected thickness $t_{\text{sph}}(\mathbf{K}_s)$ at the scan location $\mathbf{K}_s$. The latex spheres were interferometrically imaged by scanning the probes over a 100×100 nm^2 scan region while the $m = 0$ interferometer output order was recorded by the BF detector, same as in Figure 4.2, but with spherical NP instead of a vacuum static potential.

We recovered the phase image of the 60 nm diameter latex NP from two interferometric BF images, one with the interferometer initially aligned for maximally constructive 0^{th} order output, $2\mathbf{K}_0 \cdot \mathbf{R}_0' = \pi$, Figure 4.6(ii), and one aligned for a destructive output $2\mathbf{K}_0 \cdot \mathbf{R}_0' = 0$, Figure 4.6(iii). To map each pixel's intensity from an image scan onto a phase, we first find the center of the NP and take an azimuthal average of the intensity to exploit the particle symmetry. This provides an average intensity line profile across the NP and graphene from the constructive and destructive interferometric images, Figure 4.6(iv). Exploiting the phase continuity of the spherical NP, we note that the phase should be monotonically increasing from the graphene substrate to the center of the NP. We set the phase of the graphene substrate to zero, as a reference. Using the co-sinusoidal relation between phase and intensity found in Equation (4.11), we map the intensity profile to a phase profile.

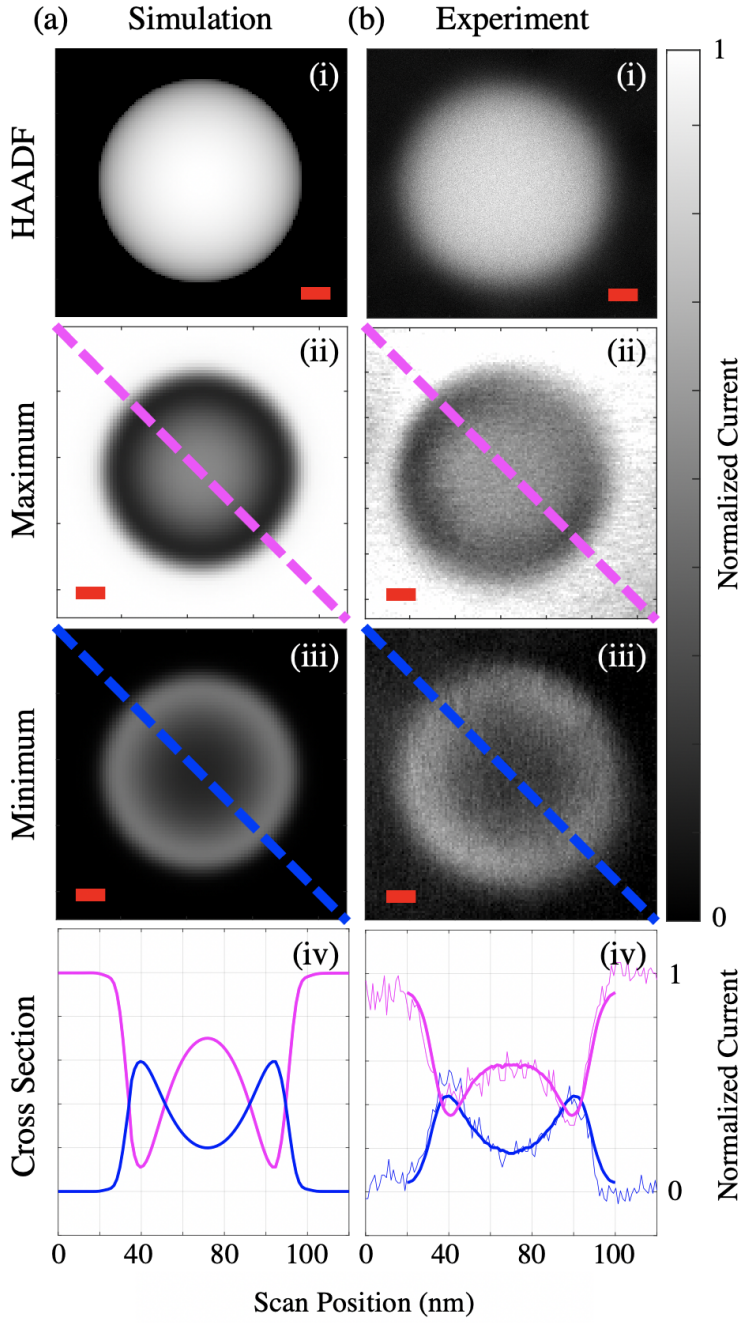

FIGURE 4.6. High angle annular dark field (HAADF) and 2GeMZI BF image scans of a latex NP both from (a) simulation and (b) experiment. The rows display (i) the HAADF image, the 2GeMZI image aligned at the maximally (ii) constructive (magenta) and (iii) destructive (blue) interferometer output, and (iv) the respective line profiles. The experimental cross section (b(iv)) shows a raw cross section (light line) and the radially averaged signal (weighted line). All scalebars are 10 nm.

From these radial phase profiles, we reconstruct a phase image of the particle, as shown in Figure 4.7.

Using the experimental Fourier coefficients which define each grating, a 5 nm spot size, 100 nm probe separation and assuming the NP is a perfectly spherical phase object, we simulate the expected intensity output in the BF detector when the positive first order probe interacts with the sample for both alignment schemes, Figure 4.6(a). The simulated intensity profile is then mapped to phase using the same mechanism as described above. The phase profiles reconstructed from the experimental interferometric images of the latex NPs can be up to 10% lower than

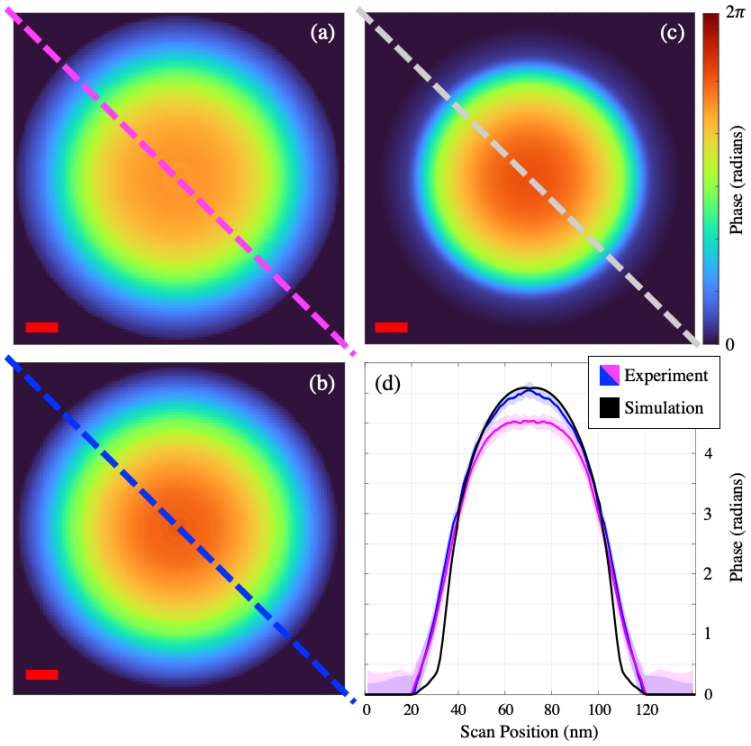

FIGURE 4.7. Reconstructed azimuthally averaged phase images of a latex NP from the raw 2GeMZI BF images with (a) constructive alignment (magenta) and (b) destructive alignment (blue). The simulated outcome (c) is also shown. (d) The experimental and simulated cross-sections of the reconstructed particle phase with shaded regions to show the error. All scale bars are 10 nm.

the expected maximum depending on the interferometer alignment and thickness profile of the NP is broader than is expected when simulating an incident probe with a 5 nm width, Figure 4.7(d). These deviations from the expected results can be attributed to the small, but non-negligible amplitude decay coefficient $\alpha^{\text{latex}} \neq 0$, as well as unexpected charging on the NP throughout the scan. Decoupling the amplitude loss and imparted phase with multiple probes is a subject of ongoing work and as of now is treated as a source of systematic error and charging effects can be mitigated through improved sample preparation procedures.

The 2GeMZI achieves qualitative phase imaging of static electric potentials and quantitative phase recovery of a latex NP with a phase resolution of $\delta\phi = 240\,\text{mrad}$; this is the standard deviation of $m = 0$ interferometer output order intensity converted to phase. The phase precision could be improved with enhanced gratings, a smaller probe size, longer exposure times with efficient charge alleviation, or by using a detector with a higher quantum efficiency. The spatial resolution of the 2GeMZI is limited by the focused probe width, which is tunable by selecting different convergence angles using the lens system. Since the holographic grating is used as both a beam splitter and a beam-defining aperture, the ratio of the maximum separation between probes to the width of those probes is constant and equal to the number of lines in the grating. Considering grating-based phase imaging has previously achieved 30 mrad phase and sub-nanometer spatial resolutions [126], there is promise for phase and spatial resolution improvements of this grating-based technique.

4.5. Chapter Summary

We constructed a scanning, path-separated, two-grating Mach-Zehnder interferometer (2GeMZI) for free electrons by employing two nanofabricated diffraction grating holograms in a conventional TEM. Although each figure of merit can be tuned or improved, the initial implementation shown here has an interference contrast of 82%, a path separation of up to 1 μm, a demonstrated phase resolution of $\delta\phi = 240\,\text{mrad}$, and an output current on the order of tens of picoamps. We qualitatively showed that the 2GeMZI is sensitive to phase shifts due to electrostatic potentials in vacuum by imaging the potential differences around both grounded and insulated silver vertical nanorods. We then quantitatively recovered the phase of a polysterene latex NP on graphene. The 2GeMZI is particularly impactful in free electron interferometry due to its tunable probe separation, the accessibility of individual paths, the ability to arbitrarily apply phase shifts between separate paths, its scanning capabilities, and the real-time phase information at the nanoscale.

With incremental improvements in grating beam splitters and detectors, the 2GeMZI could be used for interaction-free electron imaging [15, 94], low-dose STEM imaging [44, 127], nanoscale magnetic imaging [128], fundamental quantum physics experiments such as the Aharnov-Bohm effect [92, 129], and furthering decoherence theory [130, 131]. Subjects of ongoing work are decoupling the imparted phase and amplitude loss, enhancing the contrast at the detector, and improving the spatial and phase resolution. Due to the flexible design and broad applications, the 2GeMZI is uniquely positioned in electron microscopy to open doors to sub-nanometer electron interferometry and low-dose, high-resolution microscopy.

CHAPTER V

INTERFEROMETRIC PLASMON SCATTERING THEORY

In addition to nanoscale phase imaging, the two-grating electron interferometer can be used to coherently probe plasmons.

Notes for Ch. V:

This chapter is adapted from the supplementary material of a manuscript that is in preparation:

C. W. Johnson, A. E. Turner, F. J. Garcia de Abajo, and B. J. McMorran. Grating-Based Inelastic Mach-Zehnder Interferometry with Free Electrons. {*Manuscript in Preparation*}, 2021.

BJM, AET, and I developed the study for the paper. FJG initially conceived the experimental idea and interpreted the results. I performed the experiment and wrote the paper.

The energy loss probability of a single focused electron probe passing next to a metallic nanoparticle is well understood and is directly proportional to the experimentally measured electron energy loss spectra (EELS) in a TEM [30]. In this chapter we show how this loss probability behaves in the 2GeMZI output with multiple focused electron probes, and simulate the spectrally resolved interferometer output for a two-beam scan over a single spherical gold nanoparticle.

From this point on in this dissertation we will switch to the scattering coordinate convention outlined in Section 1.2.2 and illustrated in Figure 1.2(b).

5.1. Energy Loss Probability from a Focused Electron Probe

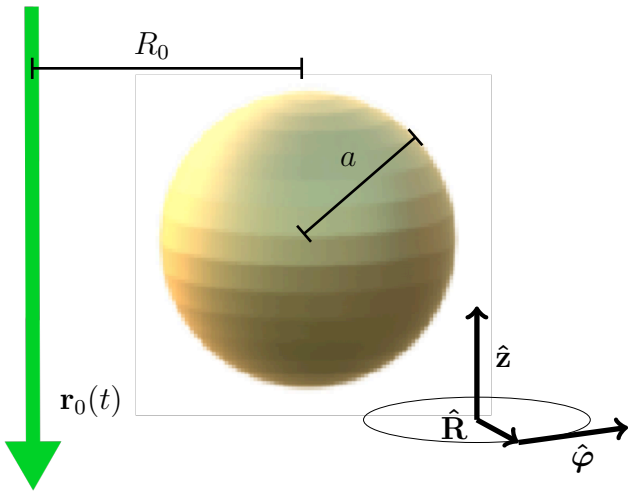

FIGURE 5.1. An electron with path $\mathbf{r}_0(t)$ at an impact parameter R_0 to a spherical metallic NP with radius a in a cylindrical coordinate system.

As mentioned in Section 1.2.5, a fast electron passing next to a surface will lose energy due to the dielectric response of the material. For metals, this dielectric response to the fast electron can be explained as collective oscillations of the conduction electrons in the material that are referred to as plasmons [132]. For individual metallic nanoparticles (NPs) these plasmon excitations are localized to the object and have a geometry dependent resonant mode structure where the energy dispersion of each mode is dependent on the material properties [133].

We can consider a fast electron passing next to a spherical metallic nanoparticle with radius a at an impact parameter R_0, see (Fig. 5.1). The energy resolved probability of the electron losing $\hbar\omega$ energy by exciting a localized plasmon resonance (LPR) while travelling at a velocity v along a straight vertical trajectory $\mathbf{r}_0(t) =$

$(R_0\cos(\varphi_0), R_0\sin(\varphi_0), z_0 - vt)$ can be written as

$$\Gamma^{\{1\mathrm{p}\}}(\omega, \mathbf{r}_0, \mathbf{r}_0') = \frac{e}{\pi\hbar\omega}\int dt\,\mathrm{Re}\left\{e^{-i\omega t}\mathbf{v}\cdot\mathbf{E}^{ind}_{\mathbf{r}_0'}(\mathbf{r}_0(t),\omega)\right\}, \tag{5.1}$$

where the $\{1\mathrm{p}\}$ superscript stands for one probe, and the electric field is induced by the dielectric response of the NP due to the external electric field of the electron. A fully relativistic analytic solution to Equation (5.1) can be found by expanding the induced electric field due the retarded dielectric response of the spherical NP by a multipole expansion of its Green's function representation, giving

$$\begin{aligned}\Gamma^{\{1\mathrm{p}\}}(\omega, \mathbf{r}_0, \mathbf{r}_0') = \frac{e^2}{\hbar\omega c}\sum_{l=1}^{\infty}\sum_{m=-l}^{l} K_m\left(q_\gamma R_0\right) K_m\left(q_\gamma R_0'\right)\left[C^M_{lm}\mathrm{Im}\{t^M_l(\omega)\} + C^E_{lm}\mathrm{Im}\{t^E_l(\omega)\}\right] \\ \times \mathrm{Re}\{e^{-im(\varphi_0-\varphi_0')-i\omega(z_0-z_0')/v}\},\end{aligned} \tag{5.2}$$

where K_m is a modified Bessel function of the second kind, $q_\gamma = \omega/v\gamma$ with γ the Lorentz factor, C^M_{lm} and C^E_{lm} are the magnetic and electric coupling constants, and t^M_l and t^E_l are the scattering matrix elements given by Mie scattering theory. The latter are written explicitly as

$$\begin{aligned} t^M_l(\omega) &= \frac{-j_l(\rho_0)\rho_1\frac{d\,j_l(\rho_1)}{d\rho_1} + \rho_0\frac{d\,j_l(\rho_0)}{d\rho_0}j_l(\rho_1)}{h^{(+)}_l(\rho_0)\rho_1\frac{d\,j_l(\rho_1)}{d\rho_1} - \rho_0\frac{d\,h^{(+)}_l(\rho_0)}{d\rho_0}j_l(\rho_1)} \\ t^E_l(\omega) &= \frac{-j_l(\rho_0)\frac{d\,[\rho_1 j_l(\rho_1)]}{d\rho_1} + \epsilon(\omega)\frac{d\,[\rho_0 j_l(\rho_0)]}{d\rho_0}j_l(\rho_1)}{h^{(+)}_l(\rho_0)\frac{d\,[\rho_1 j_l(\rho_1)]}{d\rho_1} - \epsilon(\omega)\frac{d\,[\rho_0 h^{(+)}_l(\rho_0)]}{d\rho_0}j_l(\rho_1)} \end{aligned} \tag{5.3}$$

where $\rho_0 = \omega a/c$, $\rho_1 = \omega a\sqrt{\epsilon(\omega)}/c$, $\epsilon(\omega)$ is the dielectric function of the NP, c is the speed of light, and j_l and $h^{(+)}_l$ are spherical Bessel and Hankel functions respectively. Although in this case we evaluate the induced field at the location of the passing

electron, $\mathbf{r}_0(t) = \mathbf{r}'_0(t)$, we have shown them explicitly as it will be important to know where the contributions come from in the next section. A full derivation of Equation (5.2), explanation of Equation (5.3), as well as closed forms of the coupling constants C_{lm}^M and C_{lm}^E can be found here [134].

For a gold NP with 30 nm radius and 80 keV electrons, the electric contribution to the energy loss probability is much larger than the magnetic contribution in the 1-6 eV region where the plasmon resonance peaks are, i.e. $C_{lm}^E \mathrm{Im}\{t_l^E\} \gg C_{lm}^M \mathrm{Im}\{t_l^M\}$. So we will neglect the magnetic contribution in the following analysis, giving

$$\Gamma^{\{1\mathrm{p}\}}(\omega, R_0) \approx \frac{e^2}{\hbar\omega c} \sum_{l=1}^{\infty} \sum_{m=-l}^{l} K_m \left(q_\gamma R_0\right)^2 C_{lm}^E \mathrm{Im}\{t_l^E(\omega)\} = \sum_{l=1}^{\infty} \Gamma_l^{\{1\mathrm{p}\}}(\omega, R_0), \quad (5.4)$$

where the $l = 1$, $l = 2$, etc. terms correspond to the dipole, quadrupole, etc. loss probabilities, respectively and

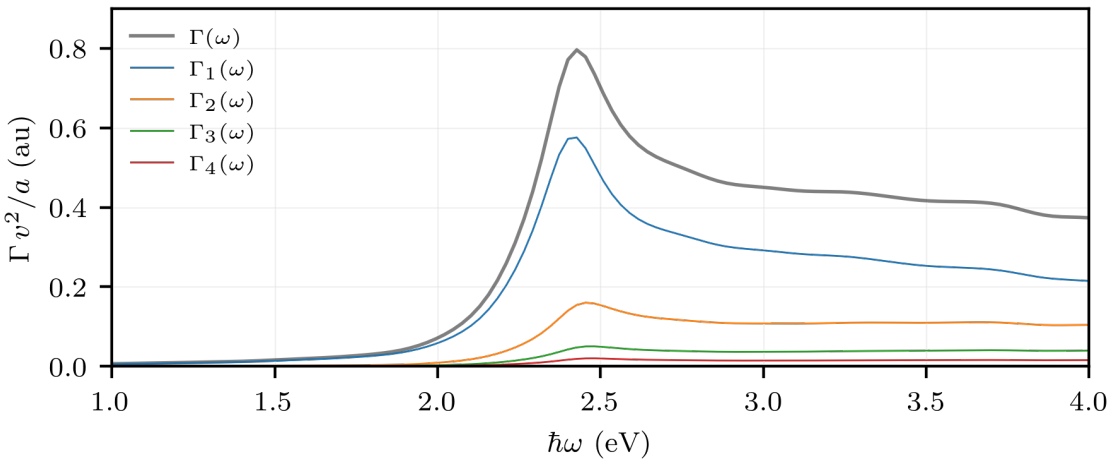

FIGURE 5.2. Calculated one-probe energy loss probability for an $a = 30$ nm radius gold NP excited from a focused electron beam at an impact parameter of $R_0 = 1.2a$.

$$\Gamma_l^{\{1p\}}(\omega, R_0) \equiv \frac{e^2}{\hbar\omega c} \sum_{m=-l}^{l} K_m \left(q_\gamma R_0\right)^2 C_{lm}^E \mathrm{Im}\{t_l^E(\omega)\}. \tag{5.5}$$

Using numerically tabulated values for dielectric function of gold [135], we plot the different multipole components of the energy loss probability for the gold NP to show that the LPR multipole peaks around 2.4 eV are not spectrally resolvable, but the $l = 1$ dipole mode has the largest contribution to the spectrum, Figure 5.2.

5.2. Multiple Focused Electron Probes in a 2GeMZI

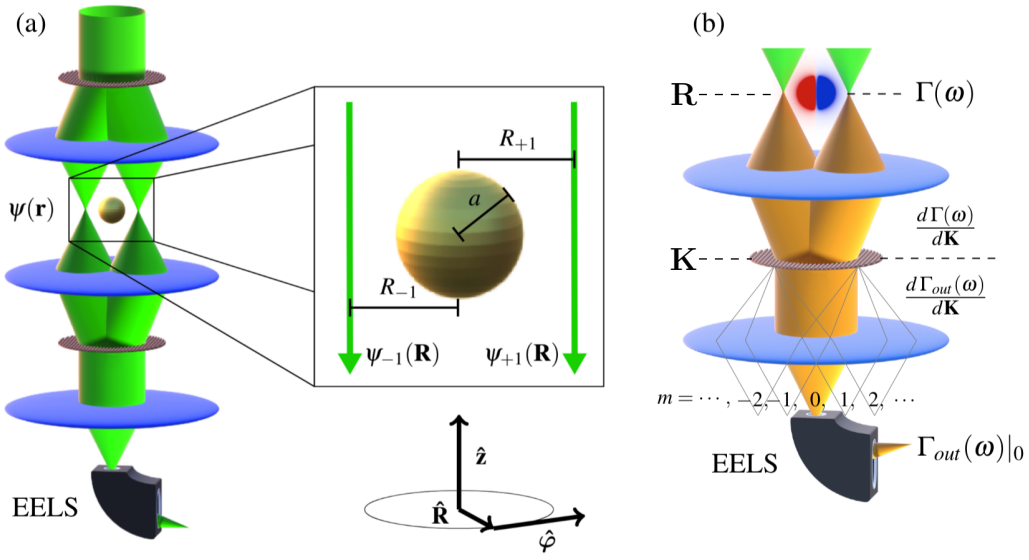

FIGURE 5.3. (a) Diagram of two focused electron probes incident on a NP in the 2GeMZI. (b) The scattering geometry within the 2GeMZI. Focused electron probes in the specimen plane, with coordinates $\mathbf{R} = (x, y)$, excite an NP LPR with probability Γ. In the back focal plane, with coordinates $\mathbf{K} = (k_x, k_y)$, the overlapping beams have a transverse momentum resolved loss probability $d\Gamma/d\mathbf{K}$. The second 2GeMZI grating redirects these beams to be co-propagating in the interferometer output with corresponding transverse momentum resolved loss probability $d\Gamma_{out}/d\mathbf{K}$. Finally, the entrance aperture of the EELS spectrometer selects the $m = 0$ interferometer output order to resolve the combined two-probe loss probability $\Gamma_{out}|_0$.

The input grating of a 2GeMZI creates a superposition of electron probes spatially separated in the specimen plane each with a well defined relative phases. We can write the electron wavefunction as the longitudinal plane wave superposition $\psi(\mathbf{r}) = e^{ik_z z}\sum_j \psi_j(\mathbf{R}) \equiv e^{ik_z z}\psi_\perp(\mathbf{R})$, where each transverse probe wavefunction can be approximated as a delta function with a complex amplitude $\psi_j(\mathbf{R}) \approx c_j\delta(\mathbf{R}-j\mathbf{R}_0)$, with $c_j = |c_j|e^{i\phi_j}$ being proportional to the Fourier coefficients attributed to the periodic shape of the 2GeMZI input grating and $\mathbf{R}_0 \propto 1/p_0$ is the probe spacing for a grating with pitch p_0, i.e., each probe at the specimen plane is the jth diffraction order from interferometer input grating, Figure 5.3(a). In the far field after this interaction the electron probes from the sample plane expand to their transverse momentum distributions and, as shown in Figure 5.3(b), recombine at the output 2GeMZI grating in the back focal plane where the energy loss probability is resolved by its transverse momentum $d\Gamma/d\mathbf{K}$. To find the energy loss probability for this electron wavefunction we must move to the quantum mechanical formalism from Section 1.2.5.2 that is capable of including explicit wave properties of the electrons after the interaction. Plugging the superposition of probes at the specimen into the transverse momentum resolved loss probability from Equation (1.15) gives

$$\begin{aligned}\frac{d\Gamma(\omega)}{d\mathbf{K}} &= \frac{e^2}{\pi^2\hbar}\sum_{j,j'}\int d^3\mathbf{r}\, d^3\mathbf{r}'\, \left(\psi_j(\mathbf{R})e^{-i\mathbf{K}\cdot\mathbf{R}}\right)^* \left(\psi_{j'}(\mathbf{R})e^{-i\mathbf{K}\cdot\mathbf{R}}\right) \\ &\qquad\qquad \times \mathrm{Im}\left\{-G_{\mathbf{zz}}(\omega,\mathbf{R},\mathbf{R}',z,z')\right\} \\ &\propto \sum_{j,j'}\left(c_j e^{-ij\mathbf{R}_0\cdot\mathbf{K}}\right)^*\left(c_{j'}e^{-ij'\mathbf{R}_0\cdot\mathbf{K}}\right) \\ &\qquad\qquad \times \int dz dz'\, e^{-i\omega(z-z')/v}\mathrm{Im}\left\{-G_{\mathbf{zz}}(\omega,j\mathbf{R}_0,j'\mathbf{R}_0,z,z')\right\},\end{aligned} \tag{5.6}$$

where $G_{\mathbf{zz}} = \mathbf{z} \cdot G \cdot \mathbf{z}$ is a component of the electromagnetic dyadic Green's function [30].

In the weak phase approximation upon transmission through the output grating, the passing unscattered wavefunction $\psi_\perp(\mathbf{K}) \propto \int d^2\mathbf{R}\psi_\perp(\mathbf{R})e^{-i\mathbf{K}\cdot\mathbf{R}} = \sum_j c_j e^{-ij\mathbf{R}_0\cdot\mathbf{K}}$ is multiplied by the grating transmission function $e^{i\widetilde{\Phi}t(\mathbf{K})}$, where $\widetilde{\Phi}$ contains the phase shift and amplitude loss per unit thickness of the grating, and $t(\mathbf{K})$ is the periodic thickness profile of the grating. Since t is periodic, the whole transmission function can be written as the Fourier series $e^{i\widetilde{\Phi}t(\mathbf{K})} = \sum_k \tilde{c}_k e^{ik\mathbf{R}_0\cdot\mathbf{K}}$, where, in this case, the probe plane spacing $\mathbf{R}_0 \propto 1/p_0$ corresponds to the spatial frequency for the output grating with pitch p_0 in the $\mathbf{K}$ plane and $\tilde{c}_k$ are the Fourier coefficients for transmission function. The unscattered transverse wavefunction out of the second interferometer grating is then

$$\begin{aligned} \psi_{\perp\text{out}}(\mathbf{K}) &= e^{i\widetilde{\Phi}t(\mathbf{K})}\psi_\perp(\mathbf{K}) \\ &\propto \sum_{j,k} c_j\tilde{c}_k e^{i(k-j)\mathbf{R}_0\cdot\mathbf{K}}. \end{aligned} \tag{5.7}$$

From here we can see that all the terms that contribute to the $m = 0$ interferometer output diffraction order must satisfy the condition $k = j$.

Similarly, in the Equation (5.6) we multiply both wavefunctions by the output grating transmission function to find the transverse momentum resolved loss probability of the 2GeMZI output

$$\begin{aligned} \frac{d\Gamma_{\text{out}}(\omega)}{d\mathbf{K}} \propto \sum_{j,k,j',k'} &\left(c_j\tilde{c}_k e^{i(k-j)\mathbf{R}_0\cdot\mathbf{K})}\right)^* \left(c_{j'}\tilde{c}_{k'} e^{i(k'-j')\mathbf{R}_0\cdot\mathbf{K})}\right) \\ &\times \int dz\, dz'\, e^{-i\omega(z-z')/v}\text{Im}\left\{-G_{\mathbf{zz}}(\omega, j\mathbf{R}_0, j'\mathbf{R}_0, z, z')\right\}. \end{aligned} \tag{5.8}$$

The plane waves with in each of the parentheses must now satisfy $j = k$ and $j' = k'$ to contribute to the 0^{th} output diffraction order of the 2GeMZI

$$\begin{aligned}\left.\frac{d\Gamma_{\text{out}}(\omega)}{d\mathbf{K}}\right|_0 &= \frac{d\Gamma_{\text{out}}(\omega)}{d\mathbf{K}}\delta_{j,k}\delta_{j',k'} \\ &\propto \sum_{j,j'} c_j^* c_{j'} \tilde{c}_j^* \tilde{c}_{j'} \int dz\, dz'\, e^{-i\omega(z-z')/v} \text{Im}\left\{-G_{\mathbf{zz}}(\omega, j\mathbf{R}_0, j'\mathbf{R}_0, z, z')\right\}.\end{aligned} \tag{5.9}$$

By integrating over $\mathbf{K}$ and normalizing over the area of integration we can find the energy loss probability when only the entire $m = 0$ 2GeMZI output order is selected by an EELS entrance aperture as depicted in Figure 5.3, giving

$$\begin{aligned}\Gamma_{\text{out}}(\omega)\big|_0 \propto& \sum_{j,j'} |c_j c_{j'} \tilde{c}_j \tilde{c}_{j'}| \cos(\Delta\phi_{j,j'}) \\ &\times \int dz\, dz'\, e^{-i\omega(z-z')/v} \text{Im}\left\{-G_{\mathbf{zz}}(\omega, j\mathbf{R}_0, j'\mathbf{R}_0, z, z')\right\},\end{aligned} \tag{5.10}$$

where $\Delta\phi_{j,j'} = \phi'_j - \phi_j$ are the relative probe phases and we have also made the assumption that the Fourier coefficients are even under inversion of their indices $c_j = c_{-j}$, as is the case with the binary gratings of the 2GeMZI. The integral over z and z' in Equation (5.10) is equivalent to Equation (5.1) with $\mathbf{r}_0$ and $\mathbf{r}'_0$ allowed to differ and written in the Green's function formalism. With this we can write

$$\begin{aligned}\Gamma_{\text{out}}(\omega)\big|_0 \propto& \sum_j |c_j \tilde{c}_j|^2 \Gamma^{\{1\text{p}\}}(\omega, jR) \\ &+ 2\sum_{j,j'>j} |c_j c_{j'} \tilde{c}_j \tilde{c}_{j'}| \Gamma^{\{int\}}(\omega, j\mathbf{R}_0, j'\mathbf{R}_0, \Delta\phi_{j,j'}),\end{aligned} \tag{5.11}$$

where the two-path interference terms are given by

$$\begin{aligned}\Gamma^{\{int\}}(\omega,\mathbf{R}_j,\mathbf{R}_{j'},\Delta\phi_{j,j'}) &= \frac{e^2}{\hbar\omega c}\sum_{l=1}^{\infty}\sum_{m=-l}^{l} K_m\left(q_\gamma R_j\right) K_m\left(q_\gamma R_{j'}\right) C_{lm}^{E}\mathrm{Im}\{t_l^E(\omega)\} \\ &\qquad\qquad \times\cos\left(\Delta\phi_{j,j'}\right)\cos(m\Delta\varphi_{j,j'}) \\ &= \sum_{l=1}^{\infty}\Gamma_l^{\{int\}}(\omega,\mathbf{R}_j,\mathbf{R}_{j'},\Delta\phi_{j,j'}),\end{aligned} \tag{5.12}$$

where again, $\Gamma_l^{\{int\}}$ are the l multipole components. In the case where the input and output gratings of the 2GeMZI are optimized to create only two probes in the $j=\pm1$ orders at $\mathbf{R}_{-1}$ and $\mathbf{R}_{+1}$, Figure 5.3, then we have the condition $c_{|m|\neq1}\approx\tilde{c}_{|m|\neq1}\approx0$ giving

$$\begin{aligned}\Gamma_{\mathrm{out}}^{\{2\mathrm{p}\}}(\omega)\big|_0 &\propto \Gamma^{\{1\mathrm{p}\}}(\omega,R_{-1})+\Gamma^{\{1\mathrm{p}\}}(\omega,R_{+1})+2\Gamma^{\{\mathrm{int}\}}(\omega,\mathbf{R}_{-1},\mathbf{R}_{+1},\Delta\phi) \\ &= \sum_{l=1}^{\infty}\Gamma_l^{\{1\mathrm{p}\}}(\omega,R_{-1})+\Gamma_l^{\{1\mathrm{p}\}}(\omega,R_{+1})+2\Gamma_l^{\{\mathrm{int}\}}(\omega,\mathbf{R}_{-1},\mathbf{R}_{+1},\Delta\phi),\end{aligned} \tag{5.13}$$

where we have dropped the subscripts for $\Delta\phi=\phi_{-1}-\phi_{+1}$.

5.3. Inelastic Interference in the 2GeMZI by Multipole Components

The relative phase difference between the two 2GeMZI probes have contributions from the internal interferometer alignment as well as from any external static potential the probes pass through

$$\Delta\phi=\Delta\phi_{\mathrm{internal}}+\Delta\phi_{\mathrm{external}}. \tag{5.14}$$

Taking two interferometric spectra with different interferometer alignments $\Delta\phi_{\text{internal}} = 0$ and $\Delta\phi_{\text{internal}} = \pi$ gives

$$\begin{aligned}
\Gamma^{\{2\text{p}\}}_{out}(\omega, \Delta\phi_{\text{internal}} = 0)\big|_0 &= \Gamma^{\{1\text{p}\}}(\omega, R_{-1}) + \Gamma^{\{1\text{p}\}}(\omega, R_{+1}) \\
&\quad + 2\Gamma^{\{int\}}(\omega, \mathbf{R}_{-1}, \mathbf{R}_{+1}, \Delta\phi_{\text{external}}) \\
\Gamma^{\{2\text{p}\}}_{out}(\omega, \Delta\phi_{\text{internal}} = \pi)\big|_0 &= \Gamma^{\{1\text{p}\}}(\omega, R_{-1}) + \Gamma^{\{1\text{p}\}}(\omega, R_{+1}) \\
&\quad - 2\Gamma^{\{int\}}(\omega, \mathbf{R}_{-1}, \mathbf{R}_{+1}, \Delta\phi_{\text{external}}).
\end{aligned} \tag{5.15}$$

With this we can express the interference component as

$$\begin{aligned}
\Gamma^{\{int\}}(\omega, \mathbf{R}_{-1}, \mathbf{R}_{+1}, \Delta\phi_{\text{external}}) = \frac{1}{4}\Big(&\Gamma^{\{2\text{p}\}}_{out}(\omega, \Delta\phi_{\text{internal}} = 0)\big|_0 \\
&- \Gamma^{\{2\text{p}\}}_{out}(\omega, \Delta\phi_{\text{internal}} = \pi)\big|_0\Big).
\end{aligned} \tag{5.16}$$

As discussed in Chapter 4, the 2GeMZI can be used in an imaging mode that scans the probes across a specimen. We can use this scanning capability to not only record an output intensity at every scan location, but also an energy spectrum for every scan location. This is no different than what is displayed in Figure 4.2, except instead of using a bright field single pixel detector we use an EELS spectrometer allowing us to create interferometric spectrum images by selectively integrating the intensity energy windows.

Also recall from Chapter 4 that electrostatic potentials that can build up throughout an imaging scan creating a spatially dependent external phase shift between the probes, $\Delta\phi_{\text{external}}$. Since spectrum imaging is much less dose efficient than imaging with a bright field detector, requiring much longer dwell times per pixel, we can expect a considerable amount of charging throughout a spectrum imaging scan. Experimentally we use amorphous carbon support films to support

gold nanoparticles in a TEM. We simulate interferometric images of a gold NP with a $V_z \propto 1/r + 30/(y - y_0)$ potential to approximate the projected potential phase shift applied to each probe for the $l = 1-4$ multipole modes from surface charge on the NP and amorphous carbon support, where the $1/r$ term comes from the gold NP and the $1/y$ term comes from the carbon support. These carbon supports can have much more surface area than a 30 nm radius NP and a lower conductivity than gold, supporting a larger surface charge throughout the scan and the 30 times larger $1/y$ potential was chosen as an estimation to fit the experimental data in the next chapter. These simulations include interferometer phase shifts $\Delta\phi_{\text{internal}} = 0$ and $\Delta\phi_{\text{internal}} = \pi$, allowing us to also show $\Gamma_l^{\{int\}}(\omega, \mathbf{R}_{-1}, \mathbf{R}_{+1}, \Delta\phi_{\text{external}})$, Fig. 5.4. As expected, the $l = 1$ dipole mode dominates, but there can be considerable contribution from the higher order modes, especially near the edge of the NP.

When the probe separation direction is parallel to the carbon support the $1/y$ part of the projected potential exactly cancels in the phase difference, Figure 5.4. Introducing an angular offset between the probe separation direction and the carbon support introduces an asymmetric potential that can be used to impart a position dependent phase shift to the two probes. Figure 5.5 shows this effect for a 5° angular offset. This allows for a convenient way to image the interference fringes in the interferometer output as a function of continuously varying relative phase.

5.4. Chapter Summary

We have developed the theory for how the EELS probability of plasmon excitation with multiple STEM probes behaves in the output of the 2GeMZI that is general

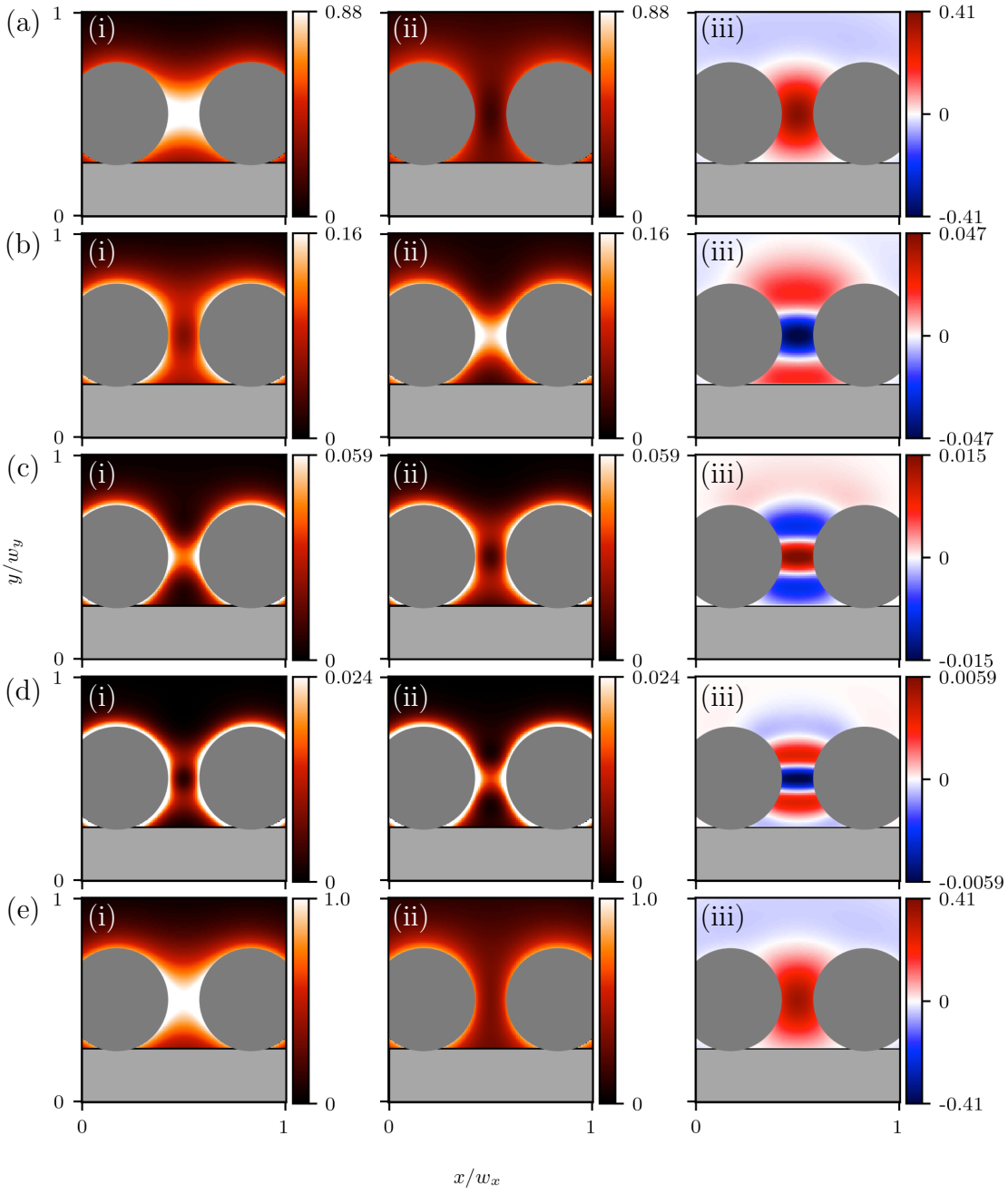

FIGURE 5.4. Simulated interferometric spectrum images of a single $a = 30$ nm gold nm NP over a 120×120 nm^2 scan region with a probe separation of 80 nm and $w_x = w_y = 120$ nm. Spectra were integrated over the energy range 1-3 eV. (a) $l = 1$, (b) $l = 2$, (c) $l = 3$, (d) $l = 4$, and (e) $\sum_{l=1}^{4}$. With corresponding (i) $\Gamma_l(\omega)$ spectrum images for $\Delta\phi_{\text{internal}} = 0$, (ii) $\Gamma_l(\omega)$ spectrum images for $\Delta\phi_{\text{internal}} = \pi$, and (iii) $\Gamma_l^{\{int\}}(\omega)$ spectrum images. All colorbar scales are normalized to the maximum intensity of (e)(i).

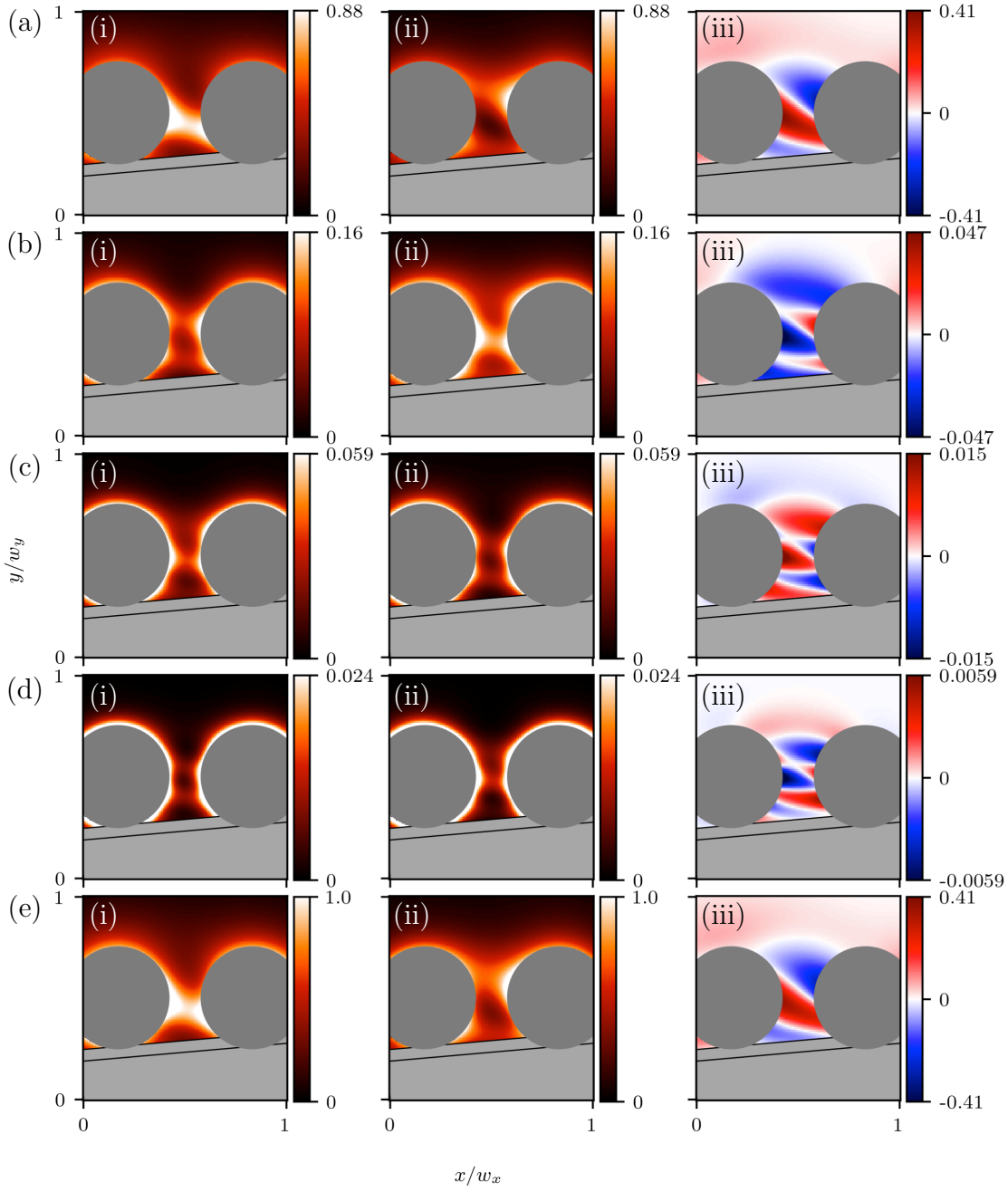

FIGURE 5.5. Simulated interferometric spectrum images of a single $a = 30$ nm gold nm NP over a 120×120 nm^2 scan region with a probe separation of 80 nm and $w_x = w_y = 120$ nm. Spectra were integrated over the energy range 1-3 eV. (a) $l = 1$, (b) $l = 2$, (c) $l = 3$, (d) $l = 4$, and (e) $\sum_{l=1}^{4}$. With corresponding (i) $\Gamma_l(\omega)$ spectrum images for $\Delta\phi_{\text{internal}} = 0$, (ii) $\Gamma_l(\omega)$ spectrum images for $\Delta\phi_{\text{internal}} = \pi$, and (iii) $\Gamma_l^{\{int\}}(\omega)$ spectrum images. All colorbar scales are normalized to the maximum intensity of (e)(i).

to the geometry of the plasmonic nanostructure and interferometer alignment. We use this to simulate EELS signal for a two-probe excitation of a single metallic gold nanoparticle in bare vacuum as well as in the presence of a static electric potential at the sample.

CHAPTER VI

INELASTIC INTERFEROMETRY EXPERIMENT

The two-grating electron interferometer described in Chapter IV can be used to explore the plasmon scattered inelastic electron interferometry outlined in Chapter V.

Notes for Ch. VI:

This chapter is adapted from a manuscript that is in preparation:

C. W. Johnson, A. E. Turner, F. J. Garcia de Abajo, and B. J. McMorran. Grating-Based Inelastic Mach-Zehnder Interferometry with Free Electrons. {*Manuscript in Preparation*}, 2021.

BJM, AET, and I developed the study for the paper. FJG initially conceived the experimental idea and interpreted the results. I performed the experiment and wrote the paper.

Free electrons (FE) in a transmission electron microscope (TEM) are ideal for probing individual, nanoscale plasmonic systems [30] due to their picometer wavelengths allowing for Ångstrom resolution imaging and their ability to couple with electromagnetic fields. These interactions can be measured with electron energy loss spectroscopy (EELS) that is sensitive to the photonic local density of states of materials, but not sensitive to the sign or phase of the excited field [136]. In general, plasmonic excitations and their radiated fields are phase coherent; this phase information is passed on to the scattered FE, motivating the use of electrons as quantum probes in the detection and manipulation of nanoplasmonic systems

[25]. There have been multiple experiments in TEMs to exploit this phase coherence after inelastic electron-matter interactions. Inelastic holography is an interferometric technique using an electrostatic biprism to interfere different parts of an electron plane wave after interacting with the sample; specifically looking at the coherent interference of the inelastically scattered electrons. This has been used to measure the coherence properties of bulk and surface plasmon excitations [137, 138], as well as measure the loss of coherence due to the Coulomb interaction [20], but requires a high degree of electron spatial coherence. The partial coherence of the electron source and multiple final scattering states after excitation with broad illumination complicates the analysis and interpretation of measured signals [105, 139, 140]. An alternative approach is to shape the transverse wavefront of a single electron longitudinal plane wave mode and use this shaped transverse mode to match the spatial extent and phase of the plasmonic near field. Post-selection of the coherent scattered wavefront by selecting a small transverse area with a circular aperture in the far field can act as a spatial mode filter. A successful demonstration of this wavefront selection has shown discrimination between the dipole an quadrupole localized plasmon resonance (LPR) modes of a metallic nanorod with a Hermite-Gaussian beam [23]. It has also been proposed to measure the transfer of orbital angular momentum [141]. However, post-selection by spatially filtering wavefronts is very dose inefficient and requires precise simultaneous alignments of the structured electron wavefront at the specimen as well as the and selection apertures in the far field for filtering. These plasmonic interactions can be resonantly enhanced by temporally and spatially matching pulses of probe electrons with plasmonic near fields excited an by external optical pump [22]. This has been very successful in the detection and manipulation of plasmonic systems and the longitudinal electron wavefunction [13], but requires highly specialized TEMs

and optical systems. A robust electron Mach-Zehnder interferometer with scanning, spatially separated paths, phase tunability, and discrete, co-propagating outputs could not only improve on many of these approaches, but it can also open the door to a diverse range of interferometric experiments that were not possible before.

Mach-Zehnder interferometers [108, 116, 117] or crystal plane interferometers [114, 115] for electrons have previously been demonstrated, but all have either had poorly-defined separation between paths, no ability to vary the relative phase between probes, or no ability scan the separate paths relative to a sample of interest. More recently, improvements in the fabrication of electron phase gratings [31] has allowed for the implementation of an efficient and phase tunable two-grating electron Mach-Zehnder interferometer (2GeMZI) in a TEM [89]. The 2GeMZI is constructed with an amplitude dividing beamsplitter grating [43] forming tightly focused probes to interrogate a sample. After the sample the probes pass through a second grating recombining the separate paths for co-propagation to a detector. With flexible control over the relative probe positions and phases, the 2GeMZI can conveniently match plasmon resonance modes. Co-propagation in the interferometer output allows for complete interference, mitigating the need for post-selection apertures and reducing the complexity of the analysis and interpretation of the interference. Inelastic interferometry with 2 phase coherent probes after scattering from plasmonic near fields in the 2GeMZI combines the concepts of transverse beam shaping and inelastic holography gaining all the individual techniques capabilities while mitigating their faults, all accomplished by only modifying the two apertures of a conventional TEM.

We use a two-probe 2GeMZI to image the interference of coherent superpositions of electrons inelastically scattered by self-induced LPR excitations of an individual

spherical gold nanoparticle (NP). The interferometer output is projected onto a real-space image plane and collected by an EELS system where the plasmon scattered electrons can be spectrally resolved from the zero loss peak (ZLP), (Fig. 6.1). The relative phase between the two probes in the interferometer output can be arbitrarily tuned by shifting the incident image of the input grating (G1) with respect to the output grating (G2), or by passing the probes through a spatially varying electrostatic potential. This is used to show phase-sensitive enhancement and suppression of the dipole LPR spectral peak in the output of the interferometer that is out of phase with the interference of the elastically scattered electrons. This demonstrates that electrons in a coherent superposition of paths can interact inelastically with an environment and still retain coherence.

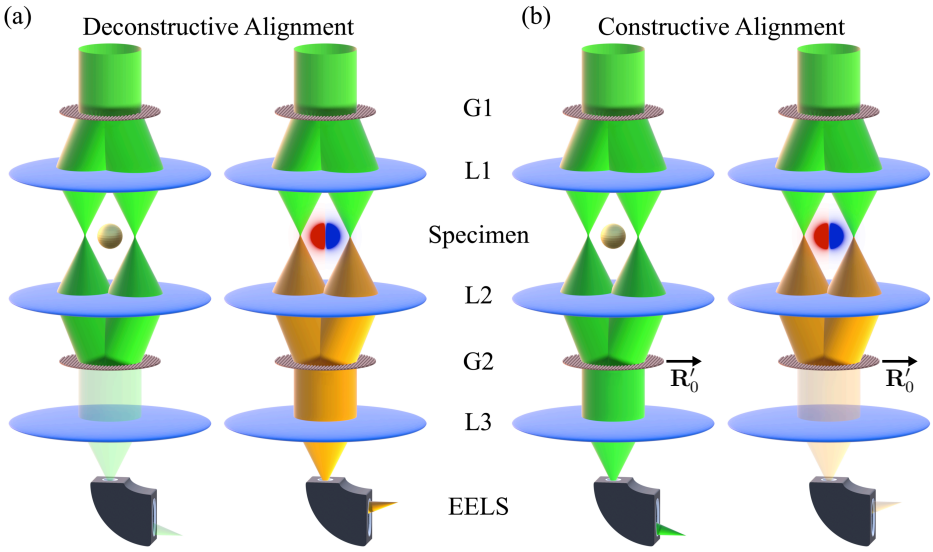

FIGURE 6.1. Qualitative diagram of interferometer constructed from gratings (G1, G2) and magnetic lenses (L1, L2, L3) with a gold NP in the specimen plane (Sp) and EELS spectrometer for two different interferometer alignments. Converse interference relationship between the green ZLP electrons and orange dipole plasmon scattered electrons spectrally resolved for (a) a deconstructive and (b) a constructive 2GeMZI alignment.

6.1. Plasmon Scattering in the 2GeMZI

The electric field from a fast electron STEM probe passing next to a metallic NP causes excitations of localized plasmon resonances (LPR). The induced electric field produced by the LPR then acts back on the passing electron, causing a loss of energy; the probability of an $\hbar\omega$ amount of energy being lost by a passing electron with a straight vertical trajectory $\mathbf{r}_0(t) = (R_0\cos(\varphi_0), R_0\sin(\varphi_0), z_0 - vt)$ can be expressed as a relativistic multipole expansion,

$$\Gamma^{\{1\mathrm{p}\}}(\omega, R_0) = \frac{e^2}{\hbar\omega c}\sum_{l=1}^{\infty}\sum_{m=-l}^{l} C_{lm}^{E}\mathrm{Im}\{t_l^E(\omega)\}K_m(q_\gamma R_0)^2, \tag{6.1}$$

where the superscript $\{1\mathrm{p}\}$ denotes one STEM probe at the sample plane, C_{lm}^E is a coupling constant depending on v/c, $t_l^E(\omega)$ is the electric Mie scattering matrix element, K_m are modified Bessel function of the second kind, and $q_\gamma = \omega/v\gamma$ is a Lorentz factor scaled energy loss wave number [134]. The sum over l is a sum over the multipole components, i.e., $l = 1$, $l = 2, \cdots$ correspond to the dipole, quadrupole, etc. modes. For a gold NP with radius $a = 30$ nm, the dipole mode dominates, but for impact parameters close to the radius of the NP $a < R_0 < 1.2a$ the higher order multiple modes can have more significant contributions.

In the 2GeMZI, the G1 puts a majority of the transmitted electrons into 2 equal intensity diffraction orders. These probes focused to the sample plane with an NP can be approximated by the longitudinal plane wave superposition of two delta functions $\psi(\mathbf{r}) = e^{ik_z z}(c_1\delta(\mathbf{R} - \mathbf{R}_{-1}) + c_2\delta(\mathbf{R} - \mathbf{R}_{+1}))$, where $c_j = |c_j|e^{i\phi_j}$ are complex amplitudes, and $\mathbf{R}_j = (R_j\cos(\varphi_j), R_j\sin(\varphi_j))$ are the impact parameters for each probe in the transverse plane separated by the constant $\mathbf{b} = \mathbf{R}_{-1} - \mathbf{R}_{+1}$. G2 redirects the two paths to be spatially overlapped and co-propagating. In this

case, the EELS probability is modified to include individual loss probabilities for each probe, but also an interference term that describes the energy loss due to the electron wave component at $\mathbf{R}_{-1}$ traveling through the electric field induced by the NPs response to the electron wave component at $\mathbf{R}_{+1}$, and vice versa

$$\begin{aligned}\Gamma^{\{2p\}}(\omega, \mathbf{R}_{-1}, \mathbf{R}_{+1}) = \Gamma^{\{1p\}}(\omega, R_{-1}) + \Gamma^{\{1p\}}(\omega, R_{+1}) \\ + 2\Gamma^{\{int\}}(\omega, \mathbf{R}_{-1}, \mathbf{R}_{+1}, \Delta\phi),\end{aligned} \tag{6.2}$$

with the interference term

$$\begin{aligned}\Gamma^{\{int\}}(\omega, \mathbf{R}_{-1}, \mathbf{R}_{+1}, \Delta\phi) = \frac{e^2}{\hbar\omega c}\sum_{l=1}^{\infty}\sum_{m=-l}^{l} C_{lm}^{E}\mathrm{Im}\{t_l^E(\omega)\} \\ \times K_m(q_\gamma R_{-1})K_m(q_\gamma R_{+1}) \\ \times \cos(\Delta\phi)\cos(m\Delta\varphi),\end{aligned} \tag{6.3}$$

where we have defined $\Delta\phi = \phi_{-1} - \phi_{+1}$ and $\Delta\varphi = \varphi_{-1} - \varphi_{+1}$. A derivation of this result can found in the previous chapter. We should note that this analysis neglects the inelastic momentum transfer applied to the passing electron in the transverse direction. Near the edge of a metallic NP at TEM energies this can cause a center of mass angular displacement on the order of 1 μrad in the far field at G2 [142]. Yet, with the STEM probe convergence angle on the order of 1 mrad, this effect is negligible.

When the two probes are scanned such that they pass in small regions on opposite sides of an NP, we have the condition $\Delta\varphi \approx \pi$. By only considering the dipole mode that dominates the plasmonic response of the NP we can expect a converse interference relation between ZLP intensity output of interferometer, proportional to $\cos(\Delta\phi/2)^2$, and the interference of the dipole plasmon scattered

electrons proportional to $\sin(\Delta\phi/2)^2$. This can be understood as a consequence of the overlap integral of the electron wavefunction and the dipole plasmon mode function that has odd parity [23].

6.2. Phase Sensitivity of the 2GeMZI

The 2GeMZI can be aligned to have any relative phase shift between the two probes by shifting the relative position of G1 and G2. If G2 is shifted by the amount $\mathbf{R}'_0$, then the phase difference between the two co-propagating probes in the output is $2\mathbf{K}_0 \cdot \mathbf{R}'_0$; to change the interferometer output from constructive to deconstructive interference requires the relative grating shift by a quarter grating pitch, $|\mathbf{R}'_0| = p_0/4$. The 2GeMZI is also sensitive to relative phase differences introduced to the two paths. One important source of this external phase shift to consider is due to a nonuniform electrostatic potential. In the weak phase approximation [118], a position dependent phase shift accumulated by a path due to a potential $V(\mathbf{r})$ is $\sigma V_z(\mathbf{R})$, where $\sigma = 2\pi me\lambda/h^2$ is the first order interaction parameter of an electron with relativistic de Broglie wavelength λ and relativistic mass m, and $V_z(\mathbf{R}) = \int dz\, V(\mathbf{r})$ is the projected static potential along z. The total relative phase difference between the two probes is then $\Delta\phi = \Delta\phi_{\text{internal}} + \Delta\phi_{\text{external}}$ where $\Delta\phi_{\text{internal}} = 2\mathbf{K}_0 \cdot \mathbf{R}'_0$ is due to the interferometer alignment, and $\Delta\phi_{\text{external}} = \sigma(V_z(\mathbf{R}_{-1}) - V_z(\mathbf{R}_{+1}))$ is the external phase shift due to a static potential.

When the electron beams are rastered across an NP object it is continually pumping current into the system and reaches an equilibrium of static surface charge. For an NP on the edge of a lacey carbon support, we approximate the projected static potential in the surrounding vacuum region as $V_z(\mathbf{R}) \propto 1/R + 30/(y - y_0)$ due to the much larger surface area of the carbon support. With this projected potential the

interferometer is very sensitive to angular offsets between the diffraction direction of the probes and the edge of the carbon support. In Figure 6.2(a-g), a 5 degree angular offset is shown to give considerable apparent phase gradient away from the carbon support that skews the interference pattern. Regardless of the asymmetry

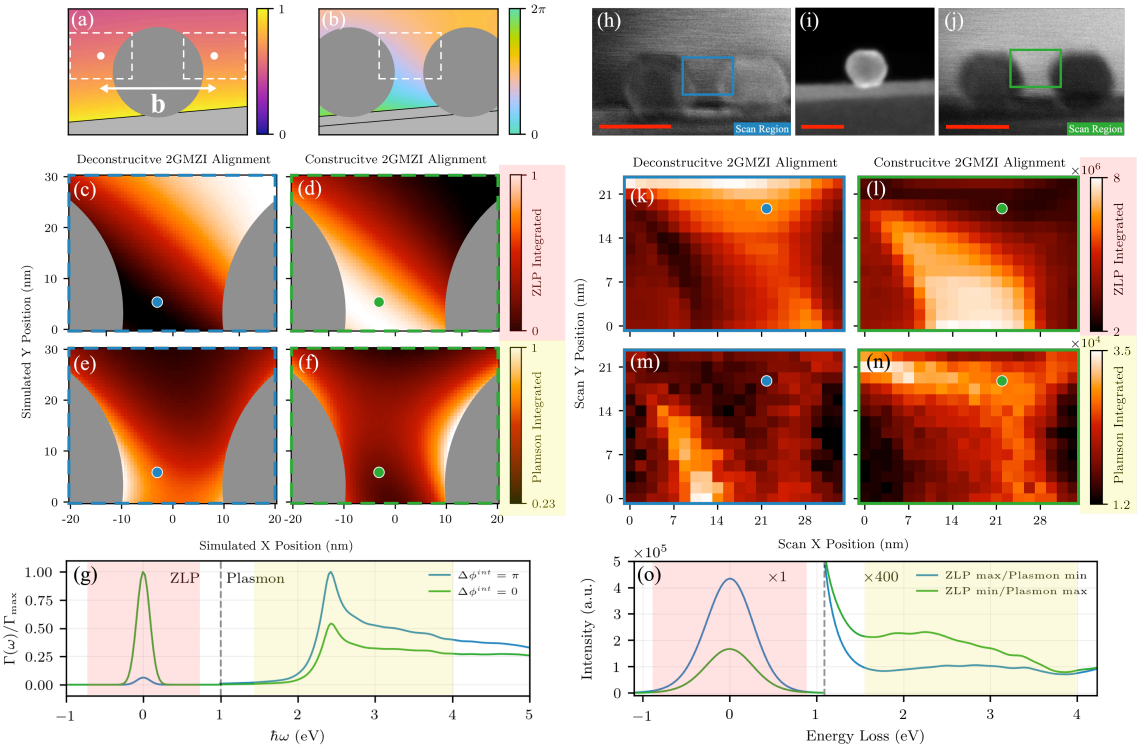

FIGURE 6.2. (a) 120×90 nm^2 region of $V_z(\mathbf{R})/V_{z;max}$ for a simulated 60 nm Au NP on a carbon support with white dashed 2 probe scan regions for probes separated by **b** with 5° angular offset. (b) $\Delta\phi_{\text{external}}$ with a the combined white dashed scan region. Simulated 40×30 nm^2 spectrum images for: (c) $\Delta\phi_{\text{internal}} = \pi$, ZLP integrated; (d) $\Delta\phi_{\text{internal}} = 0$, ZLP integrated; (e) $\Delta\phi_{\text{internal}} = \pi$, plasmon integrated; (f) $\Delta\phi_{\text{internal}} = 0$, plasmon integrated. (g) Simulated spectra at single scan point where line color corresponds to different interferometer alignments, red and yellow shaded regions are the spectrum integration regions for the ZLP and plasmon peak. (h) and (j) 2GeMZI BF images of Au NP with deconstructive and constructive interferometer alignments respectively showing spectrum image scan regions. (i) Dark field STEM image of NP. All red scale bars are 60 nm. (k-o) Experimental spectrum images and spectra with same conditions as simulations in (c-g).

in the static potential, the converse interference relation between the ZLP and the dipole plasmon scattered electrons remains over a sizable spatial region as long as the two probes are on either side of the NP and the two impact parameters are comparable, $R_{-1} \approx R_{+1}$.

6.3. Experimental Methods

The 2GeMZI is constructed in an image corrected 80-300 keV FEI Titan TEM by placing the input grating G1 in the condenser 2 aperture holder above the specimen plane and the output grating G2 in the selected area aperture holder below the specimen plane. The TEM is operated at 80 keV in STEM mode such that the probe convergence angle was tunable from 1 to 10 mrad. Both G1 and G2 were one of a 6x6 array of 30 μm diameter, 300 nm pitch binary diffraction gratings milled into a 30 nm thick Si_3N_4 free-standing membrane. These gratings were optimized to maximize intensity in the $\pm 1^{st}$ diffraction orders and minimize intensity in the 0^{th} diffraction order; approximately 30% of the total transmitted intensity is in each of the $\pm 1^{st}$ order, and no more than 6% is in any other diffraction order. An intermediate aperture after G1 (condenser 3 aperture) was used to transmit only electrons passed through a desired grating. The Lorentz lens in the image corrector was then used to project a focused image of G1 onto G2. The post-G2 projection lenses were then used to project the discrete outputs of the interferometer for selection by the entrance aperture of the EELS system. The natural energy spread of the emission source convolved with the point spread function (PSF) of the optical system of the spectrometer gives a measured full width half maximum of the ZLP of 0.8 eV. In this configuration, the scan and descan coils were used to raster the probes in the specimen plane for up to a 200×200 nm^2 scan region while maintaining the alignment

of the image of G1 with respect to G2, as well as keeping the interferometer output on the EELS entrance aperture stationary. The probe widths were 5 nm with a probe separation of 80 nm between the ± 1 diffraction orders.

Although the LPR intensity for a gold NP is more limited by the resonance frequency overlap with interband transitions compared to other noble metals such as silver [143], gold was chosen for its resistance to form oxides, offering long-term stability, availability, and ease of sample preparation. A commercial 60 nm diameter monodisperse gold NP solution was dropcast on a lacey carbon grid, allowed to air dry, and then placed in the specimen plane of the TEM. A single NP was isolated on edge of the carbon such that two electron beams could pass on either side of the NP through vacuum, Figure 6.2(i). The 2 probe scan regions were selected such that the probes were straddling NP with $\Delta\varphi \approx \pi$, Figure 6.2(h,j), then spectrum images were recorded for both deconstructive and constructive interferometer outputs, Figure 6.2(k-n).

The imaging procedure is as follows: A larger area BF scan was recorded to select a smaller region to collect a spectrum image. The spectrum image scan region was scanned while the interferometer output was collected by a 2 mm EELS entrance aperture with the spectrometer magnetic prism set to have an energy dispersion of 0.03 eV/channel on the CCD collecting the spectrum. The non-dispersing direction on CCD was binned to 1 pixel and for each scan location 20 spectra were summed with each spectrum integrated for 0.01 seconds giving a total integration time of 0.5 seconds per scan location.

Once the spectrum images were recorded they were post-processed in two steps. First, each spectrum was smoothed with a 4 pixel standard deviation Gaussian convolution to remove high frequency noise. Second, 4 iterations of the 1D

Richardson-Lucy deconvolution algorithm were run using the HyperSpy Python library on each spectrum. A vacuum collected spectrum that was identically smoothed was used as the deconvolution kernel to partially remove the PSF of the spectrometer. This significantly narrows the tails of the zero loss peak (ZLP), effectively removing the background in the 1-3 eV region where the plasmon signals of interest are [144]. Finally, the post-processed spectra were integrated over range (-1,1) eV for the ZLP and over the range (1.5,4) eV for the plasmon peaks, shown in Figure 6.2(o).

6.4. Discussion of results

The side-by-side comparison of the simulated and experimental spectrum images in Figure 6.2 shows an excellent qualitative agreement for the converse dipole interference relationship between the ZLP and plasmon peaks over a spatially varying electrostatic potential. To provide a more quantitative analysis, we assign a relative probe phase to each pixel with probes passing through vacuum in Figure 6.2(k,l) by normalizing the ZLP intensity, then we find the relative phase by inversion of $I_{ZLP} \propto \cos(\Delta\phi/2)^2$. The normalized integrated ZLP and plasmon intensities of each pixel were plotted as a function of the assigned relative probe phase (Fig. 6.3). For clarity, we also show the mean values binned by every $\pi/12$ relative phase interval along with the theoretically predicted values for $\Delta\varphi = \pi$. To account for our ignorance of whether or not the minimum and maximum ZLP intensities correspond to the exact actual $\Delta\phi = \pi$ and $\Delta\phi = 0$ points we give a $\pi/12$ systematic error to the standard deviation of the binned values added in quadrature. Since we definitionally assigned the relative phase to the integrated intensity of the ZLP peak, we didn't

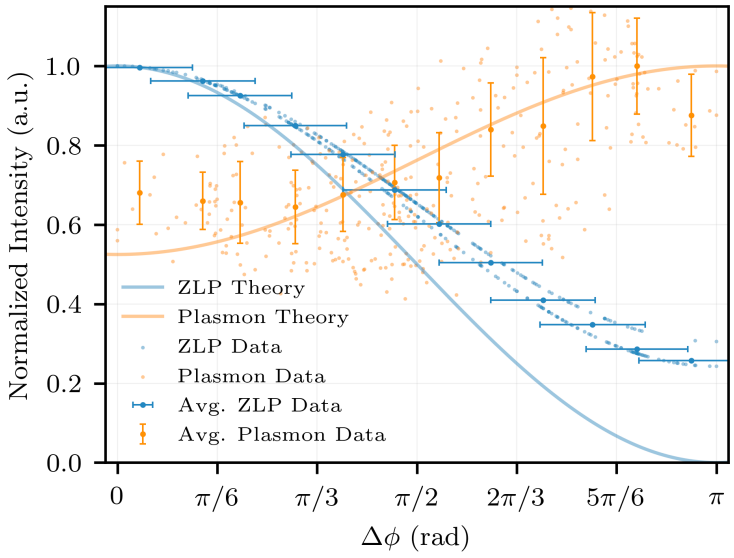

FIGURE 6.3. Measured and theoretical ZLP and plasmon integrated intensities as function of the total relative probe phase fit to each spectrum image pixel from Figure 6.2(k-n).

give an error for this integrated intensity. The error given for the mean integrated plasmon intensities is the standard deviation of the integrated intensities for each binned region and the phase error is assumed to be the same as the mean ZLP data. Deviation of the measured ZLP intensity compared to the theoretical prediction is well understood by the small, but non-zero contributions of the higher order probes from G1 causing a loss of fringe visibility. This does not have as large of an effect the visibility of the plasmon interference because the higher order probes are further away from the NP than the main ± 1 probes and the plasmon loss probability is exponentially suppressed for large impact parameters, i.e. $K_m(x) \sim e^{-x}\sqrt{\pi/2x}$ for large x. We made additional measurements on a separate gold NP where an angular offset between the probe separation direction and the carbon support were in the opposite direction. The spatially varying relative phase is consistent with the

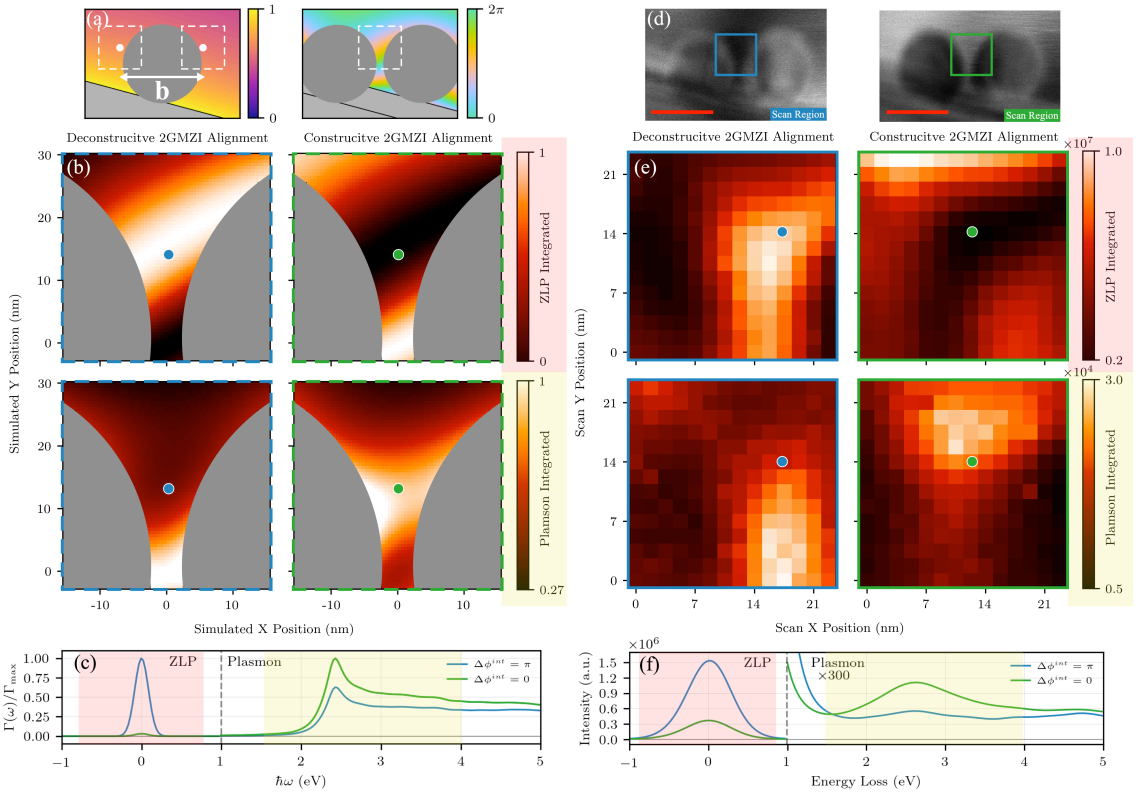

FIGURE 6.4. (a) Left, simulated static projected potential $V_z(\mathbf{R})/V_{z;max}$ in a 120×90 nm^2 region; right, 2 probe relative external phase due to simulated projected potential, $\Delta\phi^{ext}$, for a metallic NP on a carbon support. (b) Simulated spatially varying interference for: top ZLP integrated, and bottom plasmon integrated spectrum images. Blue outlines correspond to deconstructive interferometer output, $\Delta\phi^{int} = \pi$, and green outlines to constructive interferometer output, $\Delta\phi^{int} = 0$. Red scale bars are 70 nm. (c) Simulated EELS spectra from location of colored spot corresponding to color of the plot line. (d) 2GeMZI bright field images of 35 nm radius gold NP for a deconstructive and constructive interferometer alignments showing spectrum image scan regions on the left and right respectively. (e,f) Experimental data with same conditions as simulated data in (b,c).

changed orientation and still exhibits the expected converse intensity relation between the ZLP and dipole plasmon peak, Figure 6.4.

Similar conditional interference relations between the the ZLP and the higher order modes in the multipole expansion dependent on the geometry and symmetry of the mode spatial distribution and probe position exist, but the multipole plasmon peaks for a spherical gold NP of this size are not spectrally resolvable; the peak widths are much larger than the peak spacing in the loss spectrum. However, multiple plasmon mode peaks can be resolved with more complicated NP geometries [145], chains of spherical NPs [146], or by changing the spherical NP material [147]. These relations could be explored with this apparatus, but may require constructing another 2GeMZI in a monochromated TEM with an energy resolution below 100 meV. Another potential application for the 2GeMZI is to demonstrate entanglement between the electron and the NP plasmon or the photons radiated from the plasmon [148]. Incorporation of a cathodoluminescence collection system with a 2GeMZI could provide information on the correlation between the phase coherent superpositions of scattered electrons to the radiated light from the dipole plasmon [149, 150]. Alternatively, this 2GeMZI could serve as an indirect way to measure the transfer of orbital angular momentum [18, 151, 152]. Finally, we note that inelastic electron interference in the 2GeMZI can be used to probe many different condensed matter quasiparticle excitations, not just plasmons [13].

6.5. Chapter Summary

We have demonstrated phase sensitive interference between coherent superpositions of inelastically scattered electrons within a two-probe 2GeMZI from plasmonic excitations of a single gold NP. Supplement to the additional applications in probing

nanoplasmonic systems, the flexibility, scanning capabilities, and operation in a conventional TEM of this technique provides an exciting platform for probing quantum mechanics at the nanoscale and application of control over the transverse electron wavefunction. Further development of the techniques presented in this letter could lead to tests of quantum complementarity for electrons [153], exploration of decoherence theory [130], and, as a STEM technique, has the inherent potential for including multimodal functionality with control over multiple degrees freedom for the electron wavefunction [25].

CHAPTER VII

FUTURE DIRECTIONS AND CONCLUSION

Notes for Ch. VI:

This chapter contains unpublished material.

As noted in the previous chapter, there is an abundance of opportunities for future experiments with the 2GeMZI. In this chapter we outline two possible future experiments that the 2GeMZI could enable, one that could be immediately performed, and a second that could be performed after further experimental development. Finally, we conclude with a brief dissertation summary and a final outlook for the future research enabled by the body of this work.

7.1. Future Directions

7.1.1. Next Experiment: Plasmonic Mode Selection

Before exploring the larger parameter space of different nanoparticle geometries to find ideal situations of spatially and spectrally separated plasmon modes, we can restrict the search to spherical nanoparticles with different materials. We simulate the two-probe 2GeMZI EELS probabilities for gold, silver, aluminum, and platinum spherical nanoparticles with different radii (Fig. 7.1). Considering the $\Delta E \approx 0.7$ eV energy resolution of the current 2GeMZI, we see that aluminum spherical nanoparticles with radii $a < 10$ nm have their dipole and quadrupole modes spectrally resolvable. Multipole resolved EELS probabilities for an $a = 7$ nm aluminum nanoparticle are shown in Figure 7.2 displaying not only the

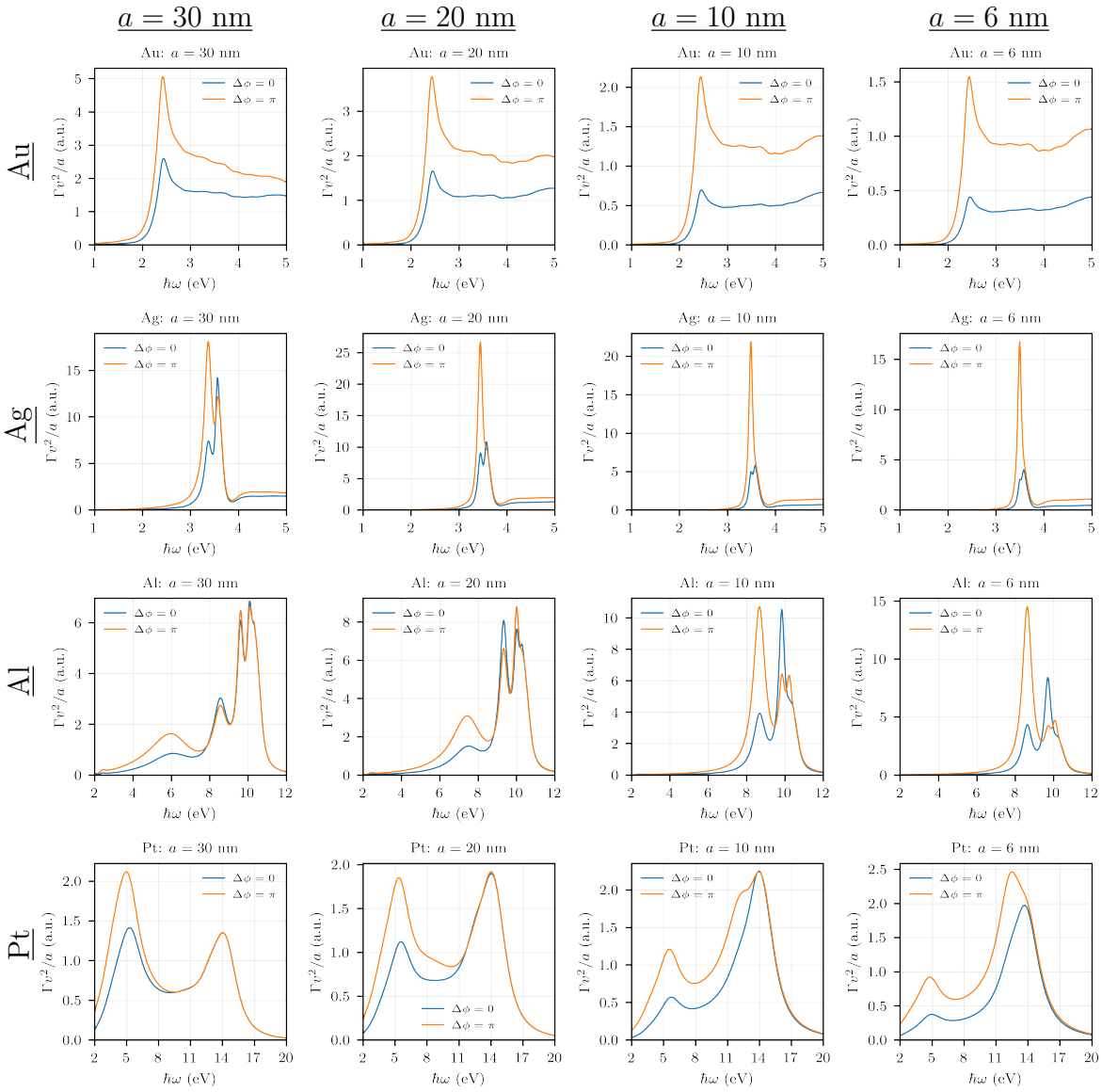

FIGURE 7.1. Simulated two-probe 2GeMZI EELS spectra of different material spherical nanoparticles with varying radii for constructive and deconstructive interferometer outputs. Different materials by row, top to bottom: gold, silver, aluminum, and platinum. Different nanoparticle radii by column, left to right: $a = 30$ nm, $a = 20$ nm, $a = 10$ nm, $a = 6$ nm.

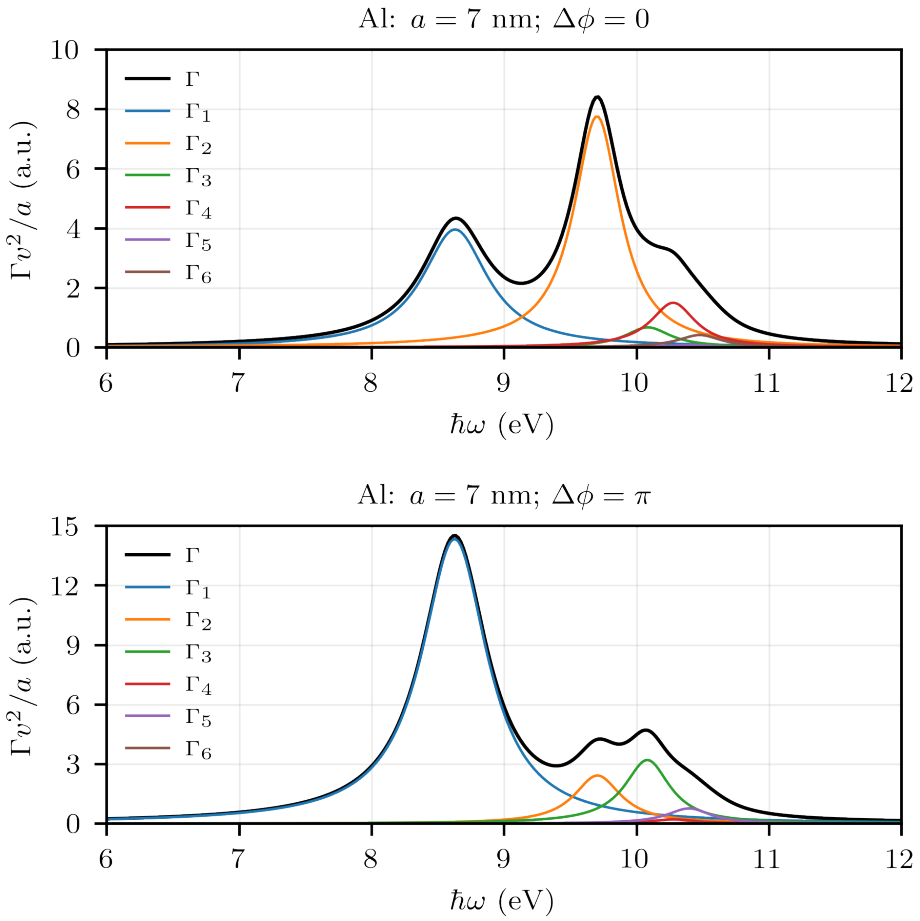

FIGURE 7.2. The total and $l = 1 - 6$ multipole components of two-probe 2GeMZI EELS spectrum for an $a = 7$ nm aluminum spherical nanoparticle for a (top) constructive and (bottom) deconstructive interferometer output. Γ and Γ_l are defined in Equation 5.13.

converse relation of the dipole peak with the interferometer alignment, but also the resolvable converse relation between the even and odd multipole components.

With the availability of aluminum nanopowders allowing for the ease of sample preparation, a single aluminum nanoparticle could be used in the current 2GeMZI apparatus to measure spatial spectrum images for multiple multipole components of the EELS spectrum like in Figures 5.4 and 5.5.

7.1.2. Future Experiment: Free Electron Plasmonic Quantum Eraser

Scully, Englert, and Walther [153] outlined tests of quantum complementarity where momentum space interference between a superposition of a quantum particle's spatial locations (i.e. a double slit) is collapsed upon measurement of an entangled system when the result of the measurement gives 'which-path' information. Specifically, quantum eraser and delayed choice experiments exploit control of the measurement parameters to destroy and revive interference as a function of parameter tuning. Variants of these experiments have been performed with atoms [154], photons [155], and condensed matter quasi-particles [156]. The inelastic interference we, and others [137], have demonstrated suggests that it should possible to entangle free electrons with a plasmonic system. However, methods for control of the which-path information has not been demonstrated, although experiments to measure correlation with FEs with entangled systems have been recently proposed [148]. Here we propose a quantum eraser experiment to control the interference of inelastically scattered electrons by measuring the polarization state of the radiated photons.

Consider the portion of the electron wavefunction that was inelastically scattered by the dipole plasmon. In the far field, the the spatial superposition of electrons inelastically scattered from a dipole plasmon form interference fringes that can be spectrally filtered from the elastic counterpart (Fig. 7.3). The probability of electromagnetic radiation emission from a NP plasmon (neglecting the magnetic component)

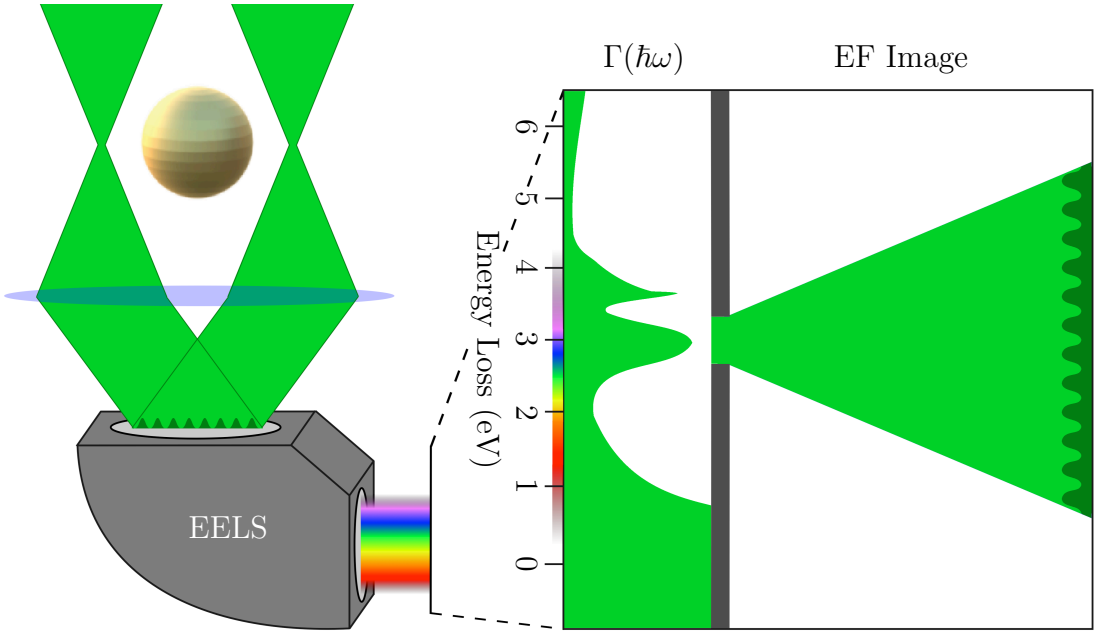

FIGURE 7.3. Diagram of energy filtered interference fringes with an EELS spectrometer. Symbolic EELS spectrum with dipole plasmon peak at 3 eV spectrally resolved from the ZLP at 0 eV and the higher order multipole peaks >3.5 eV. A slit can filter by energy only letting the dipole plasmon peak to pass and form an image of the interference fringes.

is given by

$$\begin{aligned}\Gamma^{\{\mathrm{rad}\}}(\omega,\mathbf{R}_0) &= \frac{e^2}{\hbar\omega c}\sum_{l=1}^{\infty}\sum_{m=-l}^{l} K_m\left(q_\gamma R_0\right)^2 C_{lm}^E |t_l^E(\omega)|^2 \\ &= \sum_{l=1}^{\infty}\Gamma_l^{\{\mathrm{rad}\}}(\omega,\mathbf{R}_0)\end{aligned} \tag{7.1}$$

[134]. We will only consider $l = 1$ dipole of an aluminum NP that is spectrally resolved from the rest of the multipole peaks. A cathodoluminescence light collection system can be used to collect the emitted photons. After spectrally filtering the dipole peak in the emission spectrum, a polarizing beamsplitter can resolve this radiation into two orthogonally polarized spatial photon maps for the dipole plasmon emission for every electron probe scan position [149]. A half wave plate (HWP) can be used

to rotate the detected photon's polarization state with respect to the D_H and D_V detectors (Fig. 7.4).

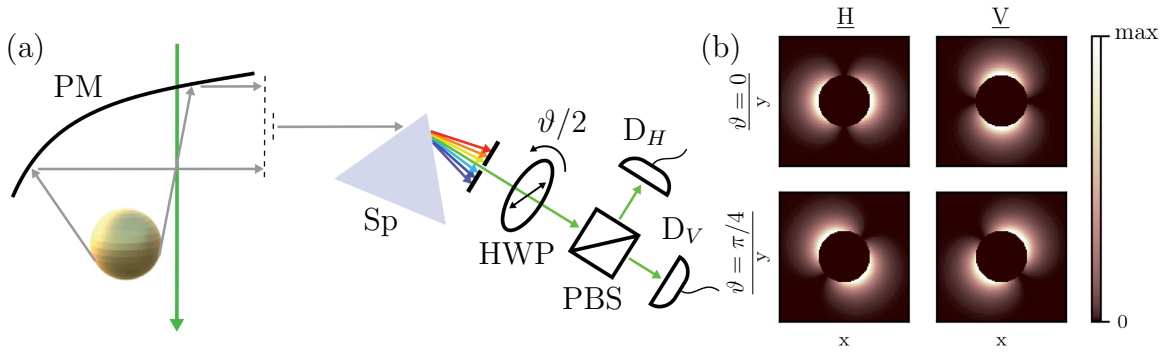

FIGURE 7.4. (a) Diagram of cathodoluminescence light collection system consisting of a parabolic mirror (PM), spectrometer (Sp), half wave plate (HWP) for rotating the polarization by the angle ϑ, polarizing beamsplitter (PBS), and two detectors D_H and D_V for detecting H and V polarizations respectively. (b) Top row, simulated H and V photon maps outside of the NP for $\vartheta = 0$. Bottom row, same but for $\vartheta = \pi/4$.

A single electron probe at the position $\mathbf{R}_0 = (R_0\cos(\varphi_0), R_0\sin(\varphi_0))$, with impact parameter R_0 and azimuthal angle φ_0 that are similarly defined in Figure 5.1, is entangled with the emitted photons and can be written as the composite wavefunction in detector polarization basis $|H\rangle$ and $|V\rangle$

$$|\psi(\vartheta)\rangle = |\psi_0^s\rangle\,(\cos(\varphi_0+\vartheta)\,|H\rangle + \sin(\varphi_0+\vartheta)\,|V\rangle), \tag{7.2}$$

where $\psi_0^s(\mathbf{R}_0) = \langle \mathbf{R}_0|\psi_0^s\rangle$ is the electron wavefunction scattered by dipole plasmon.

Now we consider a two-probe incident wavefunction $\psi(\mathbf{R}) = \psi_+(\mathbf{R}_+) + e^{i\Delta\phi}\psi_-(\mathbf{R}_-)$. With equal impact parameters $R_+ = R_-$ and incidence at right azimuthal angles, $\varphi_+ = 0$ and $\varphi_- = \pi/2$, the total scattered state becomes entangled

with the polarization of photons emitted from the dipole plasmon

$$|\psi(0)\rangle = \left|\psi_+^s\right\rangle |H\rangle + e^{i\Delta\phi}\left|\psi_-^s\right\rangle |V\rangle\,. \tag{7.3}$$

Here, a measurement of the radiated photon polarization corresponds to a which-path measurement. If the photon is measured to have H or V polarization, the probability of measuring the scattered electron, $P_{H/V}(\vartheta) = |\,\langle H/V|\psi(\vartheta)\rangle\,|^2$, is

$$P_{H/V}(0) = \left\langle\psi_\pm^s|\psi_\pm^s\right\rangle. \tag{7.4}$$

Thus, the energy-filtered interference fringes depicted in Figure 7.3 will disappear upon measurement of the radiated photon's polarization state. This which-path information can be erased by rotating the polarization detection basis. With a $\vartheta = \pi/4$ rotation of the HWP, the scattered electron wavefunction becomes

$$\begin{aligned}|\psi(\pi/4)\rangle &= \frac{1}{\sqrt{2}}\left|\psi_+^s\right\rangle(|H\rangle + |V\rangle) + \frac{e^{i\Delta\phi}}{\sqrt{2}}\left|\psi_-^s\right\rangle(-|H\rangle + |V\rangle)\\ &= \frac{1}{\sqrt{2}}\left(\left|\psi_+^s\right\rangle - e^{i\Delta\phi}\left|\psi_-^s\right\rangle\right)|H\rangle + \frac{1}{\sqrt{2}}\left(\left|\psi_+^s\right\rangle + e^{i\Delta\phi}\left|\psi_-^s\right\rangle\right)|V\rangle\,.\end{aligned} \tag{7.5}$$

Then interference fringes of the scattered electron remains after any polarization measurement

$$P_{H/V}(\pi/4) = \frac{1}{2}\left(\left\langle\psi_+^s|\psi_+^s\right\rangle + \left\langle\psi_-^s|\psi_-^s\right\rangle \mp 2\mathrm{Re}\left\{e^{i\Delta\phi}\left\langle\psi_+^s|\psi_-^s\right\rangle\right\}\right). \tag{7.6}$$

With this, we see that by selecting the measurement basis of the photon polarization and using coincidence counting to ensure correlation of the entangled state, we can create or destroy the which-path information for the passing electron superposition.

This will result in a loss of fringe visibility in the energy-filtered electron interference, as is expected for the quantum eraser. With the slow velocity of the electrons $\sim 0.5c$ and the ease of allowing for delayed photon detection, a delayed choice extension of the experiment could also be implemented.

7.2. Conclusion

In this dissertation I have described original research in holographic beam shaping and grating-based inelastic interferometry with free electrons. We have demonstrated the efficient diffraction and shaping of a free electron's wavefront via off-axis material holograms by developing the FIB GAE nanofabrication process. With FIB GAE fabricated binary gratings we have constructed a novel, scanning, phase-tunable 2GeMZI in a TEM capable of quantitative nanoscale phase imaging and mapping of electrostatic potentials. We use the 2GeMZI to demonstrate interference between a coherent spatial superposition of electrons inelastically scattered from the dipole plasmon of a single gold nanoparticle. The multiple prospects for future quantum and nanoplasmonic experiments the 2GeMZI provides gives an exciting outlook for the breadth of research that can be enabled by free electron Mach-Zehnder interferometry.

APPENDIX

TRANSVERSE BEAM SHAPING FORMALISM

A.1. The transmitted wave as a sum of diffraction orders

Inserting Equation (3.6) into Equation (3.2) gives

$$\psi(\mathbf{R}) = e^{i\widetilde{\Phi}t_0} \exp\left(-i\widetilde{\Phi}dZ(\mathbf{R}) \sum_{n=-\infty}^{\infty} |c_n(\mathbf{R})|\alpha_n(\mathbf{R}) \left(\Theta(\mathbf{R})e^{i\mathbf{k}_0\cdot\mathbf{R}}\right)^n\right). \tag{A.1}$$

By definition, the Fourier coefficients have the properties $|c_{-n}(\mathbf{R})| = |c_n(\mathbf{R})|$, $\alpha_{-n}(\mathbf{R}) = \alpha_n(\mathbf{R})^{-1}$ and $\alpha_0(\mathbf{R}) = 1$. With this, Equation (A.1) can be rewritten as

$$\psi(\mathbf{R}) = e^{i\widetilde{\Phi}(t_0 - c_0(\mathbf{R})dZ(\mathbf{R}))} \prod_{n=1}^{\infty} \exp\Bigg(- i\widetilde{\Phi}|c_n(\mathbf{R})|dZ(\mathbf{R})\Bigg(\alpha_n(\mathbf{R}) \left(\Theta(\mathbf{R})e^{i\mathbf{k}_0\cdot\mathbf{R}}\right)^n + \left[\alpha_n(\mathbf{R}) \left(\Theta(\mathbf{R})e^{i\mathbf{k}_0\cdot\mathbf{R}}\right)^n\right]^{-1}\Bigg)\Bigg). \tag{A.2}$$

Note now that there is a well-known generating relation for the Bessel functions, usually written as

$$\exp\left(\frac{\rho}{2}\left(\chi + \chi^{-1}\right)\right) = \sum_{m=-\infty}^{\infty} \chi^m I_m(\rho), \tag{A.3}$$

where $I_m(\rho)$ is the m^{th} order modified Bessel function of the first kind [157], and when applied to Equation (A.2) gives

$$\psi(\mathbf{R}) = e^{i\widetilde{\Phi}(t_0 - c_0(\mathbf{R})dZ(\mathbf{R}))} \prod_{n=1}^{\infty} \sum_{m=-\infty}^{\infty} \alpha_n(\mathbf{R})^m \left(\Theta(\mathbf{R}) e^{i\mathbf{k}_0\cdot\mathbf{R}}\right)^{nm} I_m\big(-2i\widetilde{\Phi}|c_n(\mathbf{R})|dZ(\mathbf{R})\big). \tag{A.4}$$

To make any useful progress with Equation (A.4) we need to turn the product of the sums into a sum of the products. For an arbitrary function B, a general product of sums can be rewritten as

$$\prod_{n\in\mathbb{P}} \sum_{m\in\mathbb{S}} B(n,m) = \sum_{s\in E} \prod_{n\in\mathbb{P}} B(n, s(n)) \tag{A.5}$$

where $\mathbb{P}$ is the domain of the product, $\mathbb{S}$ is the domain of the sum, and $E = \{s \,|\, s : \mathbb{P} \to \mathbb{S}\}$ is the set of all maps from the initial product domain to the initial sum domain. Further explanation of this operation can be found in Appendix A.3. Turning Equation (A.4) into a sum of products yields

$$\begin{aligned}
\psi(\mathbf{R}) &= e^{i\widetilde{\Phi}(t_0 - c_0(\mathbf{R})dZ(\mathbf{R}))} \sum_{s\in E} \prod_{n=1}^{\infty} \alpha_n(\mathbf{R})^{s(n)} \left(\Theta(\mathbf{R}) e^{i\mathbf{k}_0\cdot\mathbf{R}}\right)^{ns(n)} I_{s(n)}\big(-2i\widetilde{\Phi}|c_n(\mathbf{R})|dZ(\mathbf{R})\big) \\
&= e^{i\widetilde{\Phi}(t_0 - c_0(\mathbf{R})dZ(\mathbf{R}))} \sum_{s\in E} \left(\Theta(\mathbf{R}) e^{i\mathbf{k}_0\cdot\mathbf{R}}\right)^{\sum_{k=1}^{\infty} ks(k)} \prod_{n=1}^{\infty} \alpha_n(\mathbf{R})^{s(n)} I_{s(n)}\big(-2i\widetilde{\Phi}|c_n(\mathbf{R})|dZ(\mathbf{R})\big).
\end{aligned} \tag{A.6}$$

We now define a function $g : s \in E \to \mathbb{Z}$ that we will call the *order* of a map s as

$$g(s) = \sum_{k=1}^{\infty} ks(k). \tag{A.7}$$

With this definition we can define the subsets $E_m \subset E$ as $E_m = \{s \in E \,|\, g(s) = m\}$, i.e., group all the maps s which give the same integer *order* under the function g. Applying these conventions, Equation (A.6) can be recast as

$$\psi(\mathbf{R}) = e^{i\widetilde{\Phi}(t_0 - c_0(\mathbf{R})dZ(\mathbf{R}))} \sum_{m=-\infty}^{\infty} \big(\Theta(\mathbf{R}) e^{i\mathbf{k}_0 \cdot \mathbf{R}}\big)^m \sum_{s \in E_m} \prod_{n=1}^{\infty} \alpha_n(\mathbf{R})^{s(n)} I_{s(n)}\big(-2i\widetilde{\Phi}|c_n(\mathbf{R})|dZ(\mathbf{R})\big). \tag{A.8}$$

Now we note that the first sum in Equation (A.8) is a sum of diffraction orders and, when compared to Equation (3.4), gives

$$A_m Z_m(\mathbf{R})\Theta_m(\mathbf{R}) = e^{i\widetilde{\Phi}(t_0 - c_0(\mathbf{R})dZ(\mathbf{R}))}\Theta(\mathbf{R})^m \sum_{s \in E_m} \prod_{n=1}^{\infty} \alpha_n(\mathbf{R})^{s(n)} I_{s(n)}\big(-2i\widetilde{\Phi}|c_n(\mathbf{R})|dZ(\mathbf{R})\big). \tag{A.9}$$

A.2. Reconstruction in the first diffraction order

Equation (A.9) can be used to calculate a hologram pattern that gives a desired output beam in the first diffraction order

$$A_1 Z_1(\mathbf{R})\Theta_1(\mathbf{R}) = e^{i\widetilde{\Phi}(t_0 - c_0(\mathbf{R})dZ(\mathbf{R}))}\Theta(\mathbf{R}) \sum_{s \in E_1} \prod_{n=1}^{\infty} \alpha_n(\mathbf{R})^{s(n)} I_{s(n)}\big(-2i\widetilde{\Phi}|c_n(\mathbf{R})|dZ(\mathbf{R})\big). \tag{A.10}$$

The diffraction efficiency (relative to the incident intensity) can be easily calculated by integrating over the hologram aperture. If the envelope function $Z(\mathbf{R})$ is unity within the aperture and zero elsewhere, the diffraction efficiency is simply $|\psi_1|^2$. The value of $|\psi_1|^2$ increases monotonically with the groove depth d until maximum diffraction efficiency is reached at $d_{\max}$, the maximum invertable groove depth. $d_{\max}$ is

different for every groove profile. It can be found recursively, or it can be estimated by finding the first 1st order diffraction efficiency maximum for the 1-dimensional infinite grating with the given groove profile, i.e., the smallest non-zero valued solution to

$$\frac{i\widetilde{\Phi}|\mathbf{k}_0|}{2\pi}\int_0^{\frac{2\pi}{|\mathbf{k}_0|}} dx\, \exp\big(i(\widetilde{\Phi}t(x,d_{\max})-|\mathbf{k}_0|x)\big)\left[\frac{\partial}{\partial h}t(x,d)\right]_{d=d_{\max}}=0, \tag{A.11}$$

where $t(x,d)$ is the 1-dimensional analog of Equation (3.5) with a unit envelope function [31]. If $d > d_{\max}$, $Z_1(\mathbf{R})\Theta_1(\mathbf{R})$ is not guaranteed to be produced exactly. Provided that $d \leq d_{\max}$, we can set

$$A_1 = \left| e^{i\widetilde{\Phi}(t_0-\langle c_0\rangle_{\mathbf{R}}d)} \sum_{s\in E_1}\prod_{n=1}^{\infty} I_{s(n)}\big(-2i\widetilde{\Phi}|\langle c_n\rangle_{\mathbf{R}}|d\big)\right|, \tag{A.12}$$

where $\langle\cdots\rangle_{\mathbf{R}}$ is an average over $\mathbf{R}$. Thus, we find

$$Z_1(\mathbf{R}) = \left| e^{i\widetilde{\Phi}(t_0-c_0(\mathbf{R})dZ(\mathbf{R}))} \sum_{s\in E_1}\prod_{n=1}^{\infty} \alpha_n(\mathbf{R})^{s(n)} I_{s(n)}\big(-2i\widetilde{\Phi}|c_n(\mathbf{R})|dZ(\mathbf{R})\big)\right| /A_1 \tag{A.13}$$

and

$$\Theta(\mathbf{R}) = \Theta_1(\mathbf{R})\exp\left(-i\arg\left[e^{i\widetilde{\Phi}(t_0-c_0(\mathbf{R})dZ(\mathbf{R}))}\sum_{s\in E_1}\prod_{n=1}^{\infty}\alpha_n(\mathbf{R})^{s(n)} I_{s(n)}\big(-2i\widetilde{\Phi}|c_n(\mathbf{R})|dZ(\mathbf{R})\big)\right]\right). \tag{A.14}$$

Equation (A.13) can be numerically inverted to find $Z(\mathbf{R})$, which can then be used to find $\Theta(\mathbf{R})$. This is an exact solution when every map $s \in E_1$ is known. However, in general there are an infinite number of maps s. If we are to practically use this formalism we must rank each map by the magnitude of its contribution and select the highest contributors to use, truncating the sum over the set E_1. We define

a ranked contribution

$$C_j = \int_0^{d_0} dd' \left| e^{-i\widetilde{\Phi}\langle c_0\rangle_{\mathbf{R}} d'} \prod_{n=1}^{N} I_{s_j(n)}\big(-2i\widetilde{\Phi}|\langle c_n\rangle_{\mathbf{R}}|d'\big) \right|, \tag{A.15}$$

where $C_j > C_{j+1}$ gives the rank j to each map s_j, $d_0 \leq d_{\max}$ is the groove depth used in the search, and N is a sufficiently large number. To help find a majority of the highest ranked maps s_j, we note that $|I_k(ix)| \propto x^k$ for small x, and $c_n \to 0$ as $n \to \infty$; for large n, $|I_0(-2i\widetilde{\Phi}|c_n|d)| \approx 1$ and $|I_k(-2i\widetilde{\Phi}|c_n|d)| \approx 0$ for all $|k| > 0$. With this in mind we can set limits to the search parameters $|s(n)| \leq p$ and $n \leq q$, setting all $s(n) = 0$ for $n > q$. It must be stressed that the number of maps in the search increases as $(2p+1)^q$, the order $g(s)$ must be computed for each map, and the 1^{st} order maps must be sorted by their ranked contribution C_j. This may be computationally expensive for large parameter limits p and q, but for a given material $\widetilde{\Phi}$, and groove profile $\{c_n\}$, the same set of maps found in the search $\{s_j\}$ can be used to make the hologram groove profile from $Z(\mathbf{R})$ and $\Theta(\mathbf{R})$ corresponding to any desired function to reconstruct $Z_1(\mathbf{R})\Theta_1(\mathbf{R})$. An example Python script implementation of this process can be found here [158].

A.3. Product of sums to a sum of products

Consider the product of sums

$$
\begin{aligned}
F &= \prod_{n=1}^{3} \sum_{m=-1}^{1} B(n,m) \\
&= B(1,-1)B(2,-1)B(3,-1) + B(1,-1)B(2,-1)B(3,0) + B(1,-1)B(2,-1)B(3,1) \\
&\quad + B(1,-1)B(2,0)B(3,-1) + B(1,-1)B(2,0)B(3,0) + B(1,-1)B(2,0)B(3,1) \\
&\quad + B(1,-1)B(2,1)B(3,-1) + B(1,-1)B(2,1)B(3,0) + B(1,-1)B(2,1)B(3,1) \\
&\quad + B(1,0)B(2,-1)B(3,-1) + B(1,0)B(2,-1)B(3,0) + B(1,0)B(2,-1)B(3,1) \\
&\quad + B(1,0)B(2,0)B(3,-1) + B(1,0)B(2,0)B(3,0) + B(1,0)B(2,0)B(3,1) \\
&\quad + B(1,0)B(2,1)B(3,-1) + B(1,0)B(2,1)B(3,0) + B(1,0)B(2,1)B(3,1) \\
&\quad + B(1,1)B(2,-1)B(3,-1) + B(1,1)B(2,-1)B(3,0) + B(1,1)B(2,-1)B(3,1) \\
&\quad + B(1,1)B(2,0)B(3,-1) + B(1,1)B(2,0)B(3,0) + B(1,1)B(2,0)B(3,1) \\
&\quad + B(1,1)B(2,1)B(3,-1) + B(1,1)B(2,1)B(3,0) + B(1,1)B(2,1)B(3,1).
\end{aligned}
\tag{A.16}
$$

Each term in the sum above is of the form $B(1,a)B(2,b)B(3,c)$, where a, b, and c can be any number in the domain of the sum $a,b,c \in \mathbb{S} = \{-1,0,1\}$. Furthermore, each term represents a unique way to map the domain of the product $\mathbb{P} = \{1,2,3\}$ to the domain of the sum $\mathbb{S} = \{-1,0,1\}$. We can define the set of all these maps $E = \{s \mid s : \mathbb{P} \to \mathbb{S}\}$, clearly for this case there are 27 such maps each of which can be seen in Table A.1.

n	$s^1(n)$	$s^2(n)$	$s^3(n)$	$s^4(n)$	$s^5(n)$	$s^6(n)$	$s^7(n)$	$s^8(n)$	$s^9(n)$
1	-1	-1	-1	-1	-1	-1	-1	-1	-1
2	-1	-1	-1	0	0	0	1	1	1
3	-1	0	1	-1	0	1	-1	0	1
n	$s^{10}(n)$	$s^{11}(n)$	$s^{12}(n)$	$s^{13}(n)$	$s^{14}(n)$	$s^{15}(n)$	$s^{16}(n)$	$s^{17}(n)$	$s^{18}(n)$
1	0	0	0	0	0	0	0	0	0
2	-1	-1	-1	0	0	0	1	1	1
3	-1	0	1	-1	0	1	-1	0	1
n	$s^{19}(n)$	$s^{20}(n)$	$s^{21}(n)$	$s^{22}(n)$	$s^{23}(n)$	$s^{24}(n)$	$s^{25}(n)$	$s^{26}(n)$	$s^{27}(n)$
1	1	1	1	1	1	1	1	1	1
2	-1	-1	-1	0	0	0	1	1	1
3	-1	0	1	-1	0	1	-1	0	1

TABLE A.1. All the maps E for $\mathbb{P} = \{1, 2, 3\}$ and $\mathbb{S} = \{-1, 0, 1\}$. Note that we use a superscript here $s^k(n)$ instead of the subscript $s_j(n)$ as used in Equation A.15. This is because k is just a counting index and does not correspond to a rank from its contribution, as with the index j.

Consequently, we see that

$$\begin{aligned} F &= \prod_{n\in\mathbb{P}} \sum_{m\in\mathbb{S}} B(n,m) \\ &= \sum_{s\in E} \prod_{n\in\mathbb{P}} B(n, s(n)). \end{aligned} \tag{A.17}$$

This is equally valid when $\mathbb{P} = \mathbb{Z}^+$ and $\mathbb{S} = \mathbb{Z}$.

A.4. Map search for blazed groove profiles

The search stated in the main body of paper was performed for a depth of $d_0 = 60$ nm and yielded the set of *order* $g(s) = 1$ maps whose highest 10 contributors and their normalized contributions can be found in Table A.2.

We numerically invert Equation (A.13) for a linear input of Z, Fig. A.1. The function $Z(\mathbf{R})$ is interpolated from the envelope function of the desired target wavefunction $Z_1(\mathbf{R})$. It should be noted that C_j is dependent on h_0, meaning that

n:	1	2	3	4	5	6	7	8	$\cdots$	C_j/C_1
$s_1(n)$:	1	0	0	0	0	0	0	0	$\cdots$	1.000
$s_2(n)$:	-1	1	0	0	0	0	0	0	$\cdots$	0.265
$s_3(n)$:	0	-1	1	0	0	0	0	0	$\cdots$	0.084
$s_4(n)$:	-2	0	1	0	0	0	0	0	$\cdots$	0.074
$s_5(n)$:	0	0	-1	1	0	0	0	0	$\cdots$	0.041
$s_6(n)$:	-1	-1	0	1	0	0	0	0	$\cdots$	0.034
$s_7(n)$:	3	-1	0	0	0	0	0	0	$\cdots$	0.033
$s_8(n)$:	0	0	0	-1	1	0	0	0	$\cdots$	0.024
$s_9(n)$:	2	1	-1	0	0	0	0	0	$\cdots$	0.019
$s_{10}(n)$:	-1	0	-1	0	1	0	0	0	$\cdots$	0.018
$\vdots$	$\vdots$	$\vdots$	$\vdots$	$\vdots$	$\vdots$	$\vdots$	$\vdots$	$\vdots$	$\ddots$	$\vdots$

TABLE A.2. The 10 leading components to the first diffracted order of a blazed hologram for $h_0 = 60$ nm. All terms after $n = 8$ shown here have $s_j(n) = 0$. Also note that $g(s) = 1$ for each map, signifying that it does contribute to the first diffraction order.

the set of $\{s_j\}$ can change depending on what value d_0 is used in the search. However, for the blazed profile case with $\widetilde{\Phi} \approx 0.008i - \pi/29$ nm^{-1}, if $10 \leq d_0 \leq 60$ is used to search for the maps $\{s_j\}$, the inverted curves, an example of which are found in Figure A.1(a), are no more than 0.15% different from the curve in Figure A.1(a) up the groove depth used in the search for maps $\{s_j\}$, Fig. A.1(b). This implies that it is sufficient to use one set of maps for all $d < d_0$ and the best choice is $d_0 \lessapprox d_{\max}$. Figure A.1(c) can be used to explain why this is the case. The smaller the value of d, the less terms are needed for an accurate approximation. More maps have significant contributions when d_0 is close to $d_{\max}$ than when d_0 is small. A set of maps created from a large d_0 is more likely to contain large contributor maps of the smaller d_0 sets than vice-versa.

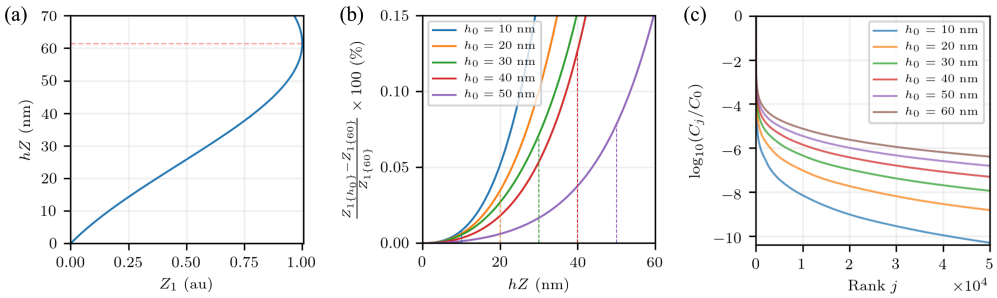

FIGURE A.1. (a) Numerical inversion of Equation (A.13) for a blazed hologram with $d_0 = 60$ nm using the first 5000 highest contributing maps. Red dashed line is the maximum invertable groove depth $d_{\max} \approx 61.5$ nm. (b) The relative error of Equation (A.13) for different values of d_0 compared to when $d_0 = 60$ nm. The dashed lines lead to the points of maximum error for $d < d_0$. (c) Log_{10} of the normalized ranked contributions C_j/C_1 for the 50000 highest contributors j found in map searches with different depths d_0.

REFERENCES CITED

[1] J. J. Thomson. Cathode Rays. *The London, Edinburgh, and Dublin Philosophical Magazine and Journal of Science*, 44(269):293–316, October 1897.

[2] R. A. Millikan. A new modification of the cloud method of determining the elementary electrical charge and the most probable value of that charge. *The London, Edinburgh, and Dublin Philosophical Magazine and Journal of Science*, 19(110):209–228, February 1910.

[3] N. Bohr. The Quantum Postulate and the Recent Development of Atomic Theory 1. *Nature*, 121(3050):580–590, April 1928.

[4] Louis De Broglie. Waves and Quanta. *Nature*, 112(2815):540, October 1923.

[5] G. P. Thomson and A. Reid. Diffraction of Cathode Rays by a Thin Film. *Nature*, 119(3007):890–890, June 1927.

[6] C. J. Davisson and L. H. Germer. Reflection of Electrons by a Crystal of Nickel. *Proc Natl Acad Sci U S A*, 14(4):317–322, April 1928.

[7] E. Ruska. The early development of electron lenses and electron microscopy. *Microsc Acta Suppl*, (Suppl 5):1–140, 1980.

[8] D. Gabor. A New Microscopic Principle. *Nature*, 161(4098):777–778, May 1948.

[9] M. E. Haine and T. Mulvey. The Formation of the Diffraction Image with Electrons in the Gabor Diffraction Microscope. *J. Opt. Soc. Am., JOSA*, 42(10):763–773, October 1952.

[10] Yi Jiang, Zhen Chen, Yimo Han, Pratiti Deb, Hui Gao, Saien Xie, Prafull Purohit, Mark W. Tate, Jiwoong Park, Sol M. Gruner, Veit Elser, and David A. Muller. Electron ptychography of 2D materials to deep sub-ångström resolution. *Nature*, 559(7714):343–349, July 2018.

[11] Rachel Courtland. The microscope revolution that's sweeping through materials science. *Nature*, 563(7732):462–464, November 2018.

[12] P.W. Hawkes and E. Kasper. *Principles of Electron Optics: Wave Optics*. Principles of electron optics. Elsevier Science, 2012.

[13] Nicholas Rivera and Ido Kaminer. Light–matter interactions with photonic quasiparticles. *Nature Reviews Physics*, 2(10):538–561, October 2020.

[14] Kangpeng Wang, Raphael Dahan, Saar Nehemia, Ori Reinhardt, Shai Tsesses, Ido Kaminer, Ofer Kfir, Hugo Lourenço-Martins, Armin Feist, Claus Ropers, and Tobias J. Kippenberg. Toward Quantum Optics with Free Electrons. *Optics & Photonics News, OPN*, 31(12):35–35, December 2020.

[15] P. Kruit, R.G. Hobbs, C-S. Kim, Y. Yang, V.R. Manfrinato, J. Hammer, S. Thomas, P. Weber, B. Klopfer, C. Kohstall, T. Juffmann, M.A. Kasevich, P. Hommelhoff, and K.K. Berggren. Designs for a quantum electron microscope. *Ultramicroscopy*, 164:31–45, May 2016.

[16] Armin Feist, Sergey V. Yalunin, Sascha Schäfer, and Claus Ropers. High-purity free-electron momentum states prepared by three-dimensional optical phase modulation. *Phys. Rev. Research*, 2(4):043227, November 2020.

[17] Katharina E. Priebe, Christopher Rathje, Sergey V. Yalunin, Thorsten Hohage, Armin Feist, Sascha Schäfer, and Claus Ropers. Attosecond electron pulse trains and quantum state reconstruction in ultrafast transmission electron microscopy. *Nature Photonics*, 11(12):793–797, December 2017.

[18] A. Asenjo-Garcia and F. J. García de Abajo. Dichroism in the Interaction between Vortex Electron Beams, Plasmons, and Molecules. *Phys. Rev. Lett.*, 113(6):066102, August 2014.

[19] Herman Batelaan and Akira Tonomura. The Aharonov–Bohm effects: Variations on a subtle theme. *Physics Today*, 62(9):38–43, September 2009.

[20] N. Kerker, R. Röpke, L. M. Steinert, A. Pooch, and A. Stibor. Quantum decoherence by Coulomb interaction. *New J. Phys.*, 22(6):063039, June 2020.

[21] Shahaf Asban and F. Javier García de Abajo. Generation, characterization, and manipulation of quantum correlations in electron beams. *npj Quantum Information*, 7(1):1–6, February 2021.

[22] Brett Barwick, David J. Flannigan, and Ahmed H. Zewail. Photon-induced near-field electron microscopy. *Nature*, 462(7275):902–906, December 2009.

[23] Giulio Guzzinati, Armand Béché, Hugo Lourenço-Martins, Jérôme Martin, Mathieu Kociak, and Jo Verbeeck. Probing the symmetry of the potential of localized surface plasmon resonances with phase-shaped electron beams. *Nat Commun*, 8(1):1–8, April 2017.

[24] Franz Hasselbach. Interferometry with de Broglie Waves. In Alwyn van der Merwe and Augusto Garuccio, editors, *Waves and Particles in Light and Matter*, pages 49–63. Springer US, Boston, MA, 1994.

[25] Albert Polman, Mathieu Kociak, and F. Javier García de Abajo. Electron-beam spectroscopy for nanophotonics. *Nat. Mater.*, 18(11):1158–1171, November 2019.

[26] Paul Adrien Maurice Dirac and Ralph Howard Fowler. The quantum theory of the electron. *Proceedings of the Royal Society of London. Series A, Containing Papers of a Mathematical and Physical Character*, 117(778):610–624, February 1928.

[27] L. Reimer. *Transmission Electron Microscopy: Physics of Image Formation and Microanalysis*. Springer Series in Optical Sciences. Springer Berlin Heidelberg, 2013.

[28] J.W. Goodman. *Introduction to Fourier Optics*. McGraw-Hill physical and quantum electronics series. W. H. Freeman, 2005.

[29] C. Tai, IEEE Antennas, Propagation Society, IEEE Microwave Theory, and Techniques Society. *Dyadic Green Functions in Electromagnetic Theory*. IEEE Press Publication Series. IEEE Press, 1994.

[30] F. J. García de Abajo. Optical excitations in electron microscopy. *Rev. Mod. Phys.*, 82(1):209–275, February 2010.

[31] Cameron W. Johnson, Dylan H. Bauer, and Benjamin J. McMorran. Improved control of electron computer-generated holographic grating groove profiles using ion beam gas-assisted etching. *Appl. Opt., AO*, 59(6):1594–1601, February 2020.

[32] B. R. Brown and A. W. Lohmann. Complex Spatial Filtering with Binary Masks. *Appl. Opt., AO*, 5(6):967–969, June 1966.

[33] G. Tricoles. Computer generated holograms: an historical review. *Appl. Opt., AO*, 26(20):4351–4360, October 1987.

[34] Roy Shiloh, Peng-Han Lu, Roei Remez, Amir H. Tavabi, Giulio Pozzi, Rafal E. Dunin-Borkowski, and Ady Arie. Nanostructuring of electron beams. *Phys. Scr.*, 94(3):034004, January 2019.

[35] Dusan Sarenac, Michael G. Huber, Benjamin Heacock, Muhammad Arif, Charles W. Clark, David G. Cory, Chandra B. Shahi, and Dmitry A. Pushin. Holography with a neutron interferometer. *Opt. Express, OE*, 24(20):22528–22535, October 2016.

[36] J. Fujita. Atomic beam holography for nanofabrication. *J. Vac. Sci. Technol. B*, 16(6):3855, November 1998.

[37] Markus Arndt, Olaf Nairz, Julian Vos-Andreae, Claudia Keller, Gerbrand van der Zouw, and Anton Zeilinger. Wave-particle duality of c 60 molecules. *Nature*, 401(6754):680, October 1999.

[38] S.M. Lloyd, M. Babiker, G. Thirunavukkarasu, and J. Yuan. Electron vortices: Beams with orbital angular momentum. *Rev. Mod. Phys.*, 89(3):035004, August 2017.

[39] Devendra Singh Negi, Juan Carlos Idrobo, and Ján Rusz. Probing the localization of magnetic dichroism by atomic-size astigmatic and vortex electron beams. *Sci Rep*, 8(1):1–12, March 2018.

[40] Martin Linck, Peter A. Ercius, Jordan S. Pierce, and Benjamin J. McMorran. Aberration corrected STEM by means of diffraction gratings. *Ultramicroscopy*, 182:36–43, November 2017.

[41] Vincenzo Grillo, Amir H. Tavabi, Emrah Yucelen, Peng-Han Lu, Federico Venturi, Hugo Larocque, Lei Jin, Aleksei Savenko, Gian Carlo Gazzadi, Roberto Balboni, Stefano Frabboni, Peter Tiemeijer, Rafal E. Dunin-Borkowski, and Ebrahim Karimi. Towards a holographic approach to spherical aberration correction in scanning transmission electron microscopy. *Opt. Express, OE*, 25(18):21851–21860, September 2017.

[42] Roy Shiloh, Roei Remez, Peng-Han Lu, Lei Jin, Yossi Lereah, Amir H. Tavabi, Rafal E. Dunin-Borkowski, and Ady Arie. Spherical aberration correction in a scanning transmission electron microscope using a sculpted thin film. *Ultramicroscopy*, 189:46–53, June 2018.

[43] Fehmi S. Yasin, Tyler R. Harvey, Jordan J. Chess, Jordan S. Pierce, and Benjamin J. McMorran. Path-separated electron interferometry in a scanning transmission electron microscope. *J. Phys. D: Appl. Phys.*, 51(20):205104, April 2018.

[44] Colin Ophus, Jim Ciston, Jordan Pierce, Tyler R. Harvey, Jordan Chess, Benjamin J. McMorran, Cory Czarnik, Harald H. Rose, and Peter Ercius. Efficient linear phase contrast in scanning transmission electron microscopy with matched illumination and detector interferometry. *Nature Communications*, 7:10719, February 2016.

[45] J. Pierce, J. Webster, H. Larocque, E. Karimi, B. McMorran, and A. Forbes. Coiling free electron matter waves. *New J. Phys.*, 21(4):043018, April 2019.

[46] Ben McMorran, John D. Perreault, T. A. Savas, and Alex Cronin. Diffraction of 0.5kev electrons from free-standing transmission gratings. *Ultramicroscopy*, 106(4):356–364, March 2006.

[47] Brett Barwick, Glen Gronniger, Lu Yuan, Sy-Hwang Liou, and Herman Batelaan. A measurement of electron-wall interactions using transmission diffraction from nanofabricated gratings. *Journal of Applied Physics*, 100(7):074322, October 2006.

[48] J. Verbeeck, H. Tian, and P. Schattschneider. Production and application of electron vortex beams. *Nature*, 467(7313):301–304, September 2010.

[49] Tyler R. Harvey, Jordan S. Pierce, Amit K. Agrawal, Peter Ercius, Martin Linck, and Benjamin J. McMorran. Efficient diffractive phase optics for electrons. *New J. Phys.*, 16(9):093039, September 2014.

[50] Roy Shiloh, Yossi Lereah, Yigal Lilach, and Ady Arie. Sculpturing the electron wave function using nanoscale phase masks. *Ultramicroscopy*, 144:26–31, September 2014.

[51] Vincenzo Grillo, Gian Carlo Gazzadi, Ebrahim Karimi, Erfan Mafakheri, Robert W. Boyd, and Stefano Frabboni. Highly efficient electron vortex beams generated by nanofabricated phase holograms. *Appl. Phys. Lett.*, 104(4):043109, January 2014.

[52] Benjamin J. McMorran, Amit Agrawal, Ian M. Anderson, Andrew A. Herzing, Henri J. Lezec, Jabez J. McClelland, and John Unguris. Electron Vortex Beams with High Quanta of Orbital Angular Momentum. *Science*, 331(6014):192–195, January 2011.

[53] E. Mafakheri, A. H. Tavabi, P.-H. Lu, R. Balboni, F. Venturi, C. Menozzi, G. C. Gazzadi, S. Frabboni, A. Sit, R. E. Dunin-Borkowski, E. Karimi, and V. Grillo. Realization of electron vortices with large orbital angular momentum using miniature holograms fabricated by electron beam lithography. *Appl. Phys. Lett.*, 110(9):093113, February 2017.

[54] A. Béché, R. Winkler, H. Plank, F. Hofer, and J. Verbeeck. Focused electron beam induced deposition as a tool to create electron vortices. *Micron*, 80:34–38, January 2016.

[55] Simon Hettler, Lucas Radtke, Lukas Grünewald, Yuliya Lisunova, Oliver Peric, Juergen Brugger, and Simon Bonanni. Phase masks for electron microscopy fabricated by thermal scanning probe lithography. *Micron*, 127:102753, December 2019.

[56] Lukas Grünewald, Dagmar Gerthsen, and Simon Hettler. Fabrication of phase masks from amorphous carbon thin films for electron-beam shaping. *Beilstein J. Nanotechnol.*, 10(1):1290–1302, June 2019.

[57] Ivo Utke, Patrik Hoffmann, and John Melngailis. Gas-assisted focused electron beam and ion beam processing and fabrication. *Journal of Vacuum Science & Technology B: Microelectronics and Nanometer Structures Processing, Measurement, and Phenomena*, 26(4):1197–1276, July 2008.

[58] Earl J. Kirkland. Calculation of Images of Thin Specimens. In Earl J. Kirkland, editor, *Advanced Computing in Electron Microscopy*, pages 77–113. Springer US, Boston, MA, 2010.

[59] R. J. Young, J. R. A. Cleaver, and H. Ahmed. Characteristics of gas-assisted focused ion beam etching. *Journal of Vacuum Science & Technology B: Microelectronics and Nanometer Structures Processing, Measurement, and Phenomena*, 11(2):234–241, March 1993.

[60] Somnath Bhattacharyya, Christoph T. Koch, and Manfred Rühle. Projected potential profiles across interfaces obtained by reconstructing the exit face wave function from through focal series. *Ultramicroscopy*, 106(6):525–538, April 2006.

[61] Tyler R. Harvey, Fehmi S. Yasin, Jordan J. Chess, Jordan S. Pierce, Roberto M. S. dos Reis, Vasfi Burak Özdöl, Peter Ercius, Jim Ciston, Wenchun Feng, Nicholas A. Kotov, Benjamin J. McMorran, and Colin Ophus. Interpretable and Efficient Interferometric Contrast in Scanning Transmission Electron Microscopy with a Diffraction-Grating Beam Splitter. *Phys. Rev. Applied*, 10(6):061001, December 2018.

[62] McMorran Benjamin J., Agrawal Amit, Ercius Peter A., Grillo Vincenzo, Herzing Andrew A., Harvey Tyler R., Linck Martin, and Pierce Jordan S. Origins and demonstrations of electrons with orbital angular momentum. *Philosophical Transactions of the Royal Society A: Mathematical, Physical and Engineering Sciences*, 375(2087):20150434, February 2017.

[63] Tyler R. Harvey, Jordan S. Pierce, Jordan J. Chess, and Benjamin J. McMorran. Demonstration of electron helical dichroism as a local probe of chirality. *arXiv:1507.01810 [cond-mat, physics:physics]*, July 2015.

[64] Jo Verbeeck, He Tian, and Gustaaf Van Tendeloo. How to Manipulate Nanoparticles with an Electron Beam? *Advanced Materials*, 25(8):1114–1117, 2013.

[65] Vincenzo Grillo, Ebrahim Karimi, Roberto Balboni, Gian Carlo Gazzadi, Stefano Frabboni, Erfan Mafakheri, and Robert W. Boyd. Innovative Phase Plates for Beam Shaping. *Microscopy and Microanalysis*, 20(S3):228–229, August 2014.

[66] Fehmi S. Yasin, Ken Harada, Daisuke Shindo, Hiroyuki Shinada, Benjamin J. McMorran, and Toshiaki Tanigaki. A tunable path-separated electron interferometer with an amplitude-dividing grating beamsplitter. *Appl. Phys. Lett.*, 113(23):233102, December 2018.

[67] M. A. R. Krielaart and P. Kruit. Grating mirror for diffraction of electrons. *Phys. Rev. A*, 98(6):063806, December 2018.

[68] Jo Verbeeck, Armand Béché, Knut Müller-Caspary, Giulio Guzzinati, Minh Anh Luong, and Martien Den Hertog. Demonstration of a 2x2 programmable phase plate for electrons. *Ultramicroscopy*, 190:58–65, July 2018.

[69] Zhong-lin Wang. *Elastic and Inelastic Scattering in Electron Diffraction and Imaging*. Springer US, 1995.

[70] J. C. T. Lee, S. J. Alexander, S. D. Kevan, S. Roy, and B. J. McMorran. Laguerre-Gauss and Hermite-Gauss soft X-ray states generated using diffractive optics. *Nature Photonics*, 13(3):205, March 2019.

[71] Cameron W. Johnson, Jordan S. Pierce, Rich C. Moraski, Amy E. Turner, Alice T. Greenberg, Will S. Parker, and Benjamin J. McMorran. Exact design of complex amplitude holograms for producing arbitrary scalar fields. *Opt. Express, OE*, 28(12):17334–17346, June 2020.

[72] Halina Rubinsztein-Dunlop, Andrew Forbes, M V Berry, M R Dennis, David L Andrews, Masud Mansuripur, Cornelia Denz, Christina Alpmann, Peter Banzer, Thomas Bauer, Ebrahim Karimi, Lorenzo Marrucci, Miles Padgett, Monika Ritsch-Marte, Natalia M Litchinitser, Nicholas P Bigelow, C Rosales-Guzmán, A Belmonte, J P Torres, Tyler W Neely, Mark Baker, Reuven Gordon, Alexander B Stilgoe, Jacquiline Romero, Andrew G White, Robert Fickler, Alan E Willner, Guodong Xie, Benjamin McMorran, and Andrew M Weiner. Roadmap on structured light. *J. Opt.*, 19(1):013001, January 2017.

[73] Jérémie Harris, Vincenzo Grillo, Erfan Mafakheri, Gian Carlo Gazzadi, Stefano Frabboni, Robert W. Boyd, and Ebrahim Karimi. Structured quantum waves. *Nature Phys*, 11(8):629–634, August 2015.

[74] Charles W. Clark, Roman Barankov, Michael G. Huber, Muhammad Arif, David G. Cory, and Dmitry A. Pushin. Controlling neutron orbital angular momentum. *Nature*, 525(7570):504–506, September 2015.

[75] V. E. Lembessis, D. Ellinas, M. Babiker, and O. Al-Dossary. Atom vortex beams. *Phys. Rev. A*, 89(5):053616, May 2014.

[76] S. Sala, A. Ariga, A. Ereditato, R. Ferragut, M. Giammarchi, M. Leone, C. Pistillo, and P. Scampoli. First demonstration of antimatter wave interferometry. *Science Advances*, 5(5):eaav7610, May 2019.

[77] Victor Arrizón, Guadalupe Méndez, and David Sánchez-de La-Llave. Accurate encoding of arbitrary complex fields with amplitude-only liquid crystal spatial light modulators. *Opt. Express, OE*, 13(20):7913–7927, October 2005.

[78] Victor Arrizón, Ulises Ruiz, Rosibel Carrada, and Luis A. González. Pixelated phase computer holograms for the accurate encoding of scalar complex fields. *J. Opt. Soc. Am. A, JOSAA*, 24(11):3500–3507, November 2007.

[79] Eliot Bolduc, Nicolas Bent, Enrico Santamato, Ebrahim Karimi, and Robert W. Boyd. Exact solution to simultaneous intensity and phase encryption with a single phase-only hologram. *Opt. Lett., OL*, 38(18):3546–3549, September 2013.

[80] Mohammad Mirhosseini, Omar S. Magaña-Loaiza, Changchen Chen, Brandon Rodenburg, Mehul Malik, and Robert W. Boyd. Rapid generation of light beams carrying orbital angular momentum. *Opt. Express, OE*, 21(25):30196–30203, December 2013.

[81] S. M. Lloyd, M. Babiker, and J. Yuan. Interaction of electron vortices and optical vortices with matter and processes of orbital angular momentum exchange. *Phys. Rev. A*, 86(2):023816, August 2012.

[82] Mario Krenn and Anton Zeilinger. On small beams with large topological charge: II. Photons, electrons and gravitational waves. *New J. Phys.*, 20(6):063006, June 2018.

[83] M. Babiker, J. Yuan, and V. E. Lembessis. Electron vortex beams subject to static magnetic fields. *Phys. Rev. A*, 91(1):013806, January 2015.

[84] Dmitry Karlovets. Relativistic vortex electrons: Paraxial versus nonparaxial regimes. *Phys. Rev. A*, 98(1):012137, July 2018.

[85] Stefano Marchesini and Anne Sakdinawat. Shaping coherent x-rays with binary optics. *Opt. Express, OE*, 27(2):907–917, January 2019.

[86] Vincenzo Grillo, Ebrahim Karimi, Roberto Balboni, Gian Carlo Gazzadi, Federico Venturi, Stefano Frabboni, Jordan S. Pierce, Benjamin J. McMorran, and Robert W. Boyd. Electron holograms encoding amplitude and phase for the generation of arbitrary wavefunctions. *Microscopy and Microanalysis*, 21(S3):503–504, August 2015.

[87] Jordan Pierce. *Holographic Sculpting of Electron Beams with Diffraction Gratings*. PhD thesis, January 2019. Accepted: 2019-01-11T22:26:56Z Publisher: University of Oregon.

[88] L. J. Allen and M. P. Oxley. Phase retrieval from series of images obtained by defocus variation. *Optics Communications*, 199(1):65–75, November 2001.

[89] Cameron W. Johnson, Amy E. Turner, and Benjamin J. McMorran. A Scanning 2-Grating Free Electron Mach-Zehnder Interferometer. *arXiv:2104.09992 [physics.ins-det]*, April 2021.

[90] Akira Tonomura. *Electron Holography*. Springer Series in Optical Sciences. Springer-Verlag, Berlin Heidelberg, 2 edition, 1999.

[91] Rafal E. Dunin-Borkowski, András Kovács, Takeshi Kasama, Martha R. McCartney, and David J. Smith. Electron Holography. In Peter W. Hawkes and John C. H. Spence, editors, *Springer Handbook of Microscopy*, Springer Handbooks, pages 767–818. Springer International Publishing, Cham, 2019.

[92] Akira Tonomura, Nobuyuki Osakabe, Tsuyoshi Matsuda, Takeshi Kawasaki, Junji Endo, Shinichiro Yano, and Hiroji Yamada. Evidence for Aharonov-Bohm effect with magnetic field completely shielded from electron wave. *Physical Review Letters*, 56(8):792–795, February 1986.

[93] Amy E. Turner, Cameron W. Johnson, Pieter Kruit, and Benjamin J. McMorran. Interaction-free measurement with electrons. *Submitted Manuscript*, 2021.

[94] William P. Putnam and Mehmet Fatih Yanik. Noninvasive electron microscopy with interaction-free quantum measurements. *Physical Review A*, 80(4):040902, October 2009.

[95] A. Pooch, M. Seidling, N. Kerker, R. Röpke, A. Rembold, W. T. Chang, I. S. Hwang, and A. Stibor. Coherent properties of a tunable low-energy electron-matter-wave source. *Phys. Rev. A*, 97(1):013611, January 2018.

[96] I. Madan, G. M. Vanacore, E. Pomarico, G. Berruto, R. J. Lamb, D. McGrouther, T. T. A. Lummen, T. Latychevskaia, F. J. García de Abajo, and F. Carbone. Holographic imaging of electromagnetic fields via electron-light quantum interference. *Science Advances*, 5(5):eaav8358, May 2019.

[97] Katharina E. Echternkamp, Armin Feist, Sascha Schäfer, and Claus Ropers. Ramsey-type phase control of free-electron beams. *Nature Phys*, 12(11):1000–1004, November 2016.

[98] John D. Monnier. Optical interferometry in astronomy. *Rep. Prog. Phys.*, 66(5):789–857, April 2003.

[99] Peter J. de Groot. A review of selected topics in interferometric optical metrology. *Rep. Prog. Phys.*, 82(5):056101, April 2019.

[100] Alexander D. Cronin, Jörg Schmiedmayer, and David E. Pritchard. Optics and interferometry with atoms and molecules. *Rev. Mod. Phys.*, 81(3):1051–1129, July 2009.

[101] Jian-Wei Pan, Zeng-Bing Chen, Chao-Yang Lu, Harald Weinfurter, Anton Zeilinger, and Marek Żukowski. Multiphoton entanglement and interferometry. *Rev. Mod. Phys.*, 84(2):777–838, May 2012.

[102] Navid Abedzadeh, M. A. R. Krielaart, Chung-Soo Kim, John Simonaitis, Richard Hobbs, Pieter Kruit, and Karl K. Berggren. Electrostatic electron mirror in SEM for simultaneous imaging of top and bottom surfaces of a sample. *arXiv:2012.09902 [physics]*, December 2020.

[103] M. A. R. Krielaart and P. Kruit. Flat electron mirror. *Ultramicroscopy*, 220:113157, January 2021.

[104] Hannes Lichte, Petr Formanek, Andreas Lenk, Martin Linck, Christopher Matzeck, Michael Lehmann, and Paul Simon. Electron Holography: Applications to Materials Questions. *Annual Review of Materials Research*, 37(1):539–588, 2007.

[105] Shery L. Y. Chang, Christian Dwyer, Chris B. Boothroyd, and Rafal E. Dunin-Borkowski. Optimising electron holography in the presence of partial coherence and instrument instabilities. *Ultramicroscopy*, 151:37–45, April 2015.

[106] Daniel L. Freimund, Kayvan Aflatooni, and Herman Batelaan. Observation of the Kapitza–Dirac effect. *Nature*, 413(6852):142–143, September 2001.

[107] R. Zimmermann, P. Weber, M. Seidling, and P. Hommelhoff. Beam splitting of low-energy guided electrons with a two-sided microwave chip. *Appl. Phys. Lett.*, 115(10):104103, September 2019.

[108] L. Marton. Electron Interferometer. *Phys. Rev.*, 85(6):1057–1058, March 1952.

[109] Helmut Rauch and Samuel A. Werner. *Neutron Interferometry: Lessons in Experimental Quantum Mechanics, Wave-particle Duality, and Entanglement*. Oxford University Press, 2015.

[110] T. Berrada, S. van Frank, R. Bücker, T. Schumm, J.-F. Schaff, and J. Schmiedmayer. Integrated Mach–Zehnder interferometer for Bose–Einstein condensates. *Nature Communications*, 4(1):2077, June 2013.

[111] Yang Ji, Yunchul Chung, D. Sprinzak, M. Heiblum, D. Mahalu, and Hadas Shtrikman. An electronic Mach–Zehnder interferometer. *Nature*, 422(6930):415–418, March 2003.

[112] M. Jo, P. Brasseur, A. Assouline, G. Fleury, H.-S. Sim, K. Watanabe, T. Taniguchi, W. Dumnernpanich, P. Roche, D.C. Glattli, N. Kumada, F.D. Parmentier, and P. Roulleau. Quantum Hall Valley Splitters and a Tunable Mach-Zehnder Interferometer in Graphene. *Phys. Rev. Lett.*, 126(14):146803, April 2021.

[113] William D. Oliver, Yang Yu, Janice C. Lee, Karl K. Berggren, Leonid S. Levitov, and Terry P. Orlando. Mach-Zehnder Interferometry in a Strongly Driven Superconducting Qubit. *Science*, 310(5754):1653–1657, December 2005.

[114] Amir H. Tavabi, Martial Duchamp, Vincenzo Grillo, Rafal E. Dunin-Borkowski, and Giulio Pozzi. New experiments with a double crystal electron interferometer. *Eur. Phys. J. Appl. Phys.*, 78(1):10701, April 2017.

[115] Akshay Agarwal, Chung-Soo Kim, Richard Hobbs, Dirk van Dyck, and Karl K. Berggren. A nanofabricated, monolithic, path-separated electron interferometer. *Scientific Reports*, 7(1):1677, May 2017.

[116] L. Marton, J. Arol Simpson, and J. A. Suddeth. An Electron Interferometer. *Review of Scientific Instruments*, 25(11):1099–1104, November 1954.

[117] G. Gronniger, B. Barwick, and H. Batelaan. A three-grating electron interferometer. *New J. Phys.*, 8(10):224–224, October 2006.

[118] J. M. Cowley and Sumio Iijima. Electron Microscope Image Contrast for Thin Crystal. *Zeitschrift für Naturforschung A*, 27(3):445–451, March 1972.

[119] G. Matteucci, G. F. Missiroli, M. Muccini, and G. Pozzi. Electron holography in the study of the electrostatic fields: the case of charged microtips. *Ultramicroscopy*, 45(1):77–83, August 1992.

[120] V. Migunov, A. London, M. Farle, and R. E. Dunin-Borkowski. Model-independent measurement of the charge density distribution along an Fe atom probe needle using off-axis electron holography without mean inner potential effects. *Journal of Applied Physics*, 117(13):134301, April 2015.

[121] Martha R. McCartney and David J. Smith. Electron Holography: Phase Imaging with Nanometer Resolution. *Annu. Rev. Mater. Res.*, 37(1):729–767, August 2007.

[122] E. Voelkl, F. Zheng, V. Migunov, M. Beleggia, and R. E. Dunin-Borkowski. Live Measurement of Electrical Charge Density in Materials using Off-Axis Electron Holography. *Microscopy and Microanalysis*, 25(S2):44–45, August 2019.

[123] Ajuan Cui, J. C. Fenton, Wuxia Li, Tiehan H. Shen, Zhe Liu, Qiang Luo, and Changzhi Gu. Ion-beam-induced bending of freestanding amorphous nanowires: The importance of the substrate material and charging. *Appl. Phys. Lett.*, 102(21):213112, May 2013.

[124] Y.C. Wang, T.M. Chou, M. Libera, E. Voelkl, and B.G. Frost. Measurement of Polystyrene Mean Inner Potential by Transmission Electron Holography of Latex Spheres. *Microscopy and Microanalysis*, 4(2):146–157, April 1998.

[125] David Cooper, Cheng-Ta Pan, and Sarah Haigh. Atomic resolution electrostatic potential mapping of graphene sheets by off-axis electron holography. *Journal of Applied Physics*, 115(23):233709, June 2014.

[126] Fehmi S. Yasin, Tyler R. Harvey, Jordan J. Chess, Jordan S. Pierce, Colin Ophus, Peter Ercius, and Benjamin J. McMorran. Probing Light Atoms at Subnanometer Resolution: Realization of Scanning Transmission Electron Microscope Holography. *Nano Lett.*, 18(11):7118–7123, November 2018.

[127] Akshay Agarwal, Karl K. Berggren, Yuri J. van Staaden, and Vivek K. Goyal. Reduced damage in electron microscopy by using interaction-free measurement and conditional reillumination. *Physical Review A*, 99(6):063809, June 2019.

[128] Alice Greenberg, Benjamin McMorran, Cameron Johnson, and Fehmi Yasin. Magnetic Phase Imaging Using Interferometric STEM. *Microscopy and Microanalysis*, pages 1–3, July 2020.

[129] Adam Caprez, Brett Barwick, and Herman Batelaan. Macroscopic Test of the Aharonov-Bohm Effect. *Physical Review Letters*, 99(21):210401, November 2007.

[130] P. Schattschneider and S. Löffler. Entanglement and decoherence in electron microscopy. *Ultramicroscopy*, 190:39–44, July 2018.

[131] Peter J. Beierle, Liyun Zhang, and Herman Batelaan. Experimental test of decoherence theory using electron matter waves. *New J. Phys.*, 20(11):113030, November 2018.

[132] R. H. Ritchie. Plasma Losses by Fast Electrons in Thin Films. *Phys. Rev.*, 106(5):874–881, June 1957.

[133] Guillaume Boudarham and Mathieu Kociak. Modal decompositions of the local electromagnetic density of states and spatially resolved electron energy loss probability in terms of geometric modes. *Phys. Rev. B*, 85(24):245447, June 2012.

[134] F. J. García de Abajo. Relativistic energy loss and induced photon emission in the interaction of a dielectric sphere with an external electron beam. *Phys. Rev. B*, 59(4):3095–3107, January 1999.

[135] P. B. Johnson and R. W. Christy. Optical Constants of the Noble Metals. *Phys. Rev. B*, 6(12):4370–4379, December 1972.

[136] F. J. García de Abajo and M. Kociak. Probing the Photonic Local Density of States with Electron Energy Loss Spectroscopy. *Phys. Rev. Lett.*, 100(10):106804, March 2008.

[137] Hannes Lichte and Bert Freitag. Inelastic electron holography. *Ultramicroscopy*, 81(3):177–186, April 2000.

[138] F. Röder and H. Lichte. Inelastic electron holography – first results with surface plasmons. *Eur. Phys. J. Appl. Phys.*, 54(3):33504, June 2011.

[139] J. Verbeeck, D. van Dyck, H. Lichte, P. Potapov, and P. Schattschneider. Plasmon holographic experiments: theoretical framework. *Ultramicroscopy*, 102(3):239–255, February 2005.

[140] J. Verbeeck. Interpretation of 'Energy-filtered electron-diffracted beam holography' by R.A. Herring. *Ultramicroscopy*, 106(6):461–465, April 2006.

[141] Daniel Ugarte and Caterina Ducati. Controlling multipolar surface plasmon excitation through the azimuthal phase structure of electron vortex beams. *Phys. Rev. B*, 93(20):205418, May 2016.

[142] J. Krehl, G. Guzzinati, J. Schultz, P. Potapov, D. Pohl, Jérôme Martin, J. Verbeeck, A. Fery, B. Büchner, and A. Lubk. Spectral field mapping in plasmonic nanostructures with nanometer resolution. *Nature Communications*, 9(1):4207, October 2018.

[143] Vincenzo Amendola, Roberto Pilot, Marco Frasconi, Onofrio M. Maragò, and Maria Antonia Iatì. Surface plasmon resonance in gold nanoparticles: a review. *J. Phys.: Condens. Matter*, 29(20):203002, April 2017.

[144] Jaysen Nelayah, Mathieu Kociak, Odile Stéphan, F. Javier García de Abajo, Marcel Tencé, Luc Henrard, Dario Taverna, Isabel Pastoriza-Santos, Luis M. Liz-Marzán, and Christian Colliex. Mapping surface plasmons on a single metallic nanoparticle. *Nature Phys*, 3(5):348–353, May 2007.

[145] Michel Bosman, Vicki J. Keast, Masashi Watanabe, Abbas I. Maaroof, and Michael B. Cortie. Mapping surface plasmons at the nanometre scale with an electron beam. *Nanotechnology*, 18(16):165505, March 2007.

[146] Steven J. Barrow, David Rossouw, Alison M. Funston, Gianluigi A. Botton, and Paul Mulvaney. Mapping Bright and Dark Modes in Gold Nanoparticle Chains using Electron Energy Loss Spectroscopy. *Nano Lett.*, 14(7):3799–3808, July 2014.

[147] Lars Kiewidt, Mirza Karamehmedović, Christian Matyssek, Wolfram Hergert, Lutz Mädler, and Thomas Wriedt. Numerical simulation of Electron Energy Loss Spectroscopy using a Generalized Multipole Technique. *Ultramicroscopy*, 133:101–108, October 2013.

[148] Chen Mechel, Yaniv Kurman, Aviv Karnieli, Nicholas Rivera, Ady Arie, and Ido Kaminer. Quantum correlations in electron microscopy. *Optica, OPTICA*, 8(1):70–78, January 2021.

[149] N. Yamamoto, K. Araya, and F. J. García de Abajo. Photon emission from silver particles induced by a high-energy electron beam. *Phys. Rev. B*, 64(20):205419, November 2001.

[150] M. Kociak and L. F. Zagonel. Cathodoluminescence in the scanning transmission electron microscope. *Ultramicroscopy*, 176:112–131, May 2017.

[151] Matteo Zanfrognini, Enzo Rotunno, Stefano Frabboni, Alicia Sit, Ebrahim Karimi, Ulrich Hohenester, and Vincenzo Grillo. Orbital Angular Momentum and Energy Loss Characterization of Plasmonic Excitations in Metallic Nanostructures in TEM. *ACS Photonics*, 6(3):620–627, March 2019.

[152] Amir H. Tavabi, Paolo Rosi, Enzo Rotunno, Alberto Roncaglia, Luca Belsito, Stefano Frabboni, Giulio Pozzi, Gian Carlo Gazzadi, Peng-Han Lu, Robert Nijland, Moumita Ghosh, Peter Tiemeijer, Ebrahim Karimi, Rafal E. Dunin-Borkowski, and Vincenzo Grillo. Experimental Demonstration of an Electrostatic Orbital Angular Momentum Sorter for Electron Beams. *Phys. Rev. Lett.*, 126(9):094802, March 2021.

[153] Marian O. Scully, Berthold-Georg Englert, and Herbert Walther. Quantum optical tests of complementarity. *Nature*, 351(6322):111–116, May 1991.

[154] Michael S. Chapman, Troy D. Hammond, Alan Lenef, Jörg Schmiedmayer, Richard A. Rubenstein, Edward Smith, and David E. Pritchard. Photon Scattering from Atoms in an Atom Interferometer: Coherence Lost and Regained. *Phys. Rev. Lett.*, 75(21):3783–3787, November 1995.

[155] Yoon-Ho Kim, Rong Yu, Sergei P. Kulik, Yanhua Shih, and Marlan O. Scully. Delayed "Choice" Quantum Eraser. *Phys. Rev. Lett.*, 84(1):1–5, January 2000.

[156] A. Bienfait, Y.P. Zhong, H.-S. Chang, M.-H. Chou, C.R. Conner, É. Dumur, J. Grebel, G.A. Peairs, R.G. Povey, K.J. Satzinger, and A.N. Cleland. Quantum Erasure Using Entangled Surface Acoustic Phonons. *Phys. Rev. X*, 10(2):021055, June 2020.

[157] Milton Abramowitz and Irene A. Stegun. *Handbook of Mathematical Functions with Formulas, Graphs, and Mathematical Tables*. Dover, 1964.

[158] Jordan S. Pierce and Cameron W. Johnson. Corrected holography. https://github.com/McMorranLab/correcte_holography, 2020.